The Structure and Substructure of Cold Dark Matter Halos

by

Aaron D. Ludlow
B.Sc., Memorial University of Newfoundland, 2002

Karun A Thesis submitted in Partial Fulfillment of the
Requirements for the Degree of

Doctor of Philosophy

in the

Department of Physics and Astronomy

Supervisory Committee

The Structure and Substructure of Cold Dark Matter Halos

by

Aaron D. Ludlow

Supervisory Committee

Dr. J. F. Navarro, (Department of Physics and Astronomy)

Supervisor

Dr. A. Babul, (Department of Physics and Astronomy)

Departmental Member

Dr. C. Pritchet, (Department of Physics and Astronomy)

Departmental Member

Dr. R. Illner, (Department Mathematics and Statistics)

Outside Member

Supervisory Committee:

Dr. J. F. Navarro, Supervisor (Department of Physics and Astronomy)

Dr. A. Babul, Departmental Member (Department of Physics and Astronomy)

Dr. C. Pritchet, Departmental Member (Department of Physics and Astronomy)

Dr. R. Illner, Outside Member (Department Mathematics and Statistics)

Abstract

We study the structure and substructure of ΛCDM halos using a suite of high-resolution cosmological N-body simulations. Our analysis of the substructure population of dark matter halos focuses on their mass and peak circular velocity functions, as well as their spatial distribution and dynamics. In our analysis, we consider the whole population of subhalos *physically associated* with the main halo, defined as those that have, at some time, crossed within the virial radius of the main progenitor. We find that this population extends beyond 3 *times the virial radius* and includes objects on unorthodox orbits, several of which travel at velocities approaching the nominal escape speed from the system. We trace the origin of these unorthodox orbits to the tidal dissociation of bound groups, which results in the ejection of some systems along tidal streams. This process primarily influences low-mass systems leading to clear mass-dependent biases in their spatial distribution and kinematics: the lower the subhalo mass at accretion time the more concentrated and kinematically hotter their descendant population. When quantified in terms of *present day* subhalo mass these trends disappear, presumably due to the increased effect of dynamical friction and tidal stripping on massive systems. We confirm several of these results using the ultra-high resolution *Aquarius* simulations,

which extend the dynamic range of the subhalo mass function by nearly 3 orders of magnitude. Using these simulations we confirm that the substructure mass function follows a power-law, $dN/dM \propto M^{-1.9}$, and exhibits very little halo-to-halo scatter. This implies that the total mass in substructure within a given halo is bounded to a small fraction of the total halo mass, with the smooth component dominating the halo inner regions. Using the Aquarius simulations we study the structure of galaxy-sized ΛCDM halos. We find that the spherically averaged density profiles become increasingly shallow toward the halo center, with no sign of converging to an asymptotic power-law; a radial dependence accurately described by the Einasto profile. In our highest resolution run we resolve scales approaching 100 pc, at which point the *maximum* asymptotic slope is ≈ -0.89, confidently ruling out recent claims for cusps as steep as $r^{-1.2}$. We find that the spherically averaged density and velocity dispersion profiles are *not* universal, but rather show subtle but significant deviations from self-similarity. Intriguingly, departures from self-similarity are minimized when cast in terms of the phase-space density profile, ρ/σ^3, suggesting an intimate scaling between densities and velocity dispersions across the system. The phase-space density profiles follow a power-law with radius, $r^{-1.875}$, identical to that of Bertschinger's similarity solution for self-similar infall onto a point mass in an otherwise unperturbed Einstein-de Sitter universe.

Table of Contents

List of Tables

List of Figures

Acknowledgments

There are many people who deserve my thanks. People who have nurtured my body, soul, and mind in both good times and bad. People who taught me to notice and appreciate the subtle in the obvious, and the obvious in the subtle.

To my Friends: Keats, Kelly, Greg, Nath, and your company...

Thank you for sharing your time, for fire and smoke, for relentless positivity, for conversation, for laughter, for fun, and for communication. Keep those eyes wide. Thank you!

To my Family: Dave, Cynthia, Amy, Anna...

You made me the person I am, and respect the person I have become. Praise. Thank you!

To my Support: Volker, Adrian, Chris, Hugh, and the CITA technical staff...

Without your thoughtful guidance this would be the first and last page. Thank you!

To my Advisor: Julio...

For providing me with interesting projects at a time when I did not know them, for insightful conversation, for introductions, and for support. Thanks you!

These words are dedicated to you

Chapter 1 | *Introduction*

1.1 A Brief Preamble

Cosmological thought is a matured form of ideas and impressions that have existed well before recorded history. Primitive people had the capacity to wonder about their surroundings long before developing the ability to articulate and communicate this awareness. Their curiosity inspired simple questions, such as "What is going on around me?", that have since evolved into the quintessential mission statement of cosmologists: How does the Universe work? To the literalists and fundamentalists within the theistic tradition, cosmology tells a story of a world created and guided by supernatural forces. To scientists, it represents the elucidation of natural forces and universal laws by means of direct observation and rationalization. Due to mankind's intrinsic craving to understand the universe, cosmology historically lays somewhere between philosophy and science; near philosophy as it addresses fundamental questions regarding the origin and fate of the universe; near science as it seeks to answer such questions empirically and objectively.

A cursory look at the history of cosmological studies shows man's fervent desire to place the Earth (or maybe himself) at the center of the universe. This geocentric cosmogony, propounded by the great Greek astronomer Ptolemy (83CE−163CE), was favored by scientists, philosophers, and theologians alike for nearly 1400 years. During this time, however, new means of gathering and processing information from the environment emerged. With the gradual increase in astronomical data these anthropocentric views were discarded for a new, more humbling description of the universe; one in which the Earth and its inhabitants follow a slightly elliptical orbit

around an *average* star, in the periphery of an *average* spiral galaxy, at a couple of hundred kilometers per second in a direction which is almost all together arbitrary.

Developments in particle physics in the mid 20^{th} century indicated that the fundamental constituents of all terrestrial materials comprise just a small fraction of all elementary particles, leaving plenty of room for a world beyond our senses. Until the early 1930's, however, physicists could take some comfort in Astronomy. Observations of distant stars, galaxies, and nebulae showed the spectral signatures of the (mainly) known terrestrial elements. By and large, it seemed that the conspicuous objects in the night sky were made of the same stuff as was known to be abundant on Earth already. The nucleosynthesis fueling stars seemed to produce on a universal scale the same elements already familiar to physicists on earth.

This situation changed gradually after Fritz Zwicky pointed out the odd dynamics of the members of the Coma cluster of galaxies (Zwicky 1933). Assuming virial equilibrium, Zwicky estimated that the average gravitating mass per galaxy required to stabilize the system was about 160 times larger than what one would infer based on the stellar light alone. He suggested that the majority of matter binding the Coma cluster somehow remained dark, and coined the term *dark matter* to describe the missing component. This was the first tangible evidence that there is more out there than "meets the eye", though the significance of Zwicky's findings was not immediately realized. It is interesting to note that only three years after Zwicky's original paper Smith (1936) pointed out that the Virgo cluster also exhibited an unexpectedly high mass, but attributed this effect to "inter-nebular material within the cluster" which was too faint to be observed directly.

The astronomical literature over the next 4 decades is peppered with observations of galaxy rotation curves suggesting that individual galaxies are themselves embedded in massive halos of dark matter, though the connection with the anomalous cluster masses was, for a time, unnoted. In 1939, Horace Babcock obtained long-slit spectral observations of the Andromeda galaxy and showed that the ro-

tational speed of stars (and hence the total galaxy mass) increased with distance from the center in a way that was inconsistent with the observed distribution of light. He concluded that either the importance of dust absorption increased with radius, or that this galaxy had an unusual outer mass-to-light ratio. Subsequent observations of Andromeda, by Rubin & Ford (1970) and Roberts & Whitehurst (1975), using the hydrogen 21 cm emission line clearly showed that the rotation speed did not exhibit the expected Keplerian fall-off, but rather remained constant between $\sim 15 - 30$ kpc, well outside the optical edge of the disk. Together with the theoretical work of Ostriker & Peebles (1973) on disk stability, and of Ostriker, Peebles & Yahil (1974) on radially increasing mass-to-light ratios, this result first convinced the majority of the astronomical community of the reality of the missing mass problem (van den Bergh, 1999): there is missing mass*, and lots of it.

As a result of this work, dark matter assumed a critical role in theories of structure formation despite its evasive identity. It was in this context that a new paradigm for galaxy formation emerged: core condensation in heavy halos (White & Rees, 1978). In this picture, luminous galaxies form as a result of the dissipational collapse of gas onto potential wells provided by dark matter halos. Luminous galaxies form as the cooling gas fragments and forms stars in the dense halo centers.

Apart from galactic studies, results from big bang nucleosynthesis (BBN) (Wagoner, 1967) and cosmic microwave background experiments indicated that the cosmic density of baryons was low, only about $\Omega_b = \rho_b/\rho_{\rm crit} \approx 0.04^\dagger$, necessitating a large non-baryonic constituent to the dark matter. The obvious candidate was the neutrino, which was known at time to be an electrically neutral particle with a possible non-zero rest mass. Neutrinos fall under the general class of hot dark matter (HDM) models since at the time of decoupling they are highly relativistic.

*Strictly speaking, it is not the mass that is missing at all, but rather the light that would be naively assumed to be associated with matter.

†The critical density, $\rho_{\rm crit}$, is the total matter energy density required for a flat universe. Density parameters, such as $\Omega_{\rm bar}$, are used to describe the fraction of the critical density found in a given constituent.

The diametrically different cold dark matter (CDM) model, in which the particles have negligible thermal velocity at decoupling, was later laid out by Peebles (1982) and Blumenthal et al (1984) and has since become the standard paradigm for understanding structure growth in the universe. The preference for CDM over HDM models followed from a seminal series of papers by White et al (1983, 1984, 1987) and Davis et al (1985). These authors used N-body simulations to demonstrate that structure formation, when driven by neutrino clustering, is significantly delayed and suppressed on small scales relative to the CDM models. Observations of galaxy clustering ruled out the "top-down" formation process expected for HDM in favor of the "bottom-up" picture of CDM.

In more recent years, strong and persuasive theoretical arguments, as well as convincing observational results, began pointing towards an even more exotic component of the Universe (e.g. Riess et al 1998; Perlmutter et al 1999). Observations that the geometry of the universe is flat requires a total energy density far greater than that which can be accounted for by the matter (both luminous *and* dark) alone. The additional component, known as dark energy, drives an accelerated expansion and CDM models which include its dynamical effects are referred to as "Λ"CDM models. Neither dark matter nor dark energy have been observed in a laboratory setting, yet the anticipation of their discovery is a primary driver of much of modern cosmology and particle physics.

The work presented in this thesis deals with the formation and structure of dark matter aggregates forming within the currently favored cosmological framework, ΛCDM. An understanding of the formation and evolution of these structures is important for developing insights into the processes responsible for the wealth of luminous objects in the universe today, from superclusters of galaxies ($\gtrsim 10^{16} M_{\odot}$) down to dwarf galaxies ($\lesssim 10^{9} M_{\odot}$). In the following sections of this Chapter I will give a simple account of the main physical principles and background knowledge required to understand the concepts discussed in Chapters 2 through 4.

1.2 The Need for Cold Dark Matter

Much of the observational evidence in favor of dark matter comes from studies of the bulk and internal motions of luminous objects in the universe. The flat outer rotation curves of late-type galaxies indicate a gradual increase in mass at distances well beyond their optical edge, implying that the ratio of total mass to total light is unusually large. This suggests that the total mass profile of spiral galaxies increases roughly linearly with distance over the observed radial range, in stark contrast with the surface brightness profile, which typically shows an exponential fall-off (Rubin & Ford 1970; Roberts & Whitehurst 1975; Rubin et al 1985).

In early-type galaxies, where there is little evidence of rotation, stellar dynamics can still be used as a mass estimator. Here one measures the random motions of a statistical sample of stars to obtain an average kinetic energy for the system. An application of the virial theorem can then be used to estimate the system's total mass assuming equilibrium. This analysis consistently shows that elliptical galaxies, like spirals, are embedded in large halos of dark matter (Binney, Davies & Illingworth 1990; van der Marel, Binney & Davies 1990).

A similar method was followed by Zwicky and Smith in their original analysis of the Coma and Virgo clusters. Here the dynamics of the individual galaxies within galaxy clusters show that these systems are much more massive than the sum of their luminous components. Given that a large fraction of early-type galaxies are currently in clusters, van den Bergh (1962) argued that these systems must be stable on timescales comparable to their ages, disfavoring the hypothesis that massive clusters are actually unbound and hence out of equilibrium.

Adding to the evidence for dark matter on cluster scales is the existence of hot intra-cluster gas (ICM) (e.g. Byram et al 1966; Fritz et al 1971; and Meekins et al 1971). This is the same "inter-nebular material" supposed to be the dark matter by Smith years earlier. The internal energy of the gas is sufficient to induce emission of X-ray photons. Using X-ray observations one can estimate the cluster potential (or

mass) required to match a given set of observations. This analysis again supports the idea that clusters of galaxies are dominated by large halos of dark matter.

Strong dynamical evidence in favor of the CDM paradigm is provided by the Bullet cluster (1E 0657-56), consisting of two colliding clusters of galaxies (Markevitch et al 2002; Clowe et al 2004). The various matter components of galaxy clusters behave quite differently in response to a merger, allowing them to be studied separately. Individual galaxies, which comprise only a small fraction of the total baryonic mass ($\sim$10%), behave much like test particles within the potential generated by the hypothetical dark matter halos. The hot intra-cluster gas, however, is affected by hydrodynamical shocks and pressure forces. Chandra observation of the Bullet cluster show that the spatial distribution of the hot, X-ray gas lags behind that of the cluster galaxies. A mass map constructed from the gravitational distortion of the shape of background galaxies shows unambiguously that most of the gravitating mass is offset from the dominant baryonic component (i.e. the gas), and follows the distribution of individual galaxies. Alternative theories that attempt to negate the dark matter paradigm by modifying gravity (e.g. Milgrom 1983a,b,c; Bekenstein 2004) thus have the challenge of explaining why most of the gravitating mass follows a only small fraction of the baryons.

1.3 Rudiments of Structure Formation

1.3.1 Inflation

The homogeneous and isotropic CDM model provides a very successful framework for interpreting many cosmological observations. It gives an account of the evolutionary history of the universe from times as early as the onset of primordial nucleosynthesis ($t \approx 10^{-2}$) to the present day (13.7 Gyr later). Despite its remarkable success, the standard hot big bang cosmology fails to account for its own initial conditions and thereby leaves a number of fundamental questions unanswered. Why

should the universe be homogeneous and isotropic on scales larger than the horizon? Why does the universe appear spatially flat? What is the origin of the small scale structure in the universe?

A possible solution to these problems was proposed by Alan Guth in 1981 in a new cosmological model known as *inflation*. His original proposal was an extension of the standard big bang model in which the universe experienced an early ($t < 10^{-33}$s) phase of aggressive expansion driven by the repulsive force of some exotic particle or field (known as the inflaton). The origin of the expansion remains unclear yet its effects provide a natural device for solving several long-standing problems facing the standard cosmogony and it is widely considered to be an essential component of any plausible cosmological model.

Though brief in duration, inflation bestows an exponential expansion upon any spatial scale existing in the universe at that time. This drives causally connected patches of space to super-horizon scales thereby creating the appearance of homogeneity and isotropy on scales larger than the horizon at any time. Furthermore, perturbations in the matter field generated by quantum zero-point motions are stretched to cosmically relevant scales thus providing the gravitational seeds that can later grow into the array of structures we see in the universe today. Since gravity is a purely attractive force these minute density perturbations can only be amplified by its influence.

Different theories of inflation predict that the power spectrum[‡] of primordial density perturbations is very close to a power-law:

$$P(k) \propto k^n, \tag{1.1}$$

[‡]In general, a power spectrum provides a measure of the portion of a signals total power that lies in a given frequency bin, or at a given wavenumber. In cosmology, the power spectrum can be used to describe the large-scale clustering of galaxies, the distribution of temperature fluctuations on the CMB, or the fluctuation spectrum of primordial density perturbations predicted by inflation.

so that the mass variance is given by

$$\sigma_k^2 \propto \int_0^k dK K^{2+n} \propto k^{3+n}. \tag{1.2}$$

In cosmology, the most important power spectrum is the Harrison-Zeldovich scale-invariant spectrum, which has $n = 1$. Apart from its simplicity, a power spectrum with $P(k) \propto k$ is predicted by many theories of inflation, although the initial interest in such a power spectrum was motivated by a much simpler arguement. In general relativity, fluctuations in the metric tensor are of order Φ/c^2, where Φ is the gravitational potential associated with the density fluctuations. In the case that fluctuations in Φ are too large on large scales, the assumption of homogeneity and isotropy break down; if the fluctuations are too large on small scales, the resulting small scale structures will be relativistic. The Harrison-Zeldovich $n = 1$ spectrum is the critical case in which the RMS potential fluctuations are independent of scale. To see this, consider the RMS density fluctuation on scale k^{-1} for an arbitrary power-law power spectrum: $\rho_{RMS}(k) \approx \rho_0 \sigma_k \propto k^{(3+n)/2}$. The corresponding RMS mass fluctuation is $M_{RMS}(k) \approx \rho_{RMS} k^{-3} \propto k^{(n-3)/2}$, so that the fluctuation in the gravitational potential is $\Phi_{RMS}(k) \approx G M_{RMS}(k) k \propto k^{(n-1)/2}$. This suggests that RMS fluctuations in the gravitational potential are scale-invariant if and only if $n = 1$.

1.3.2 Gravitational Instability in Linear Theory

The end of inflation is marked by a period of reheating in which the inflaton decays into a hot, thermal plasma of elementary particles. The energy density of the universe at this time is entirely dominated by radiation, which is strongly coupled to the baryons through Thompson scattering, forming a relativistic plasma. As the universe continues to expand and cool the energy density associated with the radiation field decreases more quickly than that of the matter constituents. Eventually,

at $z = z_{eq}$, the dynamics of the expansion becomes matter dominated.

At early times, the amplitude of density perturbations δ is small, $|\delta(x)| \ll 1$, and the essential physics describing their evolution can be captured in a simple Newtonian approach. The dynamics of density perturbations depends greatly on both the perturbation scale, and whether the universe is dominated by radiation or by non-relativistic matter. In the following, we we consider the two limiting cases of whether inhomogeneities are dominated by a relativistic fluid, or by non-relativistic matter.

Non-relativistic Fluid Limit

For simplicity we assume that the cosmic material behaves like a fluid, and that analogues to the Euler and continuity equations describe its evolution. By linearizing these equations, one can show that the evolution of a density perturbation, δ_k, on scale k^{-1}, is governed by a simple differential equation:

$$\frac{\partial^2 \delta_{\mathbf{k}}}{\partial t^2} + 2H\frac{\partial \delta_{\mathbf{k}}}{\partial t} + \left(\frac{k^2}{a^2}v_s^2 - 4\pi G\rho_0\right)\delta_{\mathbf{k}} = 0, \tag{1.3}$$

where, ρ_0 and $\delta_{\mathbf{k}}$ are, respectively, the undisturbed density and the disturbed value, $H = H(z)$ is Hubble's constant, a is the expansion factor, and v_s the sound speed.

Neglecting radiation and vacuum energy, one can show that the solution to eq. 1.3 for a long wavelength (small k) perturbation is a linear combination of growing and decaying power-laws,

$$\delta_{\mathbf{k}} \propto t^{2/3} \quad \text{and} \quad \delta_{\mathbf{k}} \propto t^{-1}, \tag{1.4}$$

with the growing mode dominating after a short time interval. This aplies in the special case in which the universe is dominated by matter, which approximately holds over the interval $3100 \gtrsim z \gtrsim 0.5$, in which most cosmic structures form. In the present and future epoch, where the dynamics is dominated entirely by

the energy density of the vacuum, H is a constant and $4\pi G\rho_0 = \frac{3}{2}H^2\Omega_m$ rapidly becomes neglidgible. In this case, eq. 1.3 reduces to

$$\frac{\partial^2\delta_{\mathbf{k}}}{\partial t^2} + 2H\frac{\partial\delta_{\mathbf{k}}}{\partial t} = 0, \tag{1.5}$$

which has the general solution

$$\delta_m(t) = A + B\exp(-2Ht), \tag{1.6}$$

for constant A and B. Thus, in a universe dominated by non-relativistic matter fluctuations grow as $t^{2/3}$, but at later times, when $z_{m\Lambda} \approx 0.5$, the growth freezes out and subsequent growth is suppressed.

Relativistic Fluid Limit

For $z > z_{\gamma m}$, the expansion dynamics of the universe is dominated by radiation. The energy density associated with the radiation field declines as a^{-4}; a factor of a^{-3} describes the rate of change of photon number density, with an additional factor of a^{-1} associated with the decrease in photon energy due to redshifting. Hence, the continuity equation is not satisfied by the mass-energy density of the radiation field, and eq. 1.3 cannot be used to describe the evolution of a perturbation. However, since the mean free path of a photon is very short during this epoch, the photon *entropy* does satisfy a continuity equation. As above, linearizing and combining the continuity and Euler equations yeilds

$$\frac{\partial^2\delta_{\mathbf{k}}}{\partial t^2} + 2H\frac{\partial\delta_{\mathbf{k}}}{\partial t} + \left(\frac{k^2c^2}{3a^2} - \frac{32}{3}\pi G\rho_0\right)\delta_{\mathbf{k}} = 0, \tag{1.7}$$

where c is the speed of light. During the radiation-dominated era we have $2H = t^{-1}$ and $\frac{32}{3}\pi G\rho_0 = t^{-2}$, and eq. 1.7 becomes

$$\frac{\partial^2\delta_{\mathbf{k}}}{\partial t^2} + \frac{1}{t}\frac{\partial\delta_{\mathbf{k}}}{\partial t} + \left(\frac{k^2c^2}{3a^2} - \frac{1}{t^2}\right)\delta_{\mathbf{k}} = 0. \tag{1.8}$$

The behaviour of the solutions to eq. 1.8 depends on whether a given fluctuation is inside the current horizon, or whether it spans causally disconnected regions. For sub-horizon sized fluctuations, $a/k \gtrsim ct$, and the first term in the brackets of eq. 1.8 dominates the second. In this case, the solution $\delta_m(t)$ is oscillatory: perturbations smaller than the horizon are stabilized by radiation pressure. For long wavelength perturbations, on the other had, we can neglect the bracketed term. In this case solutions are, again, linear combinations of power-laws:

$$\delta_{\mathbf{k}} \propto t \quad \text{and} \quad \delta_{\mathbf{k}} \propto t^{-1}. \tag{1.9}$$

Hence, during this epoch sub-horizon density fluctuations imprinted during inflation do not evolve significantly. Growth of perturbations in the dark matter is suppressed by the rapid expansion of space driven by the radiation pressure. This is because the characteristic expansion timescale $(G\rho_\gamma)^{-1/2}$ is much shorter than the characteristic growth time $(G\rho_{DM})^{-1/2}$ for fluctuations in the matter density. In a sense, dark matter fluctuations do not have time to grow. Perturbations in the relativistic photon-baryon fluid, on the other hand, have their growth halted by the very large pressure forces associated with the plasma. These pressure forces suppress the growth of all structures smaller than the Jeans length, which is roughly equal to the horizon during this time.

Although the growth of perturbations is highly suppressed during this epoch, their *evolution* is responsible for generating the anisotropy pattern in the cosmic microwave background radiation (CMB). Fluctuations that cross the horizon during this time immediately encounter their Jeans length and begin to oscillate with a

frequency that is related to the perturbation scale. Once the radiation energy density redshifts below that of the matter constituents, the expansion rate slows and matter begins to dominate the energy density of the universe. The combination of electrons, protons, and neutrons into electrically neutral atoms liberates the primordial radiation field, which consequently loses its grip on the baryons. These photons represent a "snapshot" of the universe as it appeared at recombination and the different acoustic modes appear as peaks in its power spectrum.

Dark matter provides the driving force for the acoustic oscillations in the photon-baryon plasma. Hence, the overall shape and amplitude of the CMB power spectrum, as well as the subsequent evolution of the matter power spectrum, is uniquely sensitive to the abundance and type of dark matter in the universe. Accurate measurements of the CMB and galaxy power spectra (see e.g. Spergel et al 2007; Dunkley et al 2008) indicate, with a high degree of confidence, that the dark matter outweighs the luminous baryons by a factor of roughly 20.

The present-day overdensity of structure on galactic scales also suggests the existence of a large dark matter component. As the universe expands it eventually becomes matter dominated, the expansion timescale slows, and perturbations in the dark matter are able to grow on all scales. The baryons, however, remain coupled to the photons until recombination, at which point the mean free path of photons increases substantially over a short, but finite, time interval. Hence, there is a period in which the the baryons remain coupled to the photons, but the photon mean free path is not small. This results in the diffussion of baryons out of of potential wells on scales smaller than the horizon, a process known as Silk damping (Silk 1968). In fact, all fluctuations in the baryonic matter below the scale of rich galaxy clusters ($\approx$ 10 Mpc) are erased by this process. Thus, if it were not for fluctuations in the dark matter we would expect to see no structures on scales below that of rich galaxy clusters. However, existing dark matter fluctuations are "hidden" by the smooth distribution of baryons, and provide the underlying potential wells that

force the baryons to "catch-up" to their distribution, thereby creating the small scale structures observed today.

Initial conditions for N-body simulations typically start at redshifts or order $100(\ll z_{\rm recomb})$. Because of this, the adopted primordial power-spectrum will have been modified significantly from its original form by the start of the simulation. Process such as growth under self-gravity, and the effects of pressure and dissipation all modify the primordial power-spectrum in non-trivial ways, typically reducing the amplitudes of short wavelength modes relative to long ones. The overall effect of these processes are encapsulated by the Transfer function, $T_k(k)$, which describes the late-time amplitude of a given mode to its initial value; i.e. $T_k = \delta_k(z = 0)/(\delta_k(z)D(z))$, where $D(z)$ is the linear growth factor.

For a any given cosmological model the transfer function must be calculated explicitly. This can be done using publicly available codes, such as CMBFAST (Seljak & Zaldarriaga 1996), which solve the Boltzmann equation in order to follow the evolution in detail. For the concordance ΛCDM cosmological model, the transfer function modifies the primordial Harrison-Zeldovich power spectrum such that, asymptotically,

$$P(k) = \begin{cases} kx_{\gamma m} & \text{if } kx_{\gamma m} \lesssim 1 \\ (kx_{\gamma m})^{-3} & \text{if } kx_{\gamma m} \gtrsim 1. \end{cases} \tag{1.10}$$

In other words, the power spectrum is unmodified on large scales, and proportional to the primordial power spectrum. On smaller scales, however, the power spectrum asymptotes to a power-law for large k with a slope of -3. We shall see below that a power spectrum of this form predicts that structures form hierarchically.

1.3.3 Spherical Collapse and Hierarchical Structure Formation

We can gain an intuitive grasp of the hierarchical nature of structure formation in CDM cosmogonies by considering the spherical collapse of an initial overdensity, δ, in a flat, matter-dominated Friedmann-Robertson-Walker model. The assumption that the universe is matter dominated is a reasonable one between $z_{\gamma m} \backsimeq 3100$ and $z_{m\Lambda} \backsimeq 0.5$, the interval over which most cosmic structures form.

We consider the case of a small spherically symmetric density fluctuation at some early time t_i, such that the average density inside radius r_i is $\delta_i \ll 1$. Far outside this sphere the density is given by

$$\rho_m(t) = \frac{1}{6\pi G t^2}, \tag{1.11}$$

and the total mass contained within r_i is

$$M = \frac{4\pi}{3}(1+\delta_i)\rho_m(t_i)r_i^3. \tag{1.12}$$

The equation of motion describing the evolution of a spherical shell, initially at radius r_i, is

$$\frac{d^2r(t)}{dr^2} = -\frac{GM}{r(t)^2}. \tag{1.13}$$

The gravitational acceleration of this shell is determined entirely by the mass, M, contained within it, which is constant during the evolution. Eq. 1.13 is similar to that describing the motion of a projectile launched vertically from the surface of a body of mass M, and its solution (assuming that $r = 0$ at $t = 0$) may be written parametrically as

$$r = a(1-\cos\nu) \quad ; \quad t = \sqrt{\frac{a^3}{GM}}(\nu - \sin\nu). \tag{1.14}$$

The "turn around" radius, $r_{\max} = 2a$, is the distance at which the mass shell turns around and collapse commences; it occurs at $\nu = \pi$. The average density inside the sphere is $\rho_s(t) = M/\frac{4}{3}\pi r^3(t)$, and hence

$$\begin{aligned} \delta(t) &\equiv \frac{\rho_s(t)}{\rho_m(t)} - 1 \\ &= \frac{9}{2}\frac{(\nu - \sin\nu)^2}{(1-\cos\nu)^3} - 1. \end{aligned} \tag{1.15}$$

For small density contrasts eq. 1.15 can be expanded in a power series to obtain

$$\delta(t) \backsimeq \frac{3}{20}\nu^2 + 0(\nu^4). \tag{1.16}$$

A similar expansion on the first equation in 1.14 can be used to eliminate r_i from eq. 1.12, resulting in an estimate of the turnaround radius:

$$r_{\max} = 2a \backsimeq \left(\frac{243}{250}\right)^{1/3} \frac{(GMt_i^2)^{1/3}}{\delta_i}. \tag{1.17}$$

The corresponding turnaround *time* is

$$t_{\max} = \pi\sqrt{\frac{a^3}{GM}} = \pi\left(\frac{243}{250}\right)^{1/2} \frac{t_i}{\delta_i^{3/2}}, \tag{1.18}$$

which is proportional to $\delta_i^{-3/2}$; the larger the initial fluctuation δ_i, the sooner the collapse commences. Since the initial RMS density fluctuations are roughly given by $\rho_{RMS}(k) \approx \rho_0\sigma_k \propto k^{(3+n)/2}$, it follows that the initial (RMS) overdensity is the largest on small scales (i.e. large wavenumbers k) in the CDM cosmogony. In such a universe structure formation proceeds hierarcically; small scale objects are the first to become non-linear, their subsequent merger and accretion contributes to the formation of progressively larger structures.

1.4 Problems, Alternatives, and Solutions

Although extensive numerical work over the past couple of decades aimed at testing cosmological models has led to a concordance Λ-cold-dark-matter scenario, the fine details of this paradigm are not yet fully ironed out. The structure formation scenario described in § 1.3 tells how halos of dark matter form in a hierarchical manner, through the merger and accretion of smaller halos. Since dark matter is considered to be predominantly cold, the negligible thermal velocities of the particle at decoupling allow for clustering to occur on essentially all scales. The small scale fluctuations that collapse at early times have very high central densities, reflecting the density of the universe at the time of collapse (Navarro, Frenk & White 1996, 1997; hereafter NFW collectively). These high densities make early forming low mass halos resilient to the effects of tidal stripping and disruption; small scale objects tend to be very long lived in the CDM cosmogony, even in the presence of more massive gravitational potentials.

One implication of this is that galaxies, such as our own Milky Way, should be home to hundreds, or perhaps thousands of "satellite" galaxies (Klypin et al 1999; Moore et al 1999). This is very different from the roughly 20 satellites observed around the Milky Way. The lack of observational evidence for the expected abundance of substructure on small scales has led some to question the validity of the CDM paradigm.

A related issue concerns the internal structure of dark matter halos. Numerical simulations of structure formation consistently produce dark matter halos with steeply divergent central density profiles, which asymptote to approximate power-laws ($\rho \sim r^{-1}$) at small radii (NFW). These "cusps" form from the low-entropy material of previous generations of disrupted halos, which accumulates at the center of larger systems; cusps are ubiquitous in CDM cosmogonies (NFW, Fukushige & Makino 1997; Moore et al 1998; Kravtsov et al 1998; Moore et al 1999a; Ghinga et al 2000; Klypin et al 2001; Navarro et al 2004; Merritt et al 2005). The particles' lack

of thermal energy cannot prevent the collapse leading to steeply divergent central densities.

The cuspy structure of dark matter halos is, however, at odds with the interpretation of some observational data sets. In particular, several authors have studied the dynamics of low surface brightness (LSB) galaxies and found better agreement with cored distributions of dark matter (Flores & Primack 1994; Moore 1994; Burkert 1995; de Blok et al 2001a,b). Similar results come from observations of strong lensing by galaxy clusters, where the presence of radial and tangential arcs allow for a determination of the cluster mass profile, which again suggests a shallower central density profile than predicted by N-body simulations (see, e.g., Sand et al 2004). However, the interpretation of these observations is hindered by simplistic modeling and a poor account of the baryonic processes that inevitably alter the distribution of dark matter in the inner halo regions (see Hayashi et al 2004, 2006; Bartelmann & Meneghetti 2003).

The problems with substructure and cusps in CDM cosmogonies have led some to suggest that a new paradigm for structure formation must be adopted in order to fully explain all observations in a consistent way. The most commonly discussed remedy is to invoke some degree of hot dark matter. The suppression of small scale power in these models will simultaneously alleviate the abundance of substructure in the halos of galaxies like the Milky Way, and may suppress the formation of steep cusps in halo centers (but see Wang & White 2008). In HDM scenarios the dark matter particles are massive neutrinos with a free-streaming length (just the collisionless analogue of the Jeans length) of several megaparsecs. The first structures to form in these models are superclusters and voids, which attain sizes roughly consistent with the observational data. The abundance and clustering of galaxies, however, which form later through secondary fragmentation processes, is significantly lower than observed, making pure HDM models an unlikely alternative to CDM.

Perhaps if CDM is too cold, and HDM is too hot, then some combination of the two may provide a *warm* dark matter (WDM) model which is in accord with observations. This was investigated numerically by Colombi et al (1996) in a series of simulations in which the free streaming length, l_s, was systematically varied. These authors found that if l_s was chosen to match large-scale structure, then there was still too much power on small scales.

Simulations of warm dark matter cosmogonies were also performed more recently by Yoshida et al (2003) assuming, as in Colombi et al, a truncated power spectrum below the free streaming scale. These authors argue that the absence of low mass halos at high redshift in the WDM cosmogony inhibits the formation of primordial gas clouds containing molecular hydrogen, which would otherwise provide the fuel for the first generation of stars. As a consequence, reionization is delayed significantly with respect to what one expects for CDM cosmological models, and appears inconsistent with the optical depth if the inter-galactic medium inferred from WMAP observations.

It should be noted, however, that warm dark matter cosmological models are notoriously difficult to simulate. The intrinsic velocity distribution of the dark matter particles has to be calculated explicitly for a given particle model, and properly incorporating this thermal distribution into cosmological initial conditions is non-trivial. To aviod the associated complications it is often assumed (as in Colombi et al 1996, and Yoshida et al 2003) that the dark matter is "cold", but follows a power spectrum that is artifically truncated below the free-streaming scale.

Other modifications of cosmological theory aimed at finding solutions to the above problems involve modifying the initial conditions of structure formation by, for example, introducing a non-Gaussian density fluctuation spectrum (LoVerde et al 2007; Afshordi & Tolley 2008; Carbone et al 2008). Changes in the "tilt" of the primordial power-spectrum (i.e. tilting the power spectrum of density fluctuations towards large scales) have also been considered (e.g. Bullock 2001), or, finally,

by making a large conceptual leap into the realm of modified gravity (Milgrom 1983a,b,c; Bekenstein 2004).

In recent years a careful look at the CDM model itself has been able to provide less drastic solutions to its own troubles. For example, much of the observational data on which the inference of cored dark matter halos was based had been interpreted in a rather simplistic manner. Many authors made the assumption that the mass distribution in dark matter halos is spherically symmetric, and concluded that *spherically symmetric cuspy* dark matter halos were inconsistent with their observations. N-body simulations, however, indicate that dark matter halos have a strongly triaxial shape, with a slight preference for nearly prolate systems. These interpretations have thus been called into question and more detailed analysis of the available data, which includes the effects of structural asymmetry, have been shown to significantly relax the constraints on dark matter halo mass profiles (e.g. Bartelmann & Meneghetti 2003, Hayashi & Navarro 2004).

The abundance of dark matter satellites found in numerical simulations of galaxy formation is inarguably at odds with observations. However, this inconsistency may be driven by the complex baryonic physics that occurs during the formation of galaxies. Processes such as photo-ionization, photo-evaporation, and feedback from stellar sources and active galactic nuclei, though poorly understood, may significantly suppress gas cooling in low mass halos. Thus, halos below some critical mass scale may be stripped of their gas and end up completely devoid of stars. Such a proposal has gained strong footing in light of recent weak lensing surveys of galaxy halos that claim to require *more* substructure than can be observed directly (Dalal & Kockanek 2002).

1.5 Numerical Cosmology

Numerical simulations have evolved over the past couple of decades to become an essential theoretical tool to accompany, motivate, and help interpret many astrophysical and cosmological observations. The premise of structure formation models is to reduce the evolution of the universe to an initial boundary problem. Here one specifies the initial state of the universe at some early time, assumes a dynamical background model, and evolves the system to the present day using Newtonian gravity. Such simulation work provides an invaluable bridge between observational and theoretical astrophysics, and allows for the detailed study of complex systems that can not be studied analytically.

The scope of N-body simulations has increased dramatically over the past couple of decades, and the methods by which these simulations are performed have been refined and adapted to suit specific numerical problems. The work presented in this thesis follows a technique commonly referred to as numerical *re-simulation* (e.g. Porter 1985). In the remainder of this section we briefly describe the numerical issues relevant to our simulations. This will include a overview of the adopted codes, the procedure for generating initial conditions, as well as a summary of the major published results relevant to the work presented in later Chapters.

1.5.1 N-body Methods

The spirit of the N-body method is to discretize a representative volume of the universe by coarsely sampling its phase-space structure with N point-mass particles. A set of initial conditions describing the state of the system at time t_1 allows the equations of motion to be integrated forward to any other time t_2. The number of particles used to sample a given volume of phase-space dictates the numerical resolution of that region; a finer sampling of the initial distribution function results in a higher resolution simulation. Many current simulations, such as those presented

here, rely on complex asymmetric multi-mass samplings. This allows for simulating specific regions within a much larger volume with controlled resolution.

Initial Conditions

Using N-body simulations to make accurate quantitative predictions about the evolution of structure in the universe relies heavily on having an accurate description of the initial state of the system. Subtle errors present in the initial conditions may extrapolate to large errors by the end of the simulation, and should be suppressed from the start. The specific methodology employed in setting up reliable initial conditions for astrophysical simulations depends greatly on the type of simulation one wishes to perform. In this thesis we study the formation and evolution of individual dark matter halos in a fully cosmological context. The manner of generating initial conditions for such simulations has been described in detail in the literature. For this reason we here give only a brief outline of the method for the sake of completeness, and refer the reader to more detailed descriptions given elsewhere (e.g. see Power et al 2003; Hayashi et al 2004; Navarro et al 2004; Springel et al 2008).

The first stage is to carry out a "parent" simulation of a representative volume of the universe, sufficiently large so that the matter fluctuations on the largest scales remain in the linear regime until $z = 0$. The parent simulation is then used to isolate groups or individual halos for resimulation at higher resolution. Once a halo of interest is identified, all particles in a sufficiently large Lagrangian volume surrounding the halo are traced back to the unperturbed configuration at $z = \infty$. A cube just large enough to encompass the volume occupied by these particles is then re-sampled at higher resolution than the parent run, with the remainder of the simulation volume sampled at lower resolution. Care is taken to ensure that the volume surrounding the halo retains sufficient structure to apply the appropriate tidal forces to the high resolution particles.

The high resolution region itself is initially set up as a uniform distribution of

particles, such as a cubic grid, or glass. The simulation volume outside the high-resolution cube is layered with concentric cubic shells of evenly spaced particles, whose inter-particle separation increases roughly linearly with distance from the high resolution region outward. For expediency we "clip" the particles in the high resolution box that do not end up in the final object by replacing them with particles of larger mass, for example, by combining several high-resolution ones. The result is an amoeba shaped region consisting of high resolution particles embedded in a lower resolution environment. This "clipping" significantly reduces the force integration time required to evolve the system from the initial to final redshifts.

Having set a multi-mass, uniform matter field the next step is to apply the required Gaussian density fluctuation spectrum. This is achieved by perturbing the particle positions and assigning peculiar velocities using Fourier methods. Using the same Fourier amplitudes and phases present in the parent simulation one can very accurately reproduce the original density field on the new particle distribution. The lower particle mass in the high resolution region requires the input of additional power in the form of higher frequency modes which extend to the Nyquist limit imposed by the new particle grid. Growing modes are achieved using the Zel'dovich approximation by making the peculiar velocities of particles proportional to their displacements (Zel'dovich 1970). This process leads to a new realization of the cosmological initial conditions of the parent simulation in which the vast majority of computational effort will be put into resolving the evolution of one small patch of space.

Numerical Codes

Evaluating gravitational accelerations and solving the equations of motion are two key steps employed by every N-body code. The long-range nature of the gravitational force indicates that the force contribution from distant particles can not be ignored. As a result, the force calculation is the most time consuming aspect

of any N-body simulation. In recent years a lot of attention has been devoted to addressing this issue and, today, a number of algorithms are available to N-body practitioners.

The simulations presented here were performed primarily with the publicly available N-body code `Gadget2` , written by Volker Springel (Springel 2005), but also its successor, `Gadget3`, by the same author. In the following subsections we briefly describe the code, as well as its associated post-processing algorithm, `SUBFIND` .

GADGET

`Gadget2` is a publicly available cosmological N-body/SPH code tailored for simulations on massively parallel computers with distributed memory. It combines a tree-based force calculating algorithm with an (optional) particle-mesh scheme for long-range gravitational forces. `Gadget2` can be used for idealized studies of isolated or merging objects, as well as for fully cosmological simulations of structure formation both with periodic and vacuum boundary conditions.

The force computation and timestepping scheme are both fully adaptive for all particles. In its default mode the code caries, for each particle, an estimate of the local gravitational acceleration, a_i, and the force softening, ϵ_i, which is kept fixed in comoving units. This is used to define a timestepping criterion in which the step-size is chosen according to

$$\Delta t_i \propto \sqrt{\epsilon_i / a_i}. \tag{1.19}$$

Thus, particles in low-density environments, where the gravitational accelerations are small, take relatively long timesteps compared to those experiencing large accelerations in high density regions. The adaptivity of particle timesteps is important for simulations of the type presented in this thesis because of the large dynamic range they achieve.

The simulations presented in Chapter 3 were carried out with a new version of the `Gadget` cosmological simulation code, which we refer to as `Gadget3`. This more recent algorithm implements a novel domain decomposition strategy in order to achieve unprecedented dynamic range without sacrificing load balancing or numerical accuracy.

In both `Gadget2` and `Gadget3` the particle pairwise interactions are softening with a spline length h_s, so that forces become strictly Newtonian for particle separations larger than h_s. This is roughly equivalent to the Plummer-softening with a scalelength $\epsilon_G \sim h_s/1.4$. The softening lengths are kept fixed in comoving coordinates so that the phase-space density of the discretized particle system is strictly conserved during the evolution (see Springel et al 2005 for a discussion).

`SUBFIND`

There are plenty of algorithms described in the literature whose primary purpose is to identify structures in dissipationless simulations. Generally speaking, these algorithms are, to some extent, geometrical; a structure is defined as a group of particles whose nearest neighbor separation (or local density) meets some specified threshold. Halos of dark matter identified in this way are often referred to as friends-of-friends (or FOF) halos, because of the linking of nearby particles into groups. This geometrical definition of a structure is limited, but sufficient for purposes in which one is not concerned with the internal structure of substructure (e.g., as in Mao et al 2004; Hagan et al 2005; Amara et al 2006; Hennawi et al 2007). If instead one wishes to trace the evolution of a single halo, or groups of halos, or to quantify their internal properties, then those structures must be defined in a dynamically consistent way.

The internal structure of dark matter halos and subhalos has specific relevance to the material presented in Chapters 2, 3, and 4. Hence, we employ a two step technique for identifying the particles belonging to a certain substructure halo: one

geometrical, to identify dark matter clumps; the other dynamical, to test whether they are self-bound. The first stage defines the base-level dark matter structure; instantaneous particle positions are used to group together nearby particles into localized objects. Next, each geometric structure is treated with a dynamical unbinding procedure to obtain the gravitationally bound substructure of each object by separating self-bound groups of particles from the background.

We use the algorithm `SUBFIND`, written by Volker Springel and described in Springel et al (2001). `SUBFIND` isolates dark matter substructures within larger halos by locating overdense regions and finding the subset of particles bound to each overdensity. The algorithm works recursively and can be used to identify subhalos within subhalos, thereby characterizing the full structural hierarchy of an object.

1.5.2 The Structure of Dark Matter Halos

Much of our present understanding of the structural properties of dark matter halos has been derived from the results of N-body simulations of their formation. Over the past couple of decades simulations of increasingly high resolution have been performed with the goal of more deeply probing the structure and substructure of dark matter halos. The highest resolution simulation published to date is the so-called Aquarius simulation (Springel et al 2008a,b; Navarro et al 2008). This simulation follows the formation of a single Milky Way sized dark matter halo with $N_{200} \approx 10^9$ particles (a first time achievement for simulations of this kind), and is accompanied by a sample of six additional halos, simulated with between 100 and 200 million particles.

Early analytic (Gunn & Gott, 1972; Fillmore & Goldreich 1984; Hoffmann & Shaham, 1985; White & Zaritsky, 1992) and numerical studies (Frenk et al 1985; Quinn et al 1986; Dubinski & Carlberg, 1991; Crone et al, 1994) first suggested that the density profile of dark matter halos follow a simple power-law, $\rho \propto r^{-2}$, similar

to that of an isothermal sphere. As the sophistication of numerical simulations increased, this simple density stratification was abandoned for a more complex behavior. Particularly, Navarro, Frenk & White (1996, 1997) used a series of N-body simulations to show that halos spanning a wide range of masses follow a nearly "universal" form, with

$$\rho_{\rm NFW} = \frac{\rho_s}{(r/r_s)(1+r/r_s)^2}, \tag{1.20}$$

where r_s is a characteristic radial scale at which $\mathrm{d}\ln\rho/\mathrm{d}\ln r = -2$, the "isothermal" value. This is the so-called NFW profile, which has since become the fiducial parametrization of dark matter structure against which many observational data sets are compared.

Subsequent simulation work questioned both the universality and the inner asymptotic slope advocated by NFW, but there is now a working consensus that dark matter halos are "cuspy" with profiles that gradually become shallower towards the center. Two particular studies of note are those of Navarro et al (2004), and Gao et al (2007). In the first of these, the density distribution of a suite of 16 simulated dark matter halos was shown to be better fit by the 3-parameter Einasto profile (Einasto 1965) than the universal form of eq. 1.20. The Einasto profile is characterized by a power-law logarithmic slope;

$$\ln(\rho(r)/\rho_{-2}) = -(2/\alpha)[(r/r_{-2})^\alpha - 1], \tag{1.21}$$

where α is an additional parameter that can be tailored to fit each individual halo. Subsequently, Gao et al (2007) used the unprecedented statistics and dynamic range of the Millennium simulation (Springel et al 2001) and by stacking halos of a given mass was able to show that the Einasto parameter, α, is weakly dependent on halo mass. Massive rare objects, such as galaxy clusters, have $\alpha \approx 0.3$, whereas $\alpha \approx 0.15$ at the galaxy scale. This indicates that, at the galaxy scale, dark matter halos have, on average, steeper density profiles than those of clusters; an interesting empirical

result that we discuss further in Chapters 3 and 4.

Apart from the density profile, universality has also been reported in several other structural and dynamical properties of dark matter halos: a) the cumulative angular momentum profile (Bullock et al 2001); b) the density slope versus velocity anisotropy (Hansen & Stadel 2006; Hansen & Moore 2006); and c) the pseudo phase-space density profile, ρ/σ^3 (Taylor & Navarro 2001). The first two of these have not been discussed heavily in the literature, though the third is thought by many to hold some fundamental importance. The reason for this is as follows. Dark matter halos that form as a result of dissipationless hierarchical merging develop a (nearly) universal density profile with a complex radial dependence. Complementary studies that follow the growth of dark matter halos (semi-)analytically (e.g. Bertschinger 1985; Williams et al 2004; Austin et al 2005; Barnes et al 2006, 2007) show a wide variety of relaxed density structures, from simple power-laws to ones that resemble the NFW profile. However, despite the differences in the radial behavior of $\rho(r)$, a common feature is the development of a power-law pseudo-phase-space density profile, quantified by ρ/σ^3. This result is a strong indication that some common gravitational process leads to a simple scaling between the densities and velocities across the system.

Despite the breadth of knowledge pertaining to dark matter halo structure there is no compelling theoretical argument for the existence of either a universal density or phase-space density profile, nor why there should exist a coupling that produces power-law phase-space density profiles. A deeper understanding of either of these structural properties will inevitably shed light on the others. In Chapters 3 and 4 of this thesis we examine the density and phase-space density profiles of a suite of high resolution dark matter simulations in hope of exposing the processes by which dark matter halos attain their unique but similar structure.

1.5.3 The Substructure of Dark Matter Halos

Perhaps the closest observational analogue to the substructures inhabiting simulated dark matter halos are the luminous galaxies found in galaxy clusters. The fact that the subhalo mass function of simulated clusters agrees well with the *luminosity* function of cluster galaxies (Natarajan & Springel 2004) suggests that the cluster galaxies probe, observationally, one level of the merger hierarchy. The bottom-up picture of standard ΛCDM models indicate, however, that each subsequent level was built up in a similar way, through mergers and accretion; to first order, individual galaxy halos in galaxy clusters are expected to resemble scaled down versions of the clusters themselves. However, due to the complex baryonic processes operating on galactic and sub-galactic scales it is difficult to find observational verification for any further levels of the accretion hierarchy. In numerical simulations, where the full six dimensional phase-space coordinates are known, a close examination of any (sufficiently resolved) object should reveal the undigested cores and tidal debris from past accretion events.

Though substructure halos make up a very small fraction of the total mass of a halo (between about 5% and 10%) their structural properties, spatial distribution and dynamics are of great interest. These *subhalos* are potential sites for the formation of galaxies in clusters, or of dwarf galaxies observed in the Local Group. Thus, a detailed understanding of their evolution and structure is a prerequisite for unravelling the complex formation history of the Milky Way and other galaxies.

In recent years, much attention has been devoted to quantifying the basic properties of individual subhalos as well as the population as a whole (Ghinga et al 1998, 1999; Moore et al 1999; Taylor & Babul 2005a,b; Benson 2005; Gao et al 2004; Diemand et al 2007a,b). One key statistic, the substructure mass function, has been found to follow a power-law with $dN/dM \propto M^{-1.9}$, which is a strong indication that the total mass fraction found in substructure is is dominated by the few most massive substructures (Springel et al 2001; Gao et al 2004). The spatial

distribution and kinematics of subhalos has been found to be strongly biased relative to the distribution of both the dark matter halos in which they are embedded, as well as to the observed distribution of galaxies in clusters, and to visible satellites of the Milky Way (see. e.g. Kravtsov 2001; Willman et al 2004; Madau et al 2008). Thus, the correspondence between simulated subhalos and the *luminous satellites* of galaxies is not one-to-one. This highlights the complex role of baryonic physics in molding the properties of the galaxy population.

The spatial distribution and dynamics of subhalos has also been found to be largely independent of subhalo mass. Combined with the observation that subhalos follow different radial distributions than Local Group satellites, this indicates that evolutionary effects, such as tidal mass loss and dynamical friction, must be considered in attempts to "match-up" subhalos with visible objects.

Studies of the substructure population of CDM halos, including their spatial distribution and internal structure, have been revitalized recently by the possibility of observing directly the dark matter particles, either by their annihilation signal in the gamma-ray sky (Stoehr et al 2003; Diemand et al 2007; Kuhlen et al 2008; Springel et al 2008a), or through direct detection here on Earth. For both avenues, a more detailed quantitative understanding of the distribution of dark matter in the Milky Way and its subhalo population is urgently needed.

1.6 In this Thesis

Studies of the structure of dark matter halos and the properties of their substructure populations have a rich history in the astronomical literature. Since the early analytic work of Gunn & Gott (1972) the significant increase in computational resources has led to impressive strides in our understanding of the structure of dark matter through the use of N-body simulations. Some notable results have been the characterization of the inner structure of dark matter halos (Navarro et al 1997,

1998; Ghinga et al 1998; Moore et al 1999; Gao et al 2007; Navarro et al 2008); the predictions of gamma-ray annihilation flux from dark matter in the Milky Way galaxy (Delahaye et al 2008; Kuhlen et al 2008; Springel et al 2008); the internal structure of dark matter subhalos (Diemand et al 2007; Madau et al 2008; Springel et al 2008a,b); and the statistics of the substructure population in galaxy-sized halos (Diemand et al 2008a,b; Springel et al 2008a,b).

The results presented in this thesis build upon this body of work by using a sample of high-resolution simulations to investigate the structure and substructure of cold dark matter halos. In Chapter 2 we use a suite of 11 simulated galaxy-sized halos to study the dynamical properties of the substructure population that are *physically associated* with their host galaxy. We place particular emphasis on dynamical outliers in the subhalo population and, by tracing the detailed mass accretion and orbital histories of each surviving subhalo, we pin-point the physical mechanism responsible for generating unorthodox orbits. We quantify the spatial and dynamical distributions of associated subhalos, as well as as the dependence of these distributions on subhalo mass.

In the first few sections of Chapter 3, we study the basic statistics of the substructure population found in a series of six galaxy-sized dark matter halos. In particular, we quantify the mass and peak circular velocity distributions, estimates of the total substructure mass fraction, as well as the spatial distribution and dynamics of subhalos as a function of their mass. This allows us to test directly several conclusions drawn from the results of Chapter 2, as well as other work. Where applicable, we contrast out results directly against those of other groups.

In the later sections of Chapter 3 we use the same set of six simulated objects to quantify the structure and dynamics of the host dark matter halos. One of these halos has been simulated five times, with mass resolution increasing by about a factor of 2000 between the lowest and highest resolution runs. This allows us to asses directly issues related to numerical convergence (both in the main halos

and its substructure population), as well as halo-to-halo scatter. We concentrate our analysis on the structure of the main halo; by focusing on the halo's inner regions we are able to bypass uncertainties related to the presence of substructure and unrelaxed tidal debris in the outer regions of the halo. We quantify the basic structural properties of each main halo: the mass profile, the asymptotic behavior of the inner cusp, the velocity structure, as well as the pseudo-phase-space density profile.

In Chapter 4 we investigate several issues raised in Chapter 3 regarding the self-similarity of CDM halos using a larger sample of 15 high-resolution simulations. We investigate deviations from universality in both the spherically averaged density, velocity dispersion, and phase-space density profiles. In the later sections of Chapter 4 we use our findings to motivate an interpretation for the observed scatter in the shapes of spherically averaged density profiles. Additional support for this interpretation is provided by a detailed look at the evolutionary history of the individual halos.

Finally, in Chapter 5, we summarize the main results of the thesis and discuss the implications for future work in related areas.

Chapter 2

The Unorthodox Orbits of Substructure Halos

Abstract

We use a suite of cosmological N-body simulations to study the properties of substructure halos (subhalos) in galaxy-sized cold dark matter halos. We extend prior work on the subject by considering the whole population of subhalos *physically associated* with the main system. These are defined as subhalos that have at some time in the past been within the virial radius of the halo's main progenitor and that have survived as self-bound entities to $z = 0$. We find that this population extends beyond *three times* the virial radius, and contains objects on extreme orbits, including a few with velocities approaching the nominal escape speed from the system. We trace the origin of these unorthodox orbits to the tidal dissociation of bound groups of subhalos, which results in the ejection of some subhalos along tidal streams. Ejected subhalos are primarily low-mass systems, leading to mass-dependent biases in the spatial distribution and kinematics of the population as a whole: the lower the subhalo mass at accretion time, the less centrally concentrated and kinematically hotter their descendant population. The bias is strongest amongst the most massive subhalos, but disappears at the low-mass end: below a certain mass, subhalos behave like test particles in the potential of the main halo. Overall, our findings imply that subhalos identified within the virial radius represent a rather incomplete census of the substructure physically related to a halo: only about *one half* of all associated subhalos are found today within the virial radius of a halo, and many relatively isolated halos may have actually been ejected in the past from more massive systems. These results may help explain the age dependence of the clustering of low-mass halos reported recently by Gao et al, and has further implications for (i) the interpretation of the structural parameters and assembly histories of halos neighboring massive systems; (ii) the existence of low-mass dynamical outliers, such as Leo I and And XII in the Local Group; and (iii) the presence of evidence for evolutionary effects, such as tidal truncation or ram-pressure stripping, well outside the traditional virial boundary of a galaxy system.

2.1 Introduction

In the current paradigm of structure formation, the concordance ΛCDM scenario, the dark matter halos that host galaxy systems are assembled hierarchically, through the merger and accretion of smaller subunits. One relic of this process is the presence of *substructure*, which consists of the self-bound cores of accreted subsystems that have so far escaped full disruption in the tidal field of the main halo (Klypin et al 1999; Moore et al 1999).

Although substructure halos (referred to hereafter as "subhalos", for short) typically make up only a small fraction (5 to 10%) of the total mass of the system, they chart the innermost regions of accreted subsystems, and are thus appealing tracers of the location and kinematics of the *galaxies* that subhalos may have hosted. Substructure is thus a valuable tool for studying galaxies embedded in the potential of a much larger system, such as satellite galaxies orbiting a primary, or individual galaxies orbiting within a group or cluster of galaxies.

This realization has prompted a number of studies over the past few years, both analytical and numerical, aimed at characterizing the main properties of subhalos, such as their mass function, spatial distribution, and kinematics (e.g. Ghigna et al 1998, 1999; Moore et al 1999; Taylor & Babul 2005a,b; Benson 2005; Gao et al 2004; Diemand et al 2007a,b).

Consensus has been slowly but steadily emerging on these issues. For example, the *mass function* of subhalos has been found to be rather steep, $dN/dM \propto M_{\rm sub}^{-1.9}$, implying that the subhalo population is dominated in number by low-mass systems but that most of the substructure mass resides with the few most massive subhalos (Springel et al 2001; Helmi, White & Springel 2002; Gao et al 2004). Confirmation of this comes from the fact that the total fraction of mass in subhalos is rather low (typically below 10%) even in the highest resolution simulations published so far (although see Diemand et al 2007a,b for a differing view).

Subhalos have also been found to be *spatially biased* relative to the smooth

dark matter halo where they are embedded, avoiding in general the innermost regions. Furthermore, the number density profile of the subhalo population also differs markedly from that of galaxies in clusters, and possibly from the radial distribution of luminous satellites around the Milky Way (Kravtsov et al 2004; Willman et al 2004; Madau et al 2008). This precludes identifying directly the population of "surviving" subhalos with galaxies in clusters, and highlights the need for either more sophisticated numerical modeling techniques, or for pairing up the N-body results with semi-analytic modeling in order to trace more faithfully the galaxy population (Springel et al 2001; De Lucia et al 2004; Gao et al 2004; Croton et al 2006).

One intriguing result of all these studies has been the remarkably weak dependence of the properties of substructure on subhalo mass. Gao et al (2004) and Diemand, Moore & Stadel (2004), for example, find that the radial distribution of subhalos is largely independent of their self-bound mass. This is surprising given the strong mass dependence expected for the processes that dictate the evolution of subhalos within the main halo, such as dynamical friction and tidal stripping. Although efficient mixing within the potential of the main halo is a possibility, an alternative explanation has been advanced by Kravtsov, Gnedin & Klypin (2004).

These authors argue that the *present-day* mass of a subhalo may be a poor indicator of the *original* mass of the system, which may have been substantially larger at the time of accretion, and used this idea to motivate how the faintest dwarf companions of the Milky Way were able to build up a sizable stellar mass through several episodes of star formation despite their shallow present-day potential wells. The same idea was also adopted by Libeskind et al (2007) as a possible reason for the peculiar spatial alignment of satellites around the Milky Way (Lynden-Bell 1976, 1982; Kunkel & Demers 1976; Kroupa, Thies & Boily 2005).

We revisit here these issues with the aid of a suite of high-resolution N-body simulations of galaxy-sized halos. We extend prior work by carefully tracking the

orbits of surviving subhalos back in time. This allows us to select a complete set of subhalos *physically associated* with the main halo, rather than only the ones that happen to be within the virial radius at a particular time. As we discuss below, a large fraction of the associated subhalo population are on unorthodox orbits that take them well beyond the virial radius, a result with important implications for studies of satellite galaxies and of halos clustered around massive systems.

The plan of this chapter is as follows. We introduce briefly the numerical simulations in § 2.2 and describe our subhalo detection algorithm and tracking method in § 2.3. Our main results are presented in § 2.4: we begin by exploring the subhalo spatial distribution and kinematics, as well as their dependence on mass, and discuss the consequences of our findings for the subhalo mass function. We end with a brief summary and discussion of possible implications and future work in § 2.5.

2.2 The Numerical Simulations

2.2.1 The Cosmological Model

All simulations reported here adopt the concordance ΛCDM model, with parameters chosen to match the combined analysis of the first-year WMAP data release (Spergel et al 2003) and the 2dF Galaxy Redshift Survey (Colless et al 2001). The chosen cosmological parameters are $\Omega_{\rm m} = \Omega_{\rm dm} + \Omega_{\rm b} = 0.25$, $\Omega_{\rm b} = 0.045$, $h = 0.73$, $\Omega_\Lambda = 0.75$, $n = 1$, and $\sigma_8 = 0.9$. Here Ω denotes the present-day contribution of each component to the matter-energy density of the Universe, expressed in units of the critical density for closure, $\rho_{\rm crit} = 3H^2/8\pi G$; n is the spectral index of the primordial density fluctuations, and σ_8 is the rms linear mass fluctuation in spheres of radius $8\,h^{-1}$ Mpc at $z = 0$. Hubble's "constant" is given by $H(z)$ and parameterized at $z = 0$ by $H(z = 0) = H_0 = 100\,h$ km s^{-1} Mpc^{-1}.

2.2.2 The Runs

Our analysis is based on a suite of 11 high-resolution simulations of the formation of galaxy-sized ΛCDM halos. The simulations target halos of virial mass*, $M_{200} \sim 10^{12}\,h^{-1}\,M_\odot$, and have at $z = 0$ between 2 and 5 million particles within the virial radius, r_{200}. Each halo was selected at random from a list of candidates compiled from a cosmological N-body simulation of a large ($100\,h^{-1}$ Mpc) periodic box and resimulated individually at higher resolution using the technique described in detail by Power et al (2003). We imposed a mild isolation criterion (that no neighbors with mass exceeding $\sim 5\times10^{11}h^{-1}M_\odot$ be found within $1h^{-1}$ Mpc at $z = 0$) in order to exclude systems formed in the periphery of much larger groups or clusters.

The simulations were run with `Gadget2`, a massively-parallel cosmological N-body code (Springel 2005). Particle pairwise interactions were softened using the "optimal" gravitational softening length scale suggested by Power et al (2003); i.e., a spline lengthscale $h_{\rm s} = 1.4\,\epsilon_{\rm G} \approx 4\,r_{200}/\sqrt{N_{200}}$, kept fixed in comoving coordinates. Numerical details of each run are listed in Table 2.1.

2.3 The Analysis

2.3.1 Substructure Finding

We use `SUBFIND` (Springel et al 2001) in order to identify self-bound structures in N-body simulations. `SUBFIND` finds substructure within friends-of-friends (FOF; Davis et al 1985) associations by locating overdense regions within each FOF halo and identifying the bound subset of particles associated with each overdensity. `SUBFIND`

*We define the virial mass of a halo, M_{200}, as that contained within a sphere of mean density $200 \times \rho_{\rm crit}$. The virial mass defines implicitly the virial radius, r_{200}, and virial velocity, $V_{200} = \sqrt{GM_{200}/r_{200}}$, of a halo, respectively. We note that other definitions of the "virial radius" have been used in the literature; the most popular of the alternatives adopts a density contrast (relative to critical) of $\Delta \approx 178\,\Omega_{\rm m}^{0.45} \sim 100$ (for our adopted cosmological parameters, see Eke et al 1996). We shall refer to these alternative choices, where appropriate, with a subscript indicating the value of Δ; i.e., r_{100} is the virial radius obtained assuming $\Delta = 100$.

also works recursively and its output readily identifies "subhalos within subhalos", thus characterizing fully the various levels of the hierarchy of substructure present within a given FOF halo. We retain for our catalogue all SUBFIND subhalos with more than 20 particles.

The main output of SUBFIND is a list of subhalos within each FOF halo, together with their structural properties. For the purposes of this paper, we shall focus on: (i) the subhalo self-bound mass, $M_{\rm sub}$; (ii) the peak of its circular velocity profile (characterized by $r_{\rm max}$ and $V_{\rm max}$); and (iii) the position of the subhalo center, which we identify with the particle with minimum gravitational potential energy. We have run SUBFIND on all 100 snapshots (equally spaced in scale factor, a) of each of our runs, and are therefore able to track in detail the evolution of individual subsystems and their particle members.

2.3.2 Substructure Tracking

Our analysis focuses on all *surviving* subhalos at $z = 0$ and relies heavily on tracking accurately their accretion history. To this aim, we trace each subhalo backwards in time by identifying the central particle at $z = 0$ and searching for the group it belongs to in the immediately preceding snapshot. A new central particle is then selected and the procedure is iterated backwards in time until $z = 9$, the earliest time we consider in the analysis.

This procedure leads in general to a well-defined evolutionary track for each subhalo identified at $z = 0$. When no subhalo is found to contain a subhalo's central particle in the immediately preceding snapshot, the search is continued at earlier times until either a progenitor subhalo is found or $z = 9$ is reached. This is necessary because a subhalo may temporarily disappear from the catalogue, typically at times when it falls below the minimum particle number or else when it is passing close to the center of a more massive system and its density contrast is too low to be recognized by SUBFIND. Our procedure overcomes this difficulty and in most cases

recovers the subhalo at an earlier time. We note that these complications are a fairly common occurrence in the analysis procedure, and we have gone to great lengths to make sure that these instances are properly identified and dealt with when constructing our subhalo catalogue and their accretion histories.

The tracking procedure described above defines a unique trajectory for each subhalo identified at $z = 0$. This trajectory may be used to verify whether a subhalo has, at any time in the past, been accreted within the (evolving) virial radius of the main halo. If this is the case, we record the time it first crosses $r_{200}(z)$ as the "accretion redshift", $z_{\rm acc}$, and label the subhalo as *associated* with the main system. Analogously, we identify a set of *associated dark matter* particles by compiling a list of all particles that were at some time within the virial radius of the main halo but are not attached to any substructure at $z = 0$. On the other hand, halos that have *never* been inside the virial radius of the main halo will be referred to as "field" or "infalling" halos.

Using the subhalo trajectories, we compute and record a few further quantities of interest for each subhalo; namely,

- its "turnaround" distance, $r_{\rm ta}$, defined as the *maximum separation* between a subhalo and the center of the main progenitor before $z = z_{\rm acc}$;
- the structural properties of associated subhalos at $z = 0$ and at accretion time, such as mass and peak circular velocity;
- an apocentric distance, $r_{\rm apo}$, defined as the apocenter of its orbit computed at $z = 0$ using the subhalo's instantaneous kinetic energy and orbital angular momentum, together with the potential of the main halo[†]

Subhalo quantities measured at accretion time will be referred to by using the sub/superscript "acc"; for example, $V_{\rm max}^{\rm acc}$ refers to the peak circular velocity of a

[†]We have checked that our results are insensitive to the triaxial nature of the halo by recomputing $r_{\rm apo}$ using the potential along each of the principal axes of the halo's mass distribution rather than the spherical average. This leads to typical variations of less then $\sim 20\%$ in $r_{\rm apo}$.

subhalo at $z = z_{\rm acc}$. Quantities quoted without superscript are assumed to be measured at $z = 0$ unless otherwise specified; e.g., $V_{\rm max} = V_{\rm max}(z = 0)$.

2.4 Results

The basic properties of our simulated halos at $z = 0$ are presented in Table 2.1. Here, $\epsilon_{\rm G}(= h_{\rm s}/1.4)$ is the `Gadget` gravitational softening input parameter, and M_{200}, r_{200}, and N_{200} are, respectively, the halo virial mass, radius, and number of particles within r_{200}. Table 2.1 also lists the peak of the circular velocity of the main halo, $V_{\rm max}$, and its location, $r_{\rm max}$; the total number of "associated" subhalos; as well as the number of those found within various characteristic radii at $z = 0$.

2.4.1 Subhalos Beyond the Virial Radius

One surprise in Table 2.1 is that the number of "associated" subhalos exceeds by about a factor of ~ 2 the total number of subhalos identified within r_{200}. This result is also illustrated in Fig. 2.1, where we show, at $z = 0$, the distance from the main halo center versus radial velocity for all subhalos identified in our simulations. Distances and velocities have been scaled to the virial quantities of each primary halo. Colored dots are used to denote "associated" subhalos, black symbols for "field" halos. Different colors correspond to different subhalo masses, as measured by the peak circular velocity at accretion time (in units of the present-day primary halo virial velocity, V_{200}): red is used for subhalos with $V_{\rm max}^{\rm acc} \geq 0.72\, V_{200}$, blue for those with $V_{\rm max}^{\rm acc} \leq 0.038\, V_{200}$, green for the rest.

Note that the distribution of associated subhalos extends well past $\sim 3\, r_{200}$; indeed, a few associated subsystems are found at $r \sim 4\, r_{200}$ moving outwards with radial velocity of order $V_r \sim V_{200}$. A careful search shows that there are actually several associated subhalos presently at distances larger than $\sim 5\, r_{200}$.

This result is unexpected in simple formation scenarios, such as the *spherical*

secondary infall model (SSIM, for short). SSIM identifies at any time three distinct regions around a halo: (i) an inner "virialized" region where accreted mass shells have had time to cross their orbital paths; (ii) a surrounding "infall" region, where shells are still on first approach and have not yet crossed; and (iii) a still expanding outer envelope beyond the current turnaround radius (Fillmore & Goldreich 1984; Bertschinger 1985; White et al 1993; Navarro & White 1993).

One of the premises of the secondary infall model is that the energy of a mass shell accreted into the halo is gradually reduced after its first pericentric passage until it reaches equilibrium. During this process, the apocentric distance of the shell is constantly reduced; for example, taking as a guide the SSIM self-similar solutions of Bertschinger (1985), the *second* apocenter of an accreted shell (the first would be its "turnaround" radius) is roughly 90% of its turnaround distance, $r_{\rm ta}$, and the shell gradually settles to equilibrium, approaching a periodic orbit with $r_{\rm apo} \sim 0.8\, r_{\rm ta}$. Thus, according to the SSIM, few, if any, associated subhalos are expected to populate the region outside $\sim 0.8\, r_{\rm ta} \approx 1.6\, r_{200}$. This is clearly at odds with the results shown in Fig. 2.1 and Table 2.1: more than a *quarter* of all associated subhalos are found beyond 1.6 r_{200} at $z = 0$!

2.4.2 The Orbits of Associated Subhalos

The discrepancy between the simulation results and the naive expectation of the SSIM was pointed out by Balogh, Navarro & Morris (2000), and confirmed by subsequent studies (Mamon et al 2004; Gill et al 2005; Diemand et al 2007) but its physical origin has not yet been conclusively pinned down. Associated subhalos found today beyond their turnaround radius have clearly evolved differently from the SSIM prescription, and it is instructive to study the way in which the difference arises.

One possibility is that deviations from spherical symmetry during accretion might be responsible for the outlying associated subhalos. Accretion through the

filamentary structure of the cosmic web surrounding the halo, for example, might result in a number of subhalos on orbits of large impact parameter that simply "graze" the main halo and are therefore not decelerated significantly after their first pericentric approach, as assumed in the secondary infall model. These subhalos would lose little orbital energy, and should presumably be today on orbits with apocentric distances of the order of their original turnaround radii. According to the analytic calculation of Mamon et al (2004), systems on such orbits may reach distances as far as $r_{\rm apo} \sim 2.3\, r_{200}$.

We explore this in Fig. 2.2, where we show the turnaround radius of each associated subhalo versus their apocentric distance estimated at $z = 0$, both normalized to the virial radius of the main halo. Subhalos that have followed the traditional orbits expected from the SSIM should lie to the left of the 1:1 curve in this panel. These, indeed, make up the bulk ($\sim 61\%$) of the associated population.

Note as well that there are a number of subhalos near the 1:1 line, whose orbits have not been decelerated since accretion into the main halo. These are objects that are either on their way to first pericentric passage or, as discussed in the above paragraph, that have somehow evaded significant braking during accretion.

More intriguingly, Fig. 2.2 also shows that there are a significant number of subhalos on decidedly unorthodox orbits, with apocenters exceeding their SSIM theoretical "maximum"; i.e., $r_{\rm apo} > r_{\rm ta}$. Indeed, $\sim 39\%$ of associated subhalos are on such orbits, and about $\sim 3\%$ are on orbits so extreme that their apocenters exceed their original turnaround distance by more than a factor of ~ 2.5 (the latter are highlighted in blue in Fig. 2.2 if, in addition, $r_{\rm apo} > 2\, r_{200}$). The large fraction of systems in such peculiar orbits, where the subhalo has *gained* orbital energy since turnaround, indicates that deviations from spherical symmetry play a minor role in pushing subhalos beyond r_{200}, and suggests that another mechanism is at work.

2.4.3 Subhalo Mass Dependence of Unorthodox Orbits

One clue to the mechanism responsible for pushing some subhalos onto highly energetic orbits is the dependence of the effect on the mass of the subhalo. This is illustrated in the bottom panel of Fig. 2.1, which shows that low-mass subhalos are the ones being preferentially pushed to the outskirts of the halo.

Further clues result from inspecting individually the trajectories of some of the subhalos on extreme orbits. This is shown in the top-left panel of Fig. 2.3, where we show the orbits of a few of the associated subhalos with $r_{\rm apo} > 2.5\, r_{\rm ta}$. Interestingly, all of these subhalos have very low mass at accretion ($V_{\rm max}^{\rm acc} \lesssim 0.08 V_{200}$) and acquire their "boost" in orbital energy during their *first* pericentric passage.

The "wiggles" in their trajectories prior to pericenter betray the fact that they actually belong to a bound system of multiple subhalos accreted as a single unit (Sales et al 2007a, Li & Helmi 2007). This is shown more clearly in the top-right panel of Fig. 2.3, where we show the trajectories of 5 subhalos belonging to one such group. The mass of the group is concentrated in the most massive member (see legends in the figure), which is surrounded (prior to accretion) by 4 bound satellites. The group contributes about 5% of the main halo's mass at accretion time, $a_{\rm acc} = (1+z_{\rm acc})^{-1} \approx 0.65$. The group as a whole turns around at $a_{\rm ta} \approx 0.35$ and accretes on a $(r_{\rm per}{:}r_{\rm apo}) = (1{:}10)$ orbit that reaches $r_{\rm per} \sim 0.25\, r_{200}$ at $a_{\rm per} \sim 0.69$. Adding to this evidence, we find that $\sim 95\%$ of subhalos with $r_{\rm apo} > 2\ r_{200}$ and $r_{\rm apo} > 2.5\ r_{\rm ta}$ were each, prior to accretion, members of an FoF group with multiple subhalos.

During pericentric passage, the group is dissociated by the tidal field of the main halo, and its 5 members are flung onto orbits of widely different energy. The most massive object (single dot-dashed curve in the right panels of Fig. 2.3) follows a "traditional" orbit, rebounding to a second apocenter which is only $\sim 30\%$ of its turnaround distance. The rest evolve differently; the least massive subhalos, in particular, tend to *gain* energy during the disruption of the group and recede to a

second apocenter well beyond the original turnaround. As anticipated by the work of Sales et al (2007b) this is clearly the result of energy re-distribution during the tidal dissociation of the group.

The bottom panels in Fig. 2.3, which show the evolution of the radial velocity of each subhalo, confirm this suggestion. The least massive member of the group is, in this case, the least bound as well, judging from its excursions about the group's center of mass. This subhalo (solid black line in the right panels of Fig. 2.3) happens to be approaching the group's orbital pericenter at about the same time as when the group as a whole approaches the pericenter of its orbit. This coincidence in orbital phase allows the subhalo to draw energy from the interaction; the subhalo is thus propelled onto an orbit that will take it beyond three times its turnaround distance, or $\sim 6\, r_{200}$. Although technically still bound, for all practical purposes this subhalo has been physically ejected from the system and might be easily confused for a system that has evolved in isolation.

There are similarities between this ejection process and the findings of early N-body simulations, which showed that a small but sizable fraction of particles are generally ejected during the collapse of a dynamically cold N-body system (see, e.g., van Albada 1982). The latter occur as small inhomogeneities are amplified by the collapse, allowing for substantial energy re-distribution between particles as the inhomogeneities are erased during the virialization of the system.

In a similar manner, the tidal dissociation of bound groups of subhalos leads to the ejection of some of the group members. The main difference is that, in this case, no major fluctuations in the gravitational potential of the main system occur. Indeed, in the case shown in the right-hand panels of Fig. 2.3 the main subhalo adds only $\sim 5\%$ of its current mass and its potential changes little in the process.

A more intuitive illustration is perhaps provided by Fig. 2.4, where we show, in the r-$V_{\rm rad}$ plane and at $z = 0$, the location of the same accreted group of subhalos. Black dots indicate particles belonging to the main subhalo at the time of accretion.

Large circles mark the location of the center of mass of each surviving subhalo, and the curves delineate their past evolution in the r-$V_{\rm rad}$ plane. The three outermost subhalos track closely a stream of particles formerly belonging to the main subhalo: the "ejected" subhalos are clearly part of the outgoing "tidal tail" stripped from the system during first approach. The origin of subhalos on extreme orbits is thus the same as that of particles at the tip of the outgoing tidal tails during a merger, and it should therefore be a common occurrence during the accretion of any bound group of subhalos.

It is also important to point out that not all low-mass subhalos are affected equally. For example, despite being of comparable mass to the ejected object, one of the low mass members of the group ends up on an orbit almost as tightly bound as the main subhalo (red triple dot-dashed curve in Fig. 2.3). This shows that the orbital fate of a subhalo is mainly determined by its orbital phase within the accreting group at the time of accretion. Depending on this, subhalos may either *lose* or *gain* orbital energy during the interaction.

Low mass halos are, however, the ones preferentially "ejected" or placed on high-energy orbits through this process (see Fig. 2.1 and Fig. 2.6). This is because low-mass members of accreting groups will have orbits of larger amplitude about its center of mass, enhancing the probability of capturing orbital energy when its orbit within the group is in phase with the orbit of the group within the main halo. In turn, this enhances the survival probability of low mass systems by placing them on orbits where they spend extended periods in the periphery of the main halo, outside the region where tidal fields may effectively strip and disrupt them.

The combination of these two effects (energy gain and enhanced survival likelihood) leads to a strong mass dependence on the orbital properties of associated subhalos at $z = 0$. This is illustrated in Fig. 2.5, where we show the ratio of apocenter (estimated at $z = 0$) to turnaround distance as a function of subhalo peak circular velocity. This figure shows clearly that the most massive subhalos are

found today in orbits with apocentric distances much smaller than their turnaround: halos with $V_{\rm max}^{\rm acc} \sim 0.4\,V_{200}$ (which corresponds to roughly $M_{\rm sub}^{\rm acc} \sim 0.1\,M_{200}$) have median apocenters of order half their turnaround distance. On the other hand, the median apocenter of associated subhalos with $V_{\rm max}^{\rm acc} \lesssim 0.1 V_{200}$ is of the order of the turnaround radius.

Note as well that the $V_{\rm max}$ dependence is quite pronounced at the high-mass end but rather weak for low-mass subhalos. This presumably reflects the fact that, once a subhalo is small enough, it behaves more or less like a test particle in the potential of the main system.

Finally, note that the mass dependence is less pronounced when the *present-day* subhalo $V_{\rm max}$ is used. This is because tidal stripping has a more pronounced effect on systems that orbit nearer the center of the main halo. The more massive the subhalo at accretion the closer to the center it is drawn and the more substantial its mass loss, weakening the mass-dependent bias illustrated in Fig. 2.5. We shall see below that the mass dependence becomes even weaker when expressed in terms of the *present-day* subhalo mass.

2.4.4 Subhalo Spatial Distribution

The number density profile of all associated subhalos is shown by the solid (black) curve in Fig. 2.6. The profile may be approximated rather accurately by the same empirical formula introduced by Navarro et al (2004) to describe the mass profile of CDM halos. This profile is characterized by a power-law dependence on radius of the logarithmic slope of the number density, $d\log n/d\log r \propto r^{\alpha}$, which implies a density profile of the form,

$$\ln(n(r)/n_{-2}) = -(2/\alpha)[(r/r_{-2})^{\alpha} - 1]. \qquad (2.1)$$

This density law was first introduced by Einasto (1965), who used it to describe the distribution of old stars within the Milky Way. For convenience, we will refer to it as the Einasto profile. The scaling parameters n_{-2} and r_{-2} may also be expressed in terms of the *central* value of the density, $n_0 = n(r = 0) = e^{2/\alpha}\, n_{-2}$, and of the radius containing *half* of the associated subhalos, $r_{\rm h}$.

We list in Table 2.5 the parameters obtained by fitting eq. 2.1 to the subhalo number density profiles. (Note that the units used for n_0 are arbitrary, but they are consistent, in a relative sense, for the various subhalo populations.) As discussed by Navarro et al (2004), Merritt et al (2005, 2006), and more recently by Gao et al (2007), ΛCDM halo density profiles are well described by $\alpha_{\rm DM}$ in the range $\sim 0.15 - 0.3$. This is in sharp contrast with the much larger values obtained for the subhalo number density profile ($\alpha_{\rm sub} \sim 1.0$; i.e., the 3D radial distribution of subhalos is approximately "exponential"), and quantifies the well-established spatial bias between the subhalo population and the dark matter mass profile of the main halo. The larger values of α characterizing the subhalo spatial distribution imply a large nearly constant density "core" in their profile, in contrast with the "cuspy" density profile of the dark halo, shown as a solid line (without symbols) in Fig. 2.6.

The left panel in Fig. 2.6 shows that the subhalo spatial distribution depends sensitively on subhalo mass, as measured by the peak circular velocity at accretion, $V_{\rm max}^{\rm acc}$ (see also, Nagai & Kravtsov (2005); Faltenbacher & Diemand (2006); Kuhlen et al (2007)). The various colored profiles in this panel correspond to splitting the sample of subhalos into four groups, according to the value of $V_{\rm max}^{\rm acc}$ (normalized to V_{200}, the virial velocity of the main halo at $z = 0$). The concentration increases systematically with $V_{\rm max}^{\rm acc}$; for example, half of the ~ 150 (surviving) subhalos with $V_{\rm max}^{\rm acc} > 0.22\, V_{200}$ are contained within $\sim 0.64\, r_{200}$ at $z = 0$. The corresponding radius for subhalos with $0.04 < V_{\rm max}^{\rm acc}/V_{200} < 0.042$ is $\sim 1.2\, r_{200}$ (see details in Table 2.5).

Interestingly, the mass dependence of the subhalo number density profile essen-

tially disappears when the *present-day* subhalo mass is used to split the sample. This is illustrated in the right-hand panels of Fig. 2.6, which shows that the shape of the density profile of subhalos differing by up to two decades in mass is basically the *same*. This is in agreement with the earlier results of Gao et al (2004) and Diemand et al (2004), but indicates that the apparent mass-independence of the subhalo spatial distribution is *not* the result of efficient mixing within the main halo, but rather a somewhat fortuitous result of the cancellation of the prevailing trend by dynamical friction and tidal stripping.

It is conceivable that numerical artifact may also help to erase the dependence of $n_{\rm sub}(r)$ on present-day subhalo mass. Indeed, `SUBFIND` (like every subhalo finder) will tend to assign masses to subhalos which depend slightly, but systematically, on their location within the main halo. The mass of subhalos near the center is more likely to be underestimated, and some subhalos may, indeed, even be missed altogether if close enough to the central cusp. Splitting the sample by $V_{\rm max}^{\rm acc}$ minimizes such effects and allows for the subhalo mass bias to be properly established.

2.4.5 Velocity Anisotropies

The mass dependence of the subhalo spatial distribution discussed in the previous subsection is significant, but not very large, and thus is less clearly apparent in their kinematics, as shown in Fig. 2.7. The top panels of this figure show the radial velocity dispersion profile, $\sigma_r = \langle v_r^2 \rangle^{1/2}$, computed in spherical shells for the same subsamples discussed in Fig. 2.6. The bottom panels show the anisotropy profile, defined as $\beta \equiv 1 - (\sigma_\theta^2 + \sigma_\phi^2)/2\sigma_r^2$. The mean values of the velocity dispersion for each component are listed in Table 2.5.

The solid lines without symbols in Fig. 2.7 correspond to dark matter particles of the main halo, randomly sampled in order to match the total number of subhalos. As expected, the dark matter velocity distribution is mildly anisotropic, with a radial bias that increases outward and reaches a maximum near the virial radius.

The radial velocity dispersion profile of the subhalo population follows closely that of the dark matter, although as a whole, the subhalo population is kinematically biased relative to the dark halo. The effect, however, is barely detectable; we find $\sigma_r^{\rm sub}/\sigma_r^{\rm DM} \sim 0.98$. Our results thus confirm the earlier conclusions of Ghigna et al (1998), Gao et al (2004), and Diemand et al (2004) about the presence of a slight kinematic bias between subhalos and dark matter.

Unlike the conclusions of Diemand et al, however, we find a significant discrepancy between the anisotropy profiles of the subhalo population and of the dark halo. As shown in the lower panels of Fig. 2.7, subhalos are on orbits less dominated by radial motions than the dark matter and, indeed, have a pronounced *tangential* bias near the center (i.e., for $r \lesssim 0.3\,r_{200}$). With hindsight, this is not entirely unexpected, since subhalos nearer the center are more likely to survive if they are on tangentially-biased orbits that keep them away from the innermost regions of the halo, where tidal effects are strongest.

2.4.6 Subhalo Mass Function

The large number of associated subhalos on high-energy orbits discussed above imply that subhalos within the virial radius are just a fraction of all subhalos physically influenced by the main halo. This is illustrated quantitatively in Fig. 2.8, where we show the cumulative peak circular velocity and mass functions of subhalos identified within r_{200}. The thin red lines in this figure correspond to subhalos identified within r_{200}; black to the full sample of associated subhalos. Thick lines show the average results for the 5 simulated halos considered here. The residuals shown in the small panels are computed relative to the average for the subhalo population within r_{200}, and show that, on average, the total number of associated subhalos exceed those within r_{200} by a factor of ~ 2.

Fig. 2.8 illustrates a number of interesting results. One is that, at the low mass end, the shape of the subhalo mass and velocity function is insensitive to the radius

adopted for selection. Indeed, there is no obvious systematic trend with $V_{\rm max}$ or $M_{\rm sub}$ for $V_{\rm max}/V_{\rm max}^{\rm host} \lesssim 0.2$. Below certain threshold, low mass subhalos behave as "test particles" in the potential of the main halo and their radial distribution becomes independent of mass. This implies that attempts to determine the asymptotic slope of the subhalo mass function are unlikely to be compromised by selecting for analysis only halos within the virial radius, as is traditionally done.

On the other hand, the subhalo mass function *shape* is substantially affected at the opposite end; although about half of all associated subhalos with $V_{\rm max} \lesssim 0.15\,V_{\rm max}^{\rm host}$ are missing from within r_{200}, this fraction declines to one quarter for $V_{\rm max} \sim 0.28\,V_{\rm max}^{\rm host}$, and to zero for $V_{\rm max} > 0.31\,V_{\rm max}^{\rm host}$. As a result, in that mass range, the mass function of subhalos identified within r_{200} is shallower than that of associated systems. This should have interesting consequences for semianalytic modeling of the luminosity function in galaxy groups and clusters, which traditionally assume that all accreted subhalos remain within the virial radius of the main system.

2.5 Summary and Discussion

We have used a suite of cosmological N-body simulations to study the orbital properties of substructure halos (subhalos) in galaxy-sized cold dark matter halos. We extend prior work on the subject by considering the whole population of *associated* subhalos, defined as those that (i) survive as self-bound entities to $z = 0$, and (ii) have at some time in the past been within the virial radius of the halo's main progenitor. Our main findings may be summarized as follows.

- The population of *associated* subhalos extends well beyond three times the virial radius, r_{200}, and contains a number of objects on extreme orbits, including a few with velocities approaching the nominal escape speed from the system. These are typically the low-mass members of accreted groups which

are propelled onto high energy orbits during the tidal dissociation of the group in the potential of the main halo.

- The net result of this effect is to push low-mass subhalos to the periphery of the system, creating a well-defined mass-dependent bias in the spatial distribution of associated subhalos. For example, only about $\sim 32\%$ of subhalos which, at accretion time, had peak circular velocities of order 3% of the present-day virial velocity ($V_{\rm max}^{\rm acc} \sim 0.03\,V_{200}$), are found today within r_{200}. This fraction climbs to $\sim 63\%$ and to $\sim 71\%$ for subhalos with $V_{\rm max}^{\rm acc} \sim 0.1\,V_{200}$ and $\sim 0.3\,V_{200}$, respectively.

- The strength of the bias is much weaker when expressed in terms of the subhalo *present-day* mass, due to the increased effect of dynamical friction and tidal stripping on the most massive subsystems.

- The spatial distribution, kinematics, and velocity anisotropy of the subhalo population are distinct from the properties of the dark matter. Subhalos are less centrally concentrated, have a mild velocity bias, and are, near the center, on more tangential orbits than the dark matter.

The unorthodox orbits of substructure halos that result from the complex history of accretion in hierarchical formation scenarios have a number of interesting implications for theoretical and observational studies of substructure and of the general halo population.

One implication is that subhalos identified within the virial radius represent a rather incomplete census of the substructures physically related to (and affected by) a massive halo. This affects, for example, the interpretation of galaxy properties in the periphery of galaxy clusters, and confirms earlier suggestions that evolutionary effects normally associated with passage through the innermost regions of a massive halo, such as tidal truncation or ram-pressure stripping, should be detectable well

outside the traditional virial boundaries of a group or cluster (Balogh, Navarro & Norris 2000).

Furthermore, associated subhalos pushed well outside the virial radius of their main halo might be erroneously identified as separate, isolated structures in studies that do not follow in detail the orbital trajectories of each system. This effect would be most prevalent at low masses, and it is likely to have a significant effect on the internal properties of halos in the vicinity of massive systems. We expect, for example, halos in the periphery of groups/clusters to show evidence of truncation and stripping, such as higher concentrations and/or sharp cutoffs in their outer mass profiles.

The same effect may also introduce a substantial environmental dependence in the formation-time dependence of halo clustering reported in recent studies (Gao et al 2005; Zhu et al 2006; Jing et al 2007; see also Diemand et al 2007b). In particular, at fixed mass, early collapsing halos might be more clustered because they are physically associated with a more massive system from which they were expelled.

A proposal along these lines has recently been advanced by Wang, Mo & Jing (2007) (see also Hahn et al 2008), who argue that such environmental effects might be fully responsible for the age-dependence of halo clustering. Our physical interpretation, however, differs in detail from theirs. Whereas Wang et al argue for the suppression of mass accretion onto "old" halos by "heating by large-scale tidal fields" as responsible for their enhanced clustering, our results suggest that the real culprit is the orbital energy gain associated with the tidal dissociation of bound groups of subhalos, which allows "old" low-mass halos to evade merging and to survive in the vicinity of massive systems until the present.

A further implication of our results concern the spatial bias of the most massive substructures discussed in § 2.4.4. If, for example, luminous substructures in the Local Group trace the most massive associated subhalos at the time of accretion,

they may actually be significantly more concentrated and kinematically biased relative to the dark matter, a result that ought to be taken into account when using satellite dynamics to place constraints on the mass of the halos of the Milky Way and M31.

Finally, as already pointed out by Sales et al (2007a,b), gravitational interactions during accretion may also be responsible for the presence of dynamical outliers in the Local Group, such as Leo I and And XII. Further work is needed to assess whether the exceptional orbits of such systems could indeed have originated in the tidal dissociation of groups recently accreted into the Local Group. Since the latest proper motion studies of the Magellanic Clouds seem to suggest that the Clouds are on their first pericentric passage (Kallivayalil et al 2006; Piatek et al 2007), this is a possibility to consider seriously when trying to puzzle out the significance of the motion of the satellites of the Local Group.

Halo	ϵ_G $[h^{-1}\mathrm{kpc}]$	M_{200} $[h^{-1}M_\odot]$	$M_{\rm DM}^{\rm assoc}$ $[h^{-1}M_\odot]$	r_{200} $[h^{-1}$ kpc]	$V_{\rm max}$ [km s^{-1}]	$r_{\rm max}$ $[h^{-1}\mathrm{kpc}]$	N_{200}	$M_{\rm sub}^{\rm assoc}$ $[h^{-1}M_\odot]$	$N_{\rm sub}$ [assoc]	$N_{\rm sub}$ $(r < r_{200})$	$N_{\rm sub}$ $(r < r_{100})$	$N_{\rm sub}$ $(r < r_{50})$	$N_{\rm sub}$ $r_{\rm apo} > 2.5r_{\rm ta}$
9-1-53	0.250	9.22×10^{11}	12.1×10^{11}	158.3	184.8	36.0	3.24e6	0.90×10^{11}	904	513	742	1017	3
9-12-46	0.181	7.03×10^{11}	10.5×10^{11}	144.9	159.9	34.9	4.82e6	0.62×10^{11}	2020	865	1314	1828	20
9-13-74	0.220	8.61×10^{11}	12.2×10^{11}	154.7	175.9	32.0	4.18e6	1.14×10^{11}	1683	831	1232	1645	24
9-14-39	0.186	12.6×10^{11}	17.9×10^{11}	175.7	203.5	37.8	3.30e6	1.31×10^{11}	1416	594	1050	1581	6
9-14-56	0.275	8.50×10^{11}	12.2×10^{11}	154.1	178.6	33.7	2.61e6	0.99×10^{11}	1160	469	646	930	16
9-14-49	0.186	9.17×10^{11}	13.0×10^{11}	158.0	171.3	47.6	6.00e6	1.18×10^{11}	2374	1222	1956	2553	53
9-4-70	0.171	8.85×10^{11}	13.3×10^{11}	156.1	174.8	64.0	6.10e6	0.98×10^{11}	1852	712	1115	1720	95
C02-400	0.250	14.4×10^{11}	19.2×10^{11}	183.7	209.2	21.3	4.79e6	1.45×10^{11}	1877	943	1458	2071	17
9-23-84	0.279	5.64×10^{11}	7.5×10^{11}	134.4	151.9	59.2	2.04e6	0.42×10^{11}	483	238	364	515	10
9-2-48	0.321	13.1×10^{11}	18.3×10^{11}	177.8	200.2	47.0	2.48e6	1.44×10^{11}	1340	628	942	1338	6
9-2-20	0.757	48.6×10^{11}	57.3×10^{11}	275.5	285.6	196.3	1.08e6	5.55×10^{11}	425	286	407	546	16

Table 2.1: Structural properties of galaxy halos used in this study: ϵ_G is the `Gadget` gravitational softening; virial mass, M_{200}; mass of all associated dark matter, $M_{\rm DM}^{\rm assoc}$; virial radius, r_{200}; location and magnitude of the halo peak circular velocity, $r_{\rm max}$ and $V_{\rm max}$; N_{200} is the total number of particles within r_{200}; total mass in associated subhalos $M_{\rm sub}^{\rm assoc}$; and $N_{\rm sub}(< r)$ is the total number of subhalos identified within various characteristic radii.

Sample	$N_{\rm sub}$ [5 sims]	n_0 [arb.units]	r_{-2} [r_{200}]	$r_{\rm h}$ [r_{200}]	α	$\langle\beta\rangle$	$\langle\sigma_r\rangle$ [V_{200}]
Assoc. dark matter		5422	0.l12	0.558	0.159	0.270	0.734
Assoc. subhalos	7183	964.8	0.67	1.05	0.806	0.070	0.743
$(X = V_{\rm max}^{\rm acc}/V_{200})$							
X > 0.220	150	122. 3	0.28	0.64	0.416	0.179	0.689
$0.060 < X < 0.22$	4782	654.	0.56	0.83	0.716	0.109	0.724
$0.042 < X < 0.060$	4782	268.	0.84	1.06	0.96	0.034	0.725
$0.040 < X < 0.042$	750	25.7	0.98	1.18	1.05	-0.051	0.727
$(Y = \log_{10} M_{\rm sub}/M_{200})$							
$Y > -3.0$	150	8.61	0.89	1.00	1.282	0.079	0.718
$-4.5 < Y < -3.0$	4387	317.1	0.73	0.99	0.832	0.023	0.741
$-4.9 < Y < -4.5$	4387	326.4	0.74	1.04	0.864	0.052	0.745
$-5.0 < Y < -4.9$	750	41.5	0.83	1.10	0.954	0.014	0.743

Table 2.2: The first column lists the criteria used in selecting various subhalo samples; $N_{\rm sub}$ is the total number of subhalos in each sample; n_0 is hte central value for the subhalo number density profiles; r_{-2}, $r_{\rm h}$, and α are the characteristic radii and Einasto parameter for the number density profiles of the various subhalo samples; $\langle\beta\rangle$ and $\langle\sigma_r\rangle$ are, respectively, the average anisotropy and radial velocity dispersion for various subhalo samples.

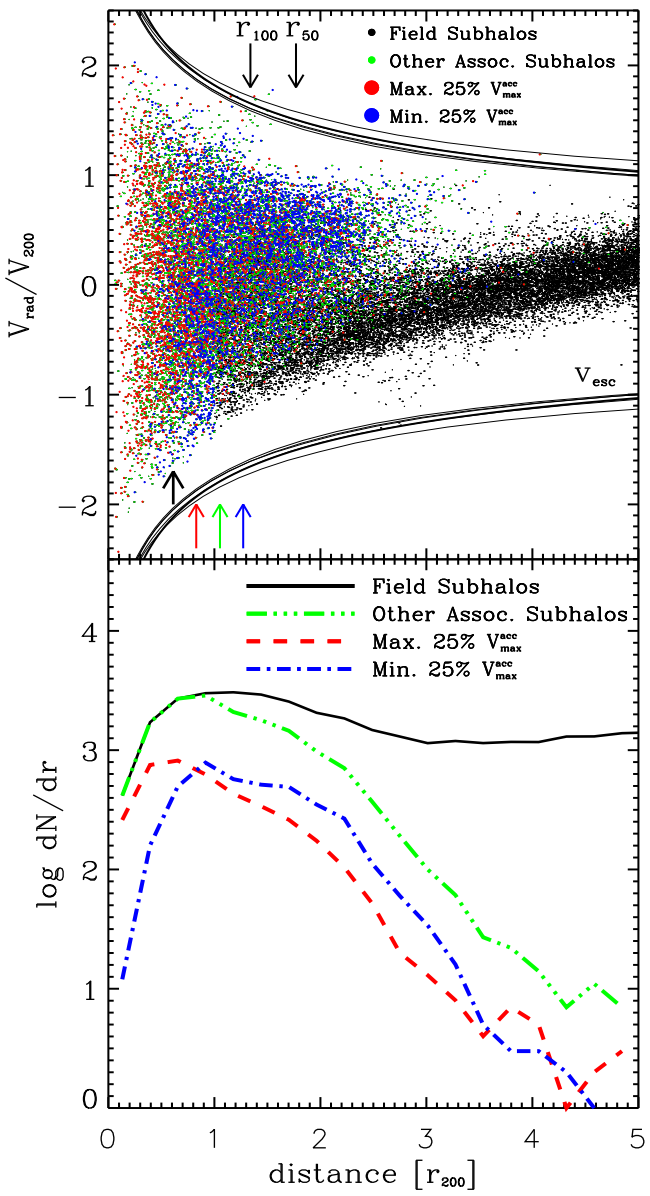

Figure 2.1: *Upper panel:* Radial velocity versus distance to the main halo center for all subhalos within $5 \times r_{200}$ in our simulations. Velocities and distances are normalized to the virial velocity, V_{200}, and virial radius, r_{200}, of each host. All "associated" halos are shown in color, subhalos on first infall are shown in black. Different colors are used according to the peak circular velocity of the subhalo at the time of accretion. Blue denotes the quartile with smallest $V_{\rm max}^{\rm acc}$, red those with largest $V_{\rm max}^{\rm acc}$. Green denotes the rest of the associated subhalo population. Upward vertical arrows of matching color indicate the half-number radius for the various subhalo populations. A shorter black arrow marks the half-number radius for "associated" dark matter particles. We find that 65% of subhalos in the range $r_{200} < r < 2\,r_{200}$ are actually "associated" and have thus already been within the host virial radius in the past. Roughly one third of subhalos between $2\,r_{200} < r < 3\,r_{200}$ are also physically "associated" with the main halo. The upper and lower bounding curves denote the escape velocity for each of the five simulated halos. *Lower panel:* Radial distribution of subhalos. Color key is the same as in the upper panel.

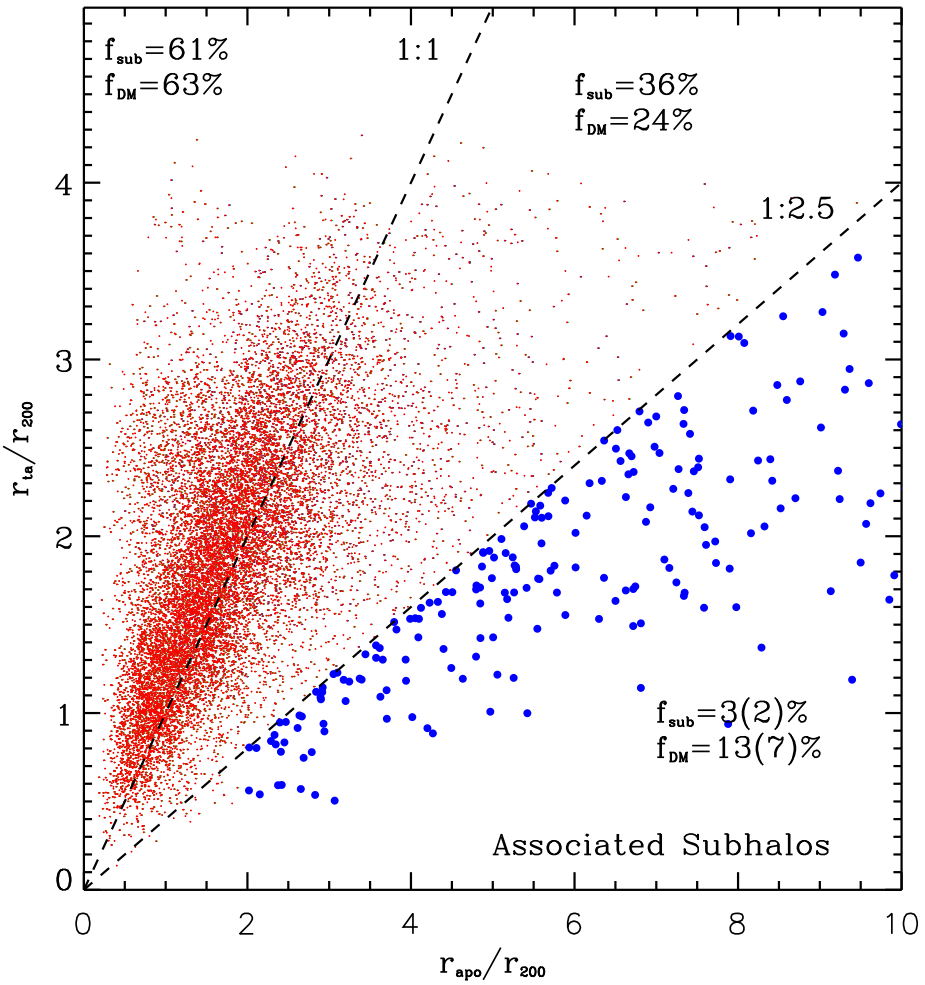

Figure 2.2: Turnaround radius versus apocentric distance at $z = 0$ for all *associated* subhalos in our simulations. The turnaround distance is the maximum distance from the main halo before accretion. Subhalos on "traditional" orbits are expected to have $r_{\rm apo} < r_{\rm ta}$ and, thus, to be to the left of the 1:1 curve in this plot. Subhalos near the 1:1 line have $r_{\rm apo} \approx r_{\rm ta}$ and are therefore on orbits which have not been decelerated substantially since turnaround. Subhalos with $r_{\rm apo} > r_{\rm ta}$ are on unorthodox orbits and they have *gained* orbital energy during or after accretion. The blue symbols in the panel highlight subhalos on extreme orbits, that will take them more than ~ 2.5 times farther than their turnaround radius. The fraction of associated subhalos and associated dark matter particles in each region of the plot is given in the legends.

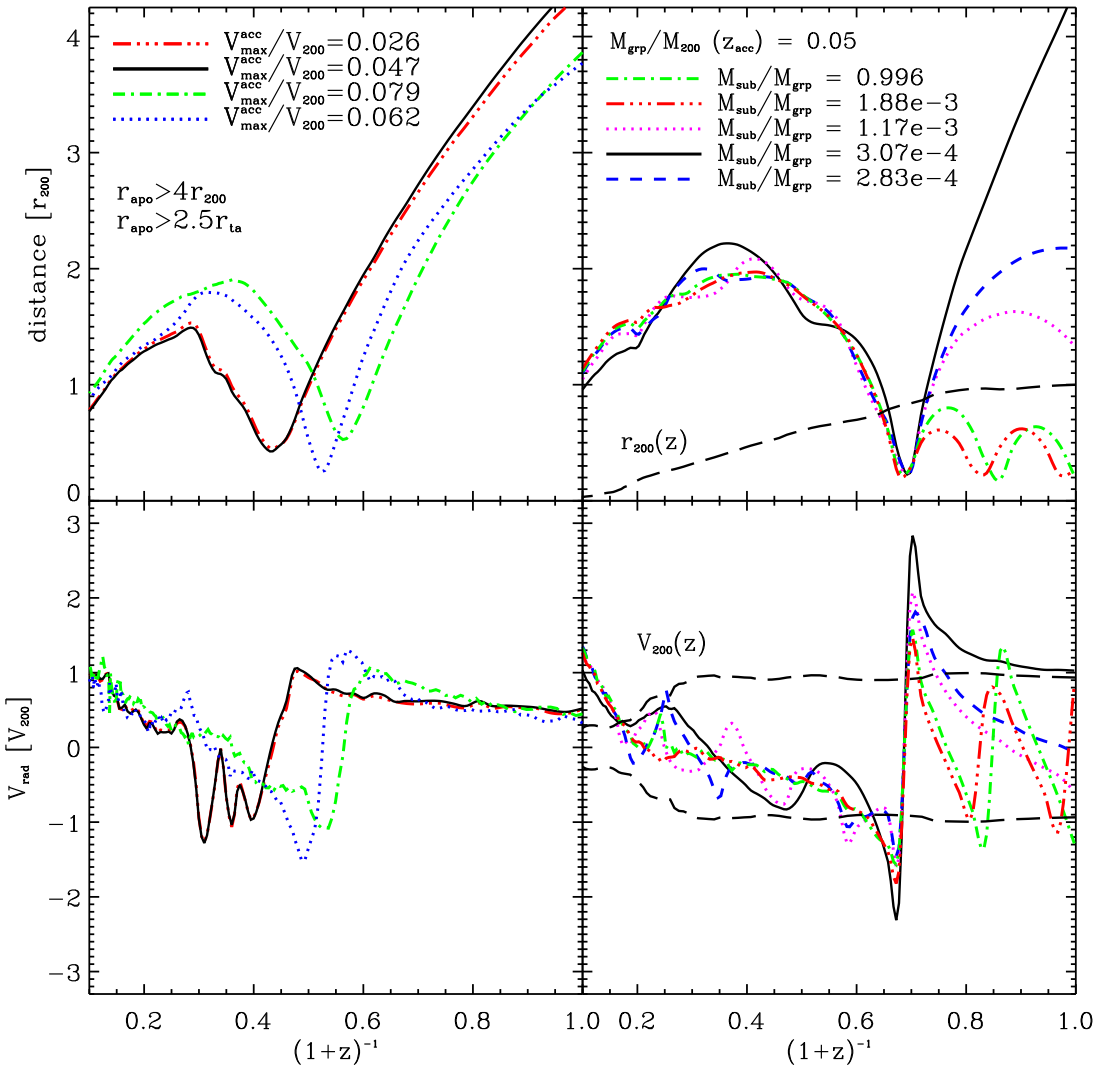

Figure 2.3: Orbital trajectories of selected subhalos. Upper panels show the distance to the center of the main progenitor as a function of expansion factor. The top-left panel shows the trajectories of 4 subhalos on "extreme" orbits (blue points in Fig. 2.2). Note that all of these systems gain energy during their first pericentric approach to the main halo. The top-right panel illustrates that interactions occurring during the tidal dissociation of bound groups of subhalos are responsible for propelling some satellites onto extreme orbits. At pericentric approach, the tidal field of the main halo breaks apart the group, and redistributes each member onto orbits of varying energy. The most affected are, on average, the least massive members of the group, some of which are pushed onto orbits with extremely large apocenters. The dashed curve shows the growth of the virial radius of the most massive progenitor of the main halo. Bottom panels show the radial velocity of the subhalos shown in the upper panels.

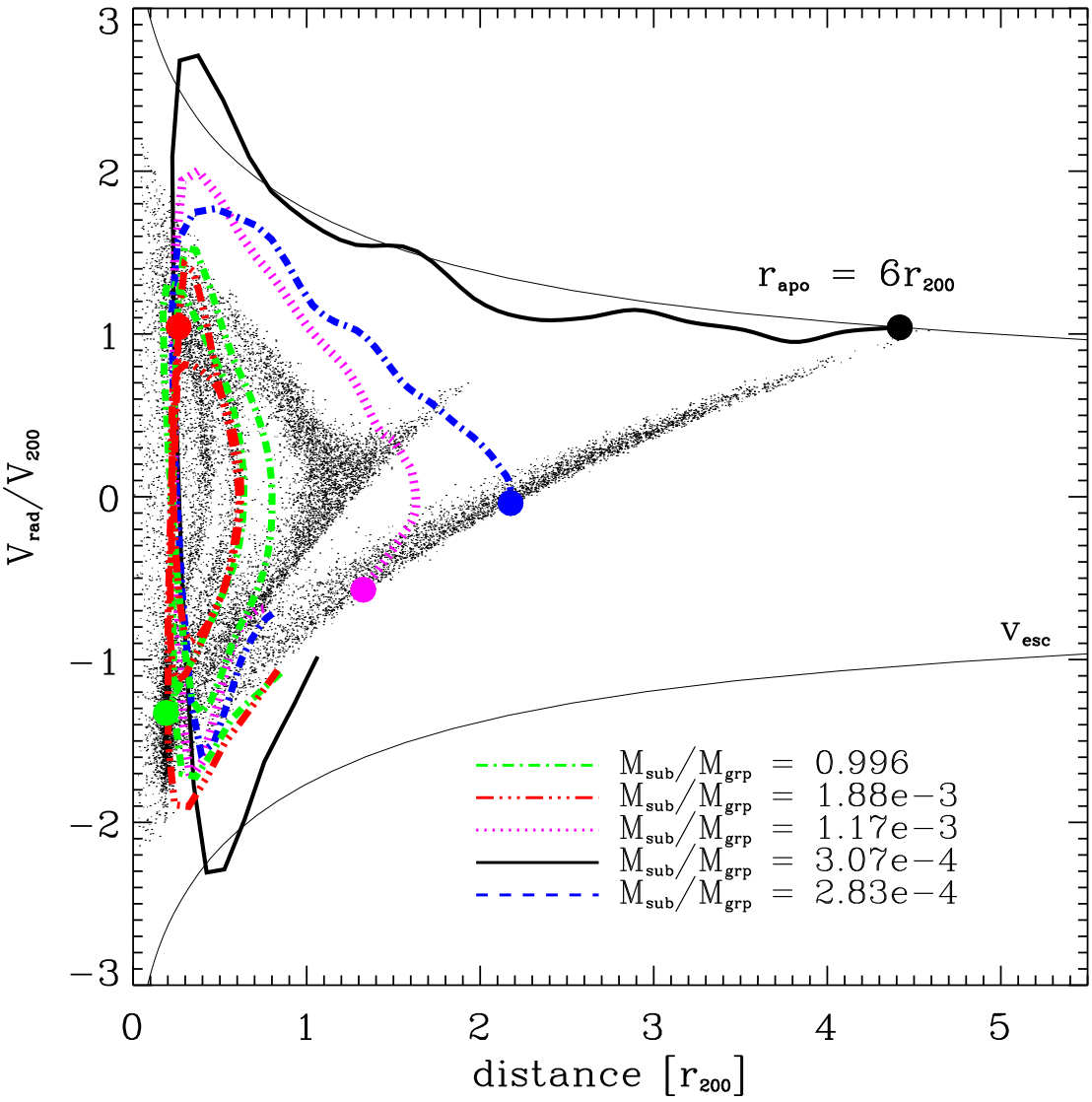

Figure 2.4: Black dots show the position, at $z = 0$, of particles belonging, at accretion time, to the most massive subhalo of the group shown in the right-hand panels of Fig. 2.3. Large circles show the position of the center of mass of the other (surviving) subhalos in the group. Curves show the evolution the center of mass of each of subgroup since accretion. Note how the surviving subhalos align themselves with tidal streams stripped from the main subhalo during the disruption process. The "ejection" of subhalos is thus due to the same mechanism that leads to the formation of outgoing tidal tails in a merger event and should occur naturally during the tidal dissociation of any bound group of subhalos.

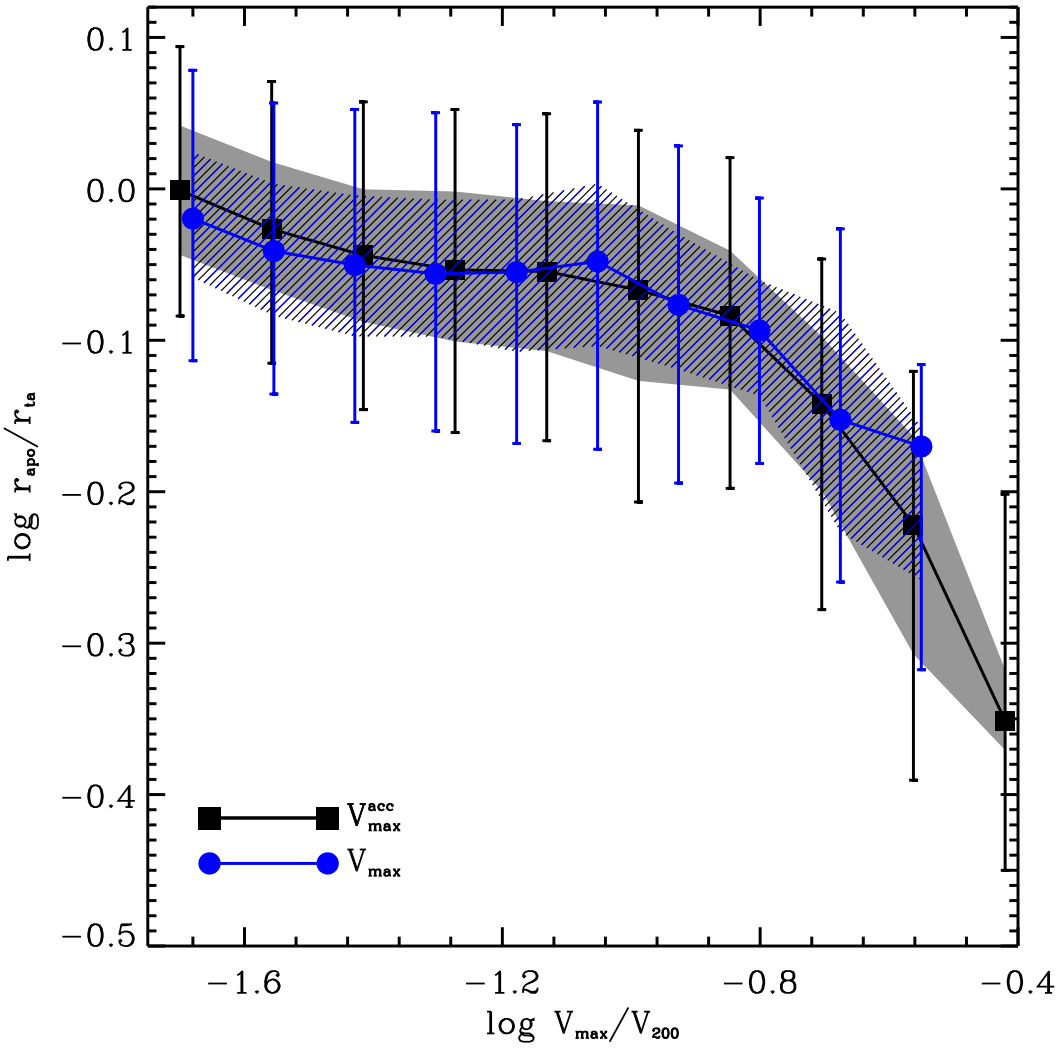

Figure 2.5: The ratio of apocentric radius (estimated at $z = 0$) to turnaround distance as a function of the peak circular velocity, $V_{\rm max}$, of a subhalo. Two estimates of $V_{\rm max}$ are used for each subhalo, one measured at accretion time and another at $z = 0$. Symbols correspond to the median of the distribution, shaded areas encompass 25% of the distribution around the median, and the extremes of the error bars correspond to the 25th and 75th centiles. Note that only fairly massive associated subhalos are today on orbits substantially more bound than when they turned around. The median apocentric radius of low-mass subhalos is of order of the virial radius, indicating that about *half* of all associated subhalos spend a substantial fraction of their orbital period outside r_{200}. Note that the effect depends only weakly on $V_{\rm max}$ below a certain threshold; this presumably indicates that, below a certain mass limit, subhalos behave like test particles in the potential of the main halo.

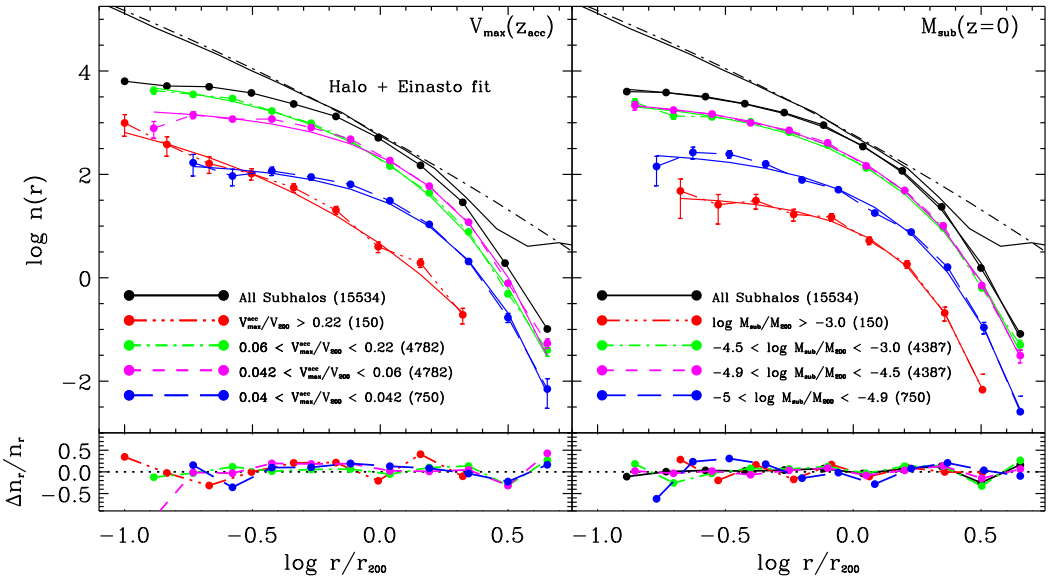

Figure 2.6: Number density profile of associated subhalos, after stacking the results of all 11 simulations in our series. The black solid symbols show the result for all subhalos, the other symbols correspond to various subsamples obtained after splitting by either $V^{\rm acc}_{\rm max}$ (left panel) or by subhalo mass at $z = 0$ (right-hand panel). Details on the velocity and mass range for each subsample are given in the legend. Solid lines through each curve correspond to the best fits obtained with eq. 2.1. The parameters of each fit are listed in Table 2.5. Lines without symbols show the dark matter density profile. Note that the spatial distribution of subhalos depends sensitively on subhalo mass when measured by $V^{\rm acc}_{\rm max}$, but that, in agreement with prior work, the mass bias essentially disappears when adopting $M_{\rm sub}$ to split the sample. See text for further discussion.

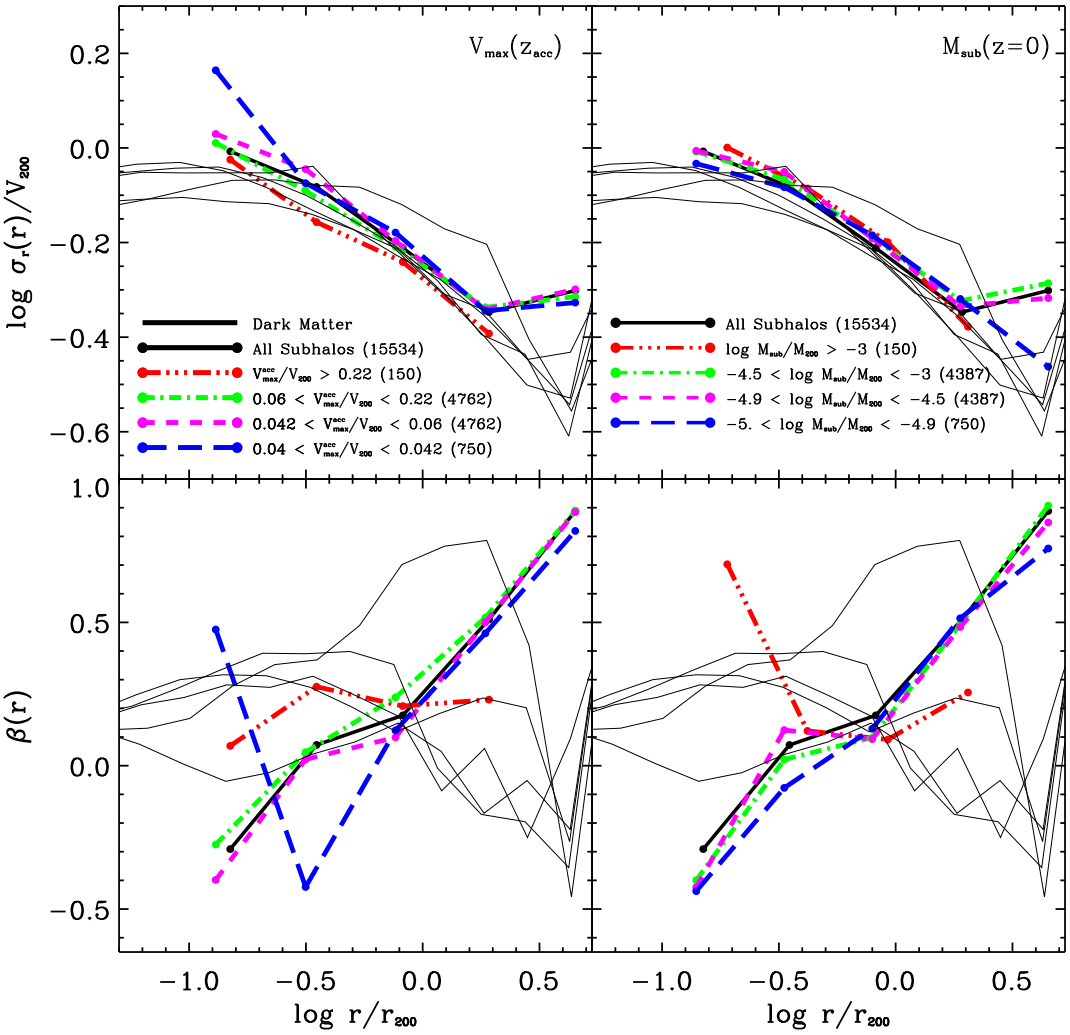

Figure 2.7: Radial velocity dispersion and anisotropy profiles for dark matter (thin black lines) and associated subhalos (thick colored lines). Symbols are described in the legend and are the same as in Fig. 2.6. Note that the mass-dependent bias shown in Fig. 2.6 is also reflected in the subhalo kinematics: low mass subhalos tend to have higher velocity dispersions than their high-mass counterparts. This bias is clearer when measuring subhalo mass by the peak circular velocity at accretion time, $V^{\rm acc}_{\rm max}$, rather than by the self-bound mass at $z = 0$, $M_{\rm sub}$. Note as well that subhalos tend to be on orbits less radially biased than the dark matter, especially near the center. This is presumably because subhalos on tangentially-biased orbits avoid the innermost regions of the main halo, thus enhancing their survival probability.

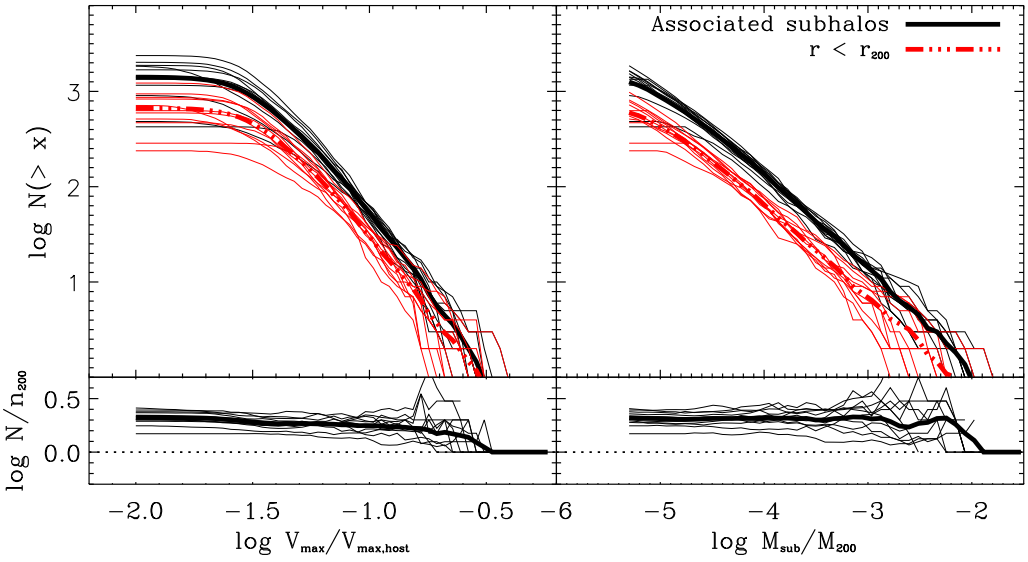

Figure 2.8: Associated subhalo mass ($M_{\rm sub}$) and peak circular velocity ($V_{\rm max}$) cumulative distributions (both quantities measured at $z = 0$). Black lines correspond to all associated subhalos; red lines to subhalos identified within r_{200}. Thick lines in each panel denote the average of our 5 simulations. Note that the number of associated subhalos exceeds by about a factor of ~ 2 the number of subhalos found within r_{200}. The residuals are computed relative to the subhalo population within the virial radius.

Chapter 3

The Structure and Substructure of Galactic Dark Halos

Abstract

We study the structure and substructure of galaxy-sized ΛCDM halos using a suite of cosmological N-body simulations of unprecedented numerical resolution. The *Aquarius project* follows the non-linear evolution of a sample of six ultra-highly resolved galaxy-sized dark matter halos. In our highest resolution simulation more than 1.5 *billion* particles compose the main halo at $z = 0$; all other runs have between about 100 and 200 million particles within the $z = 0$ virial radius. In this chapter we quantify the basic statistics of the substructure population and the structure of the main halo in each of the six Aquarius simulations.

In our highest resolution run we resolve $\sim 3 \times 10^5$ gravitationally bound substructures within the virial radius of the main halo. This abundance of substructure is significantly higher than reported for the *Via Lactea* simulations; halo-to-halo scatter and subtle differences in cosmological parameters are unlikely to account for this fact. We find that the spectrum of substructure masses associated with the main halo follow a well-defined power-law with $dN/dM \propto M^{-1.9}$ over nearly 5 decades in subhalo mass. Extrapolating this behavior to the thermal free-streaming limit of the dark matter particle suggests that the mass distribution of the main halo is dominated by a smooth component, contrary to previous claims that all of the mass may actually be bound into small clumps. In agreement with the work presented in chapter 2 we find that the spatial distribution and kinematics of the subhalo population is largely independent of (present day) subhalo mass.

Our analysis of the structure of the main halo confirms prior claims that the spherically averaged mass profile deviates slightly but systematically from the form proposed by Navarro, Frenk & White. The logarithmic slope of the density profile becomes increasingly shallow towards the halo center with no sign of converging to an asymptotic power-law; a radial dependence accurately described by the Einasto profile. For our highest resolution run converged results are achieved down to scales of $\sim 100h^{-1}$pc, at which point the *maximum* asymptotic slope is $\gamma_{\rm max} \approx -0.89$, convincingly ruling out recent claims for cusps as steep as $r^{-1.2}$. The phase-space density profile is remarkably well described by a

single "universal" power-law consistent with Bertschinger's secondary infall solution; i.e. $\rho/\sigma^3 \propto r^{-1.875}$. The "radial" phase-space density profile, $\rho/\sigma_{\rm r}^3$, also shows a power-law radial dependence, albeit with a systematically steeper slope than -1.875, in agreement with previous work.

3.1 Introduction

The concordance ΛCDM model is widely successful at explaining a variety of astrophysical and cosmological observations. In the context of this model the dark matter was created in the early universe with a negligible thermal velocity, perturbed by a scale-free distribution of Gaussian density fluctuations. When coupled with inflation, this results in a fluctuation power spectrum which favors small scales. As a result, small scale fluctuations are the first to collapse in ΛCDM, and their merger and accretion contributes to the formation of progressively larger structures; a manifestly hierarchical scenario.

In recent decades steady progress has been made in our understanding of the clustering properties of dark matter on galactic scales, driven largely by the development of numerical techniques and computational hardware designed to simulate the process. There is now a general consensus that the hierarchical assembly of CDM halos leads to a number of common features: 1) *cuspy* mass profiles that are nearly "universal" (i.e. independent of mass and background cosmology up to a simple scaling); 2) local entropy profiles that follow power-laws with radius; 3) strong triaxial shapes; and 4) abundant substructure content with a power-law spectrum of masses.

Despite this general agreement, a number of contentious issues still plague the CDM model and its predictions regarding the structure of dark matter halos. One, for example, concerns the abundance, structure, and spatial distribution of substructure halos. In the past, the debate was largely focused on the discrepancy between the abundance of substructure predicted by N-body simulations to reside

within the halo of a galaxy and the paucity of such substructure in observations of the Local Group. Though a genuine absence of such small scale structure in the Galactic halo would signal a failure of the CDM model, it is not yet clear whether these systems simply failed to form stars. More recently, however, the debate has shifted to the discovery and interpretation of possible signals from dark matter annihilation in the gamma-ray sky (e.g. Bergström et al 1998), and the role that substructure plays in such observations.

The discovery that dark matter halos are *cuspy* has also generated a lot of controversy in the community. Whereas some recent studies claim a well-defined central slope of $\rho \propto r^{-1.2}$ (Diemand et al 2004, 2005, 2008), other studies of comparable resolution find no compelling evidence for an asymptotic power-law behavior (e.g. Power et al 2003; Navarro et al 2004, 2008). No doubt some of this debate surrounds the issue of which fitting formula describes the mass profile of dark matter halos best; either the broken power-law advocated by NFW and M99, or profiles with power-law logarithmic slopes, such as the Einasto profile (N04; Merrit et al 2005).

A related issue concerns the self-similarity, or "universality", of the density profile of ΛCDM halos. If, indeed, the structure of dark matter halos can be accurately modeled by a simple two-parameter fitting formula, such as the NFW profile, or its modification, the Moore profile, then dark matter halos can always be appropriately rescaled as to be indistinguishable. Recently, however, Gao et al (2008) and Hayashi & White (2008) have argued that the *shape* of the density profile (characterized by its logarithmic slope) depends systematically on halo mass, indicating that *three* parameters may be required to describe the mass profile of ΛCDM halos accurately. If this were true it would imply that the halo mass profile is *not* strictly universal: no simple rescaling of a cluster, for example, could match in detail the mass profile of a dwarf.

Arriving at a robust prediction for the inner structure of dark matter halos

requires simulations of very high resolution, as well as a detailed understanding of the limitations imposed by the choice of numerical parameters and resolution effects. These questions were addressed in Power et al (2003), where it was shown that, for suitable choices of all other numerical parameters, the main factor affecting the inner mass profile is the number of particles used in the simulation. Empirically, the innermost radius beyond which numerical convergence is achieved corresponds roughly to the location at which the relaxation time equals the age of the universe.

The relaxation time at a given radius scales as $t_{\rm relax} \sim N/\ln N \times t_{\rm orb}$, where $N(r)$ is the number of particles within r and $t_{\rm orb}$ is the local orbital timescale. Since the latter decreases steadily towards the halo center, improving the radial range of numerical convergence requires dramatic increases in the total number of particles. Combining this with the observed halo-to-halo scatter in the CDM density profiles (see, e.g. Fig. 4.1) suggests that progress on these issues will require a concerted effort in which *several* different halos are resimulated at varying resolution, in order to overcome cosmic variance and directly assess numerical convergence.

Much of the work carried out during my PhD thesis focused on aspects of the *Aquarius* project, a programme designed by the Virgo Consortium to shed light on the problems related to dark matter on galactic scales. The Aquarius simulation suite follows the non-linear evolution of six galaxy sized dark matter halos in unprecedented detail, using the highest resolution simulations currently feasible. One of these halos has been simulated five times, increasing gradually the mass resolution by about a factor of roughly 2000 from the lowest to highest resolution run. In this run, the main halo has roughly 1.5 *billion* particles within the virial radius of the main halo at $z = 0$, making it the highest resolution simulation of its kind ever carried out.

Each of the Aquarius simulations were performed with the new parallel TreePM code `Gadget3` , written by Volker Springel specifically for the Aquarius project. `Gadget3` is a massively parallel N-body code with better efficiency and scalability,

and a higher basic speed than its predecessor, `Gadget2`. The simulations for the Aquarius project were carried out at the Leibniz Computing Center in Garching, Germany; at the Computing Center for the Max-Planck-Society in Garching, and on "STELLA", the super-computer dedicated to the LOFAR experiment at the University of Gronigen. More details about the numerical techniques, including a more thorough discussion of `Gadget3` and the initial conditions for the Aquarius simulations, are presented in Springel et al (2008a,b), and Navarro et al (2008), to which we refer the interested reader.

In this Chapter, we present the basic $z = 0$ properties of the suite of Aquarius halos. This includes the substructure mass and peak circular velocity distributions, the radial distribution and kinematics of the substructure halos, as well as the structure of each main halo and its inner cusp.

3.2 The Aquarius Halos

The Aquarius simulation suite includes six galaxy-sized dark matter halos selectively resimulated with varying resolution. Images of each are provided in Fig.s 3.1 and 3.2. The halos were identified in the same parent simulation as the suite of halos presented in Chapter 2, as well as those which will be presented in Chapter 4. Each halo was selected at random from a list of objects with $M_{\rm halo} \approx 10^{12} M_{\odot}$ that also passed a mild isolation criterion (no objects larger than half its mass within 1 Mpc/h), in order to exclude systems formed on the outskirts of larger structures. Semi-analytic models applied to the parent volume predict each halo to host a late-type galaxy, making their selection appropriate for modeling Milky Way-like halos.

Each simulation is started from initial conditions at $z = 127$ and follows the formation of the halo through to $z = 0$ in a 100 h^{-1}Mpc periodic box. The choice of cosmological parameters match all other simulations presented in this thesis,

namely: $\Omega_m = 1 - \Omega_\Lambda = 0.25$, $\sigma_8 = 0.9$, $n = 1$, and $H_0 = 73$ km s^{-1}Mpc^{-1}. These choices are consistent with current cosmological constraints derived from WMAP1 and WMAP5 data (Spergel et al 2003; Komatsu et al 2008), and are the same parameters adopted for the Millennium simulation (Springel et al 2005).

Each halo is then selectively resimulated at varying resolution, with power input with the same amplitudes and phases as the parent simulation on all resolved spatial scales. In doing so, the 100 Mpc/h simulation cube is divided into two regions; the high resolution region is defined by a Lagrangian volume surrounding the halo of interest, and is embedded in a low resolution region in which the particle masses increase roughly linearly with distance from the halo. Growing modes are achieved by displacing particle positions from a glass-like load (White, 1996) and assigning peculiar velocities according to the Zel'dovich approximation. Care is taken to ensure that the region surrounding the high resolution particles retains sufficient structure to generate the appropriate tidal field and to avoid contamination of the halo by background particles.

The basic characteristics of the Aquarius halos are presented in Table 3.1. Here we provide, for each halo, a name, the high resolution particle mass and gravitational softening, as well as various characteristic radii and the total mass and particle number that they enclose. We define the virial mass, M_{200}, of a halo as that contained within the radius, r_{200}, at which the mean overdensity first drops below $200 \times \rho_{\rm crit}$. Other structural parameters include the location of the peak in the circular velocity curve, specified by $V_{\rm max}$ and $r_{\rm max}$, as well as $\sigma_{\rm host}$, the 1D rms velocity of the host halo, and $\sigma_{\rm max}$, the maximum velocity dispersion computed in spherical shells. The softening parameters are specified by the "optimal" softening criteria of Power et al (2003).

In order to facilitate comparison with previous work, in particular that of Diemand et al (2007, 2008), we will often quote numbers relative to r_{50}, defined as the radius enclosing a mean *matter* density of 200 $\Omega_{\rm m}$ $\rho_{\rm crit}$, or in our case $50 \times \rho_{\rm crit}$.

We adopt a naming scheme in which the six Aquarius halos are associated with the tags "Aq-A" through "Aq-F". The resolution level is encoded in an additional suffix: "1" represents the highest resolution run, and "5" the lowest. In our highest resolution simulation, Aq-A-1, the main halo has ∼1.5 billion particles within r_{50} at $z = 0$. All other halos were simulated up to level "2", and have between 160 and 224 million particles within r_{50} at the present day.

3.3 The Distribution and Abundance of Galactic Subhalos

In this section we present the basic statistics, spatial distribution, and kinematics of subhalos in the Aquarius simulations. We identify substructure halos in the same manner as in Chapter 2, by isolating sets of particles that are bound to locally overdense regions of a given friends-of-friends halo. A catalogue of subhalos and some basic statistics, including position, velocity, total bound mass, spin, and various structural parameters, are stored for each subhalo in the simulation. The analysis presented in this section is limited to subhalos containing at least 20 particles.

3.3.1 Subhalo Abundances

A basic statistic describing the substructure content of a dark matter halo is its substructure mass function, which quantifies the abundance of subhalos as a function of their mass. In Fig. 3.3 we plot the differential subhalo abundance for halo Aq-A at different resolutions. The large variance at the high mass end ($M_{\rm sub} \gtrsim 10^8 h^{-1}$Mpc) is expected since the number of massive subhalos is low. Below this mass, however, there is a smooth spectrum of substructure masses which follows very closely a power-law with slope -1.9 (shown as a dashed line in Fig. 3.3). In the lower panel of Fig. 3.3 we plot $M_{\rm sub} dN/d\log M_{\rm sub}$, which corresponds to the total mass

in substructure in a given logarithmic mass interval. Plotting the mass function in this way compresses the vertical scale and allows the overall shape and convergence of the mass spectrum to be studied in more detail. It is clear from this panel that the mass functions converge remarkably well when limited to subhalos with > 100 particles (shown here as vertical dotted lines), for which softening effects are neglidgible.

The fact that the subhalo mass function is shallower than -2 is subtle but has important implications for the total substructure content of the halo. In the latter case the total mass in subhalos below mass m_0 diverges logarithmically; low-mass subhalos contribute as much to the substructure mass fraction as high mass ones. If this were indeed the case it may indicate that galactic dark matter halos possess no smooth component at all, but are instead completely composed of bound substructure (as suggested by, for example, Calcáneo-Roldàn & Moore 2000). However, in either case the total mass fraction in subhalos depends on the thermal free-streaming limit of the CDM particle, which lies between $m_{fs} = 10^{-6} M_{\odot}$ and $10^{-12} M_{\odot}$, depending on the adopted particle physics model (Hofmann et al 2001; Green et al 2004)

In Fig. 3.4 we show the cumulative substructure mass in subhalos with $M > M_{\rm sub}$ for halo Aq-A. This is shown separately for all subhalos identified within r_{200}, and for those within r_{50}. The thin dashed line corresponds to an extrapolation of the power-law mass function, $dN/dM \propto M^{-1.9}$, whereas the triple-dot-dashed line shows $dN/dM \propto M^{-2}$. It is clear from Fig. 3.4 that, provided our extrapolation is valid, galactic dark matter halos should posses a substantial smooth component, even in the logarithmically divergent case. In the latter, the total mass fraction in bound substructures should not exceed $\sim 50\%$ within r_{50}, even in the extreme case where $m_{fs} = 10^{-12} M_{\odot}$. Also interesting is that the substructure mass fraction within r_{200} is substantially lower than that within r_{50} (see also Table 3.2), suggesting that the smooth component dominates the inner regions of the halo. Indeed, we

find a conservative upper limit to the substructure mass fraction for our Aq-A halo to be $\sim 11\%$ within r_{200}. This number rises to $\sim 18\%$ when considering the volume within r_{50}.

However, limited conclusions can be drawn from the analysis of a single object. In Fig. 3.5 we show the differential mass function for all subhalos identified within r_{50} in each level 2 run. In order to make a more meaningful comparison between halos, we have normalized the substructure masses by M_{50}, the total mass contained within r_{50}. The dashed line in each panel is identical to that in Fig. 3.3, and corresponds to $dN/dM \propto M^{-1.9}$. Again we see a significant scatter at the high mass end, where there is a large halo-to-halo variation in substructure content. At the low mass end, however, the abundance of substructure per logarithmic mass interval shows very little scatter and each is described remarkably well by a single power-law.

Using these results one can estimate the theoretical *maximum* substructure mass fraction within r_{50}. Based on the finding that the substructure mass function is accurately described by

$$\frac{dN}{dM} = A_0 \left(\frac{M}{M_0} \right)^{\nu}, \tag{3.1}$$

it follows that the total mass in *unresolved* substructure below the resolution limit is

$$M_{\rm tot}(< r_{\rm res}) = \int_{m_{\rm lim}}^{m_{\rm res}} M \frac{dN}{dM} dM = \frac{A_0}{\nu + 2} \left(\frac{m_{\rm res}^{\nu+2} - m_{\rm lim}^{\nu+2}}{M_0^{\nu}} \right). \tag{3.2}$$

A conservative upper limit to the total substructure mass within r_{50} is obtained for the limiting case $m_{\rm lim} \to 0$. We find that $A_0 = 8.21 \times 10^7 / M_{50}$, $M_0 = 10^{-5} M_{50}$ and $\nu = -1.9$ provides a accurate description of the mass function in each of our simulations, and choose $m_{\rm lim}$ to correspond to their respective (20 particle) resolution limits.

With this choice of parameters, eq. 3.2 predicts a *total* substructure mass fraction of 17.4% for Aq-A-1, our highest resolution run, and for the level 2 runs: 17.0% (Aq-B), 13.0% (Aq-C), 18.3 % (Aq-D), 19% (Aq-E), and 21.5% (Aq-F). This suggests

that, on average, the total mass in *unresolved* substructure in the level 2 runs is roughly 9.4% of M_{50}, which is lower than the average substructure mass *already* resolved by the simulations. In Table 3.2 we summarize the substructure content of the Aquarius halos in more detail.

Assigning a bound mass to a set of substructure halos is, to some extent, a subjective process. One has to choose a particular identification algorithm, an unbinding procedure, or an operational definition of the subhalos outer edge. Because of this, different substructure detection algorithms may produce systematic differences in the bound mass estimates for subhalos, depending on the adopted procedure. It may therefore be advantageous to characterize the abundance of subhalos in terms of some other characteristic quantity, in order to avoid uncertainties associated with the mass assignment. One possibility is to use the structural parameter $V_{\rm max}$ as a proxy for subhalo mass; $r(V_{\rm max})$ typically lies well within the boundary of a subhalo and should therefore be less sensitive to definitions of its outer edge, or total bound mass.

The cumulative distributions of $V_{\rm max}$ are shown in Fig. 3.6 for each of our level 2 simulations. We normalize the peak circular velocities by the circular speed at r_{50}: $V_{50} = \sqrt{GM_{50}/r_{50}}$. With this scaling, which essentially the same as normalizing by the halo mass, M_{50}, there is remarkably little halo-to-halo scatter between our different runs*. To connect with previous work we also show the cumulative distributions of $V_{\rm max}$ reported by Diemand et al (2007, 2008) for the Via Lactea simulations, which have been appropriately rescaled to V_{50}. This conclusively shows that the Aquarius simulations have significantly *more* substructure (at a given mass) than both of the Via Lactea I *and* II simulations. This is particularly evident at the low mass end, where small number statistics are negligible; the Aquarius simulations show very little scatter in this regime, as was apparent from the subhalo mass functions already.

*The abundance curves in Fig. 3.6 have $N(> V_{\rm max}) \propto (V_{\rm max}/V_{50})^{-3}$, and since $V_{50}^3 \propto M_{50}$, normalizing subhalo peak circular speeds by V_{50}, is equivalent to normalizing by halo mass.

It has been suggested by Madau et al (2008), and by Diemand et al (2008), that differences of this magnitude may be within the halo-to-halo scatter, or may be induced by slight differences in the adopted cosmological parameters. In particular, the Via Lactea simulations use $\sigma_8 = 0.74$, about 18% lower than the value adopted for the Aquarius project. Lowering the normalization of the power spectrum effectively decreases the amplitude of matter fluctuations at a given redshift. Gravitational collapse of initial overdensities is thus delayed slightly in models with lower σ_8. This results in *more* substructure at a given mass, simply because the number of low-mass subhalos surviving until $z = 0$ is larger. Thus, we find it unlikely that subtle differences in the adopted cosmology contribute to the different subhalo abundances patterns observed for Via Lactea and the Aquarius runs. Furthermore, the very small dispersion in the Aquarius mass functions at the low-mass end indicate that halo-to-halo scatter is unlikely to be the origin of this discrepancy.

The possibility that halo-to-halo scatter in the substructure mass function may explain the observed paucity of dwarf satellites, as suggested by Ishiyama et al (2007), is not supported by our simulations.

3.3.2 Spatial Distribution

In § 2.4.4 and § 2.4.5 of Chapter 2 we examined the spatial distribution and kinematics of subhalos found in a lower resolution series of N-body simulations. We here revisit these issues with the aid of the Aquarius simulations, which offer much higher resolution and a larger dynamic range than those presented previously.

We begin by showing the radial distribution of subhalos in the Aq-A series as a function of subhalo mass. The number density profiles (top panel) have been normalized by the mean number density (of each sub-sample) within r_{50}. In agreement with previous work (e.g. Gao et al (2004); Diemand, Moore & Stadel (2004)), we find that the number density of subhalos increases towards the halo center, but does so much more slowly than the dark matter (shown as a thin black line in the upper

panel of Fig. 3.7). As a consequence, the majority of subhalos at any mass scale are found in the outer regions of the halo, beyond about 100 kpc. We show this explicitly in the lower panel of Fig. 3.7, where we plot the fraction of all subhalos (of a given mass) that lie at a given radius at $z = 0$. Clearly the vast majority of subhalos are at rather large distances, independent of their mass.

Perhaps more important is the apparent lack of any trend in the spatial distribution with subhalo mass. We have already discussed this in Chapter 2, but reproduce the result here with much higher resolution and a larger dynamic range than previously. If one is willing to extrapolate this behavior to arbitrarily small masses it would follow that the the dark matter mass distribution would be completely dominated by a smooth halo component in the inner regions (see also Fig. 3.4). This illuminates a discrepancy between our simulation results and the speculations of Calcáneo-Roldàn & Moore (2000) and Moore et al (2004), that the total halo mass may actually be bound into small clumps.

We show this behavior explicitly in Fig 3.8, where we plot the total cumulative substructure mass fraction as a function of radius for our Aq-A series (left), and for all level 2 runs (right). All of our highest resolution simulations show the same characteristic behavior in which the substructure mass fraction increases with distance from the halo center. An important point to make about all of this is that the substructure mass fraction within the solar circle (marked with $R_{\odot} = 8$ kpc in each panel) is expected to be small, typically less than $\sim 0.1\%$ for the Aquarius runs. This would suggest that the dark matter in the Milky Way Galaxy through which the earth moves is expected to be very smooth, with very little contribution from bound substructure.

3.3.3 Kinematics

In Fig. 3.9 we show the velocity dispersion and anisotropy profiles for subhalos in the Aq-A-1 simulation, selected by mass. The spatial bias of subhalos with respect

to the dark matter is also present in their kinematics: subhalos closer to the halo center are dynamically hotter than the dark matter. The velocity anisotropy profiles of substructure halos also show a clear bias; at any given radius the substructure velocity distribution is more isotropic than the dark matter, but the overall shape of the anisotropy profiles appears to be similar.

The results presented here are consistent with those discussed in Chapter 2, although with the increased dynamic range in the Aq-A-1 simulation a new trend is also evident. In agreement with the results presented in Chapter 2, we find that the *radial* velocity dispersion profiles of subhalos are independent of the present-day subhalo mass. However, there appears to be a slight but systematic mass dependence to the anisotropy in the subhalo's velocity distribution; at any given radius more massive subhalos tend to follow more isotropic orbits than those of lower mass. This is also evident in the tangential velocity dispersion profiles, which show that more massive systems have a more pronounced tangential velocity dispersion than lower mass systems. This mass dependence, which is more pronounced at smaller radii, is a simple indication that more massive systems are more likely to survive as bound objects if they have a slight tangential bias, which keeps them away from the more distructive inner regions of the halo.

3.4 The Structure of Galactic Dark Matter Halos: Diversity and Similarity in Halo Structure

In this section we study the structure of galaxy-sized dark matter halos using the Aquarius simulations. Our analysis focuses on the spherically averaged density, velocity dispersion, velocity anisotropy, and pseudo-phase-space density profiles each halo primary computed, as averages, in spherical shells.

3.4.1 Mass Profiles

Numerical Convergence

In order to accurately and robustly quantify the inner mass profile of the Aquarius halos we begin with a brief discussion of numerical convergence. Fig. 3.10 shows the spherically averaged mass profiles of the five Aq-A simulations run at different resolutions; the left panels show the local density profiles (weighted by a factor of r^2 in order to highlight departures); the right panels show the circular velocity profiles. We use lines of different color to distinguish runs of different resolution and mark the radius corresponding to the Plummer-equivalent gravitational softening with vertical arrows.

The results presented in Fig. 3.10 show the striking numerical convergence achieved by our series of resimulations. As mention by Springel et al (2008) and Navarro et al (2008), this exemplifies the care that has been taken in building our initial conditions, and the precision of the cosmological code `Gadget3`. Indeed, the overlap of the profiles in the outer regions, where substructure induces significant noise, suggests that our simulations faithfully reproduce not only the properties of the main halo, but also the location and mass of its dominant substructures.

Numerical convergence of the mass profile of simulated CDM halos has been discussed in detail by Power et al (2003). These authors show that systematic deviations in the mass profile, measured with respect to a "converged" result, depend predominantly on the total number of particles (provided that appropriate choices for the other numerical parameters are made), and scales roughly with the relaxation time. The empirical results of P03 indicate that deviations $\lesssim 10\%$ in the circular velocity profile are achieved at radii where the local relaxation time is longer than the age of the universe. Expressed in unit of the circular orbital

timescale at the virial radius, the relaxation time may be written

$$\kappa = \frac{N}{8 \ln N} \frac{r/V}{r_{200}/V_{200}} = \frac{\sqrt{200}N}{8 \ln N} \left(\frac{\bar{\rho}(r)}{\rho_{\rm crit}} \right)^{-1/2}, \tag{3.3}$$

where $N(r)$ is the enclosed particle number, $\bar{\rho}(r)$ is the mean density interior to r, and $\rho_{\rm crit}$ is the critical density. The results of Power et al (2003, hereafter P03) indicate convergence to $\lesssim 10\%$ for regions where $\kappa \geq 1$, and they use this to define an empirical "convergence radius", which they call $r_{\rm conv}$. Stricter convergence in the mass profile requires regions with larger values of κ, and in what follows we shall use a superscript on $r_{\rm conv}$ to denote the value of κ used in each case. For example, $r_{\rm conv}^{(1)}$ corresponds to $\kappa = 1$, as in the original work of P03.

The radial range over which convergence is achieved is, of course, different for runs of different resolution. However, when deviations in the V_c profiles are expressed in terms of κ the trends are similar. This is shown in the top panel of Fig. 3.11, where the deviation of each circular velocity profile from that of Aq-A-1 is plotted as a function of κ. As anticipated by P03, deviations in V_c are of order 10% for $\kappa \approx 1$. Resolving the mass profile to better than $\sim 2.5\%$ requires $\kappa \approx 7$, as indicated by the vertical dashed line to the right in Fig. 3.11.

These results can be used to estimate various convergence radii for our highest resolution run, Aq-A-1. For example, we expect convergence in the V_c profiles to be $\sim 10\%$ for $r > r_{\rm conv}^{(1)} \approx 112\ h^{-1}$pc; better than $\sim 2.5\%$ convergence is acheived for $r > r_{\rm conv}^{(7)} \approx 253\ h^{-1}$pc. Convergence radii corresponding to these values of κ for all other Aquarius halos are presented in Table 3.1.

The profiles shown in Fig. 3.10 use thick lines for $r_{\rm conv}^{(7)} \leq r \leq 3\ r_{200}$; thin lines show regions where $r_{\rm conv}^{(1)} < r < r_{\rm conv}^{(7)}$. It is clear from the lower-right panel that $r_{\rm conv}^{(1)}$ indeed corresponds to the radius where deviations in V_c are roughly 10%. The bottom-left panel shows that convergence in the spherically averaged density profile is always better, since this is a local quantity rather than a cumulative one. Defining

convergence of the mass profile in this way is thus a conservative approach.

Fitting Formulae

We have mentioned previously that an unsettled debate regarding the true asymptotic behavior of the ΛCDM halo mass profile plagues the analysis and interpretation of many observational data sets. No doubt much of the debate surrounds which choice of analytic fitting formulae most accurately describes the mass profile of simulated dark matter halos. We revisit these issues here using the Aquarius simulation suite and test the quality of several of the most commonly used fitting formulae in the literature. The top-left panel of Fig. 3.10 shows, however, one difficulty; the presence of substructure and unrelaxed tidal debris in the outer regions of the halo cause transient bumps and wiggles to appear in the outer halo mass profile. We circumvent this uncertainty by focusing our analysis on the halo inner regions, namely the region interior to r_{-2}, the radius at which $d\ln\rho/d\ln r = -2$, the isothermal value. This is a well defined radial scale and marks the location of the peak in the $\rho\ r^2$ profiles. Inside r_{-2} the density profiles are smooth and there is very little noise caused by the presence of substructure.

In practice, we determine r_{-2} by fitting a power-law to the smooth inner regions of the $d\ln\rho/d\ln r$ profile and identifying where this fit intersects -2. The value of r_{-2} determined in this way, as well and the associated characteristic densities, $\rho_{-2} = \rho(r_{-2})$, are given in Table 3.3. In the following discussion we will always concern ourselves with the region interior to r_{-2}, unless explicitly stated otherwise.

We consider three of the most commonly discussed parametrizations for the CDM halo mass profile. These include: 1) the NFW profile, given by

$$\rho(r) = \rho_s(r/r_s)^{-1}(1 + r/r_s)^{-2}, \tag{3.4}$$

2) the modification of the NFW formula proposed by Moore et al (1999) (hereafter

referred to as the M99 profile),

$$\rho(r) = \rho_M (r/r_M)^{-1.5}(1 + r/r_M)^{-1.5}, \tag{3.5}$$

and, finally, 3) the Einasto profile

$$\ln(\rho(r)/\rho_{-2}) = -(2/\alpha)[(r/r_{-2})^{\alpha} - 1]. \tag{3.6}$$

Because the characteristic radii of each of these formulae differ we choose to reparametrize them in terms of r_{-2} and $\rho_{-2} \equiv \rho(r_{-2})$, which implicitly defines the "peak" in the ρr^2 profiles in the left-hand panel of Fig. 3.10. Note that for the NFW profile $r_s = r_{-2}$ and $\rho_s = 4\rho_{-2}$, while for the M99 profile, $r_{-2} = 2^{-2/3} r_M$ and $\rho_{-2} = (4/3)\rho_M$.

In the top panel of Fig. 3.10 the triple-dot-dashed line shows the best-fit Einasto profile (with $\alpha = 0.170$), computed by minimizing the residuals with respect to the Aq-A-1 density profile over $r^{(1)}_{\rm conv} \leq r \leq r_{-2}$. The residuals relative to this fit are shown in the lower panels and make it clear that the Einasto profile reproduces the inner mass profile of halo Aq-A extremely well.

The left panel of Fig. 3.12 compares the density profiles of all six level 2 Aquarius halos, after rescaling all radii to r_{-2} and densities to ρ_{-2}. The right panels show the circular velocity profiles, scaled analogously to match the characteristic peak of the profile, identified by $V_{\rm max}$ and $r_{\rm max}$. In these normalized units the NFW and M99 profiles are fixed and appear to provide a rather poor description of the mass profile over-all. NFW systematically underestimates the density profile interior to r_{-2} whereas the M99 profile appears to overestimate the density. We do note, however, that each profile has been normalized by the value of r_{-2} determined by fitting the $\rho(r)$ profile to eq. 3.6, and do not necessarily correspond to the r_{-2} values that minimize the residuals between each individual profile and the adopted fitting formula. Allowing r_{-2} and ρ_{-2} to vary during the fitting process does result in improved fits. We show this in the lower-panels of Fig. 3.12, where the residuals

are plotted relative to the "best-fit" of each profile. Though the *shape* of the NFW profile appears to mismatch the numerical data the discrepancy is not huge; typically residuals are less than $\sim 25\%$ for $r < r_{-2}$. Despite this, the Einasto profile clearly does better than NFW, with the latter showing a slight but significant systematic trend in the residuals. Furthermore, systematic deviations from the best-fit NFW profile appear the largest at the innermost resolved point, suggesting that extrapolating eq. 3.4 to arbitrarily small radii is likely to incur substantial error. The M99 profile is clearly at odds with the numerical results, and is confidently ruled out by our simulations.

The scaling of the profiles in Fig. 3.12 was chosen explicitly in order to illustrate one of our main findings: namely, the mass profiles of the six Aquarius halos *are not strictly self-similar*. The differences are subtle, but robust, and no simple scaling of the profiles can be chosen to match one halo to another. The most striking example is given by halo Aq-E, which deviates from, for example, halo Aq-D by more than a factor of 2 in density at $\sim$3% of r_{-2}. The same differences are also evident in the circular velocity profiles indicating that differences in the mass profiles are genuine and are *not* simply a result of inaccurate rescaling of the density profiles[†].

Table 3.3 lists, for each halo, the best-fit Einasto shape parameter α. The small residuals in the lower panels of Fig. 3.12 shows that the Einasto profile captures the shape of the CDM halo mass profiles rather accurately, with residuals showing no systematic trend down to the innermost resolved point. The values of α listed in Table 3.3 range from 0.122 (for Aq-E) to 0.177 (for Aq-D). We have checked explicitly that these differences in α are not cause by transient departures from equilibrium, or numerical resolution. We shall return to these issues again in Chapter 4.

[†]We have tested that departures from self-similarity are *not* the result of the presence of substructure: the full profiles shown in Fig. 3.12 are virtually indistinguishable from those computed without substructure, with systematic departures evident only in the outer regions of the halos.

The Cusp Structure

We saw in the previous subsection that the density profile proposed by M99 provides a rather inaccurate description of the structure of our simulated halos. The origin of this discrepancy appears to be related to the steeply divergent $r^{-1.5}$ cusp predicted by eq. 3.5. Indeed, all of our Aq-A runs (including the lowest resolution run, Aq-A-5) have *measured* slopes in the inner regions that are *already shallower* than -1.5. This is shown in Fig. 3.13, where the thick portions of each curve correspond to $r \geq r_{\rm conv}^{(7)}$ and the innermost point reaches $r_{\rm conv}^{(1)}$.

We note that in our highest resolution run, Aq-A-1, the *measured* slope at $r_{\rm conv}^{(7)}$ is ~ -1 and continues to shallow down to the innermost resolved point, $r_{\rm conv}^{(1)}$ (see Fig. 3.13). This indicates that, at least in this case, we resolve regions of the halo where the slope becomes shallower than the asymptotic value proposed by NFW. Fig. 3.14 shows the radial dependence of the logarithmic slope for all of our level 2 runs. The measured slopes at $r_{\rm conv}^{(7)}$ are *all* substantially shallower than -1.5 and continue to shallow towards the halo center, reaching $d\ln\rho/d\ln r \simeq -1$ at $r_{\rm conv}^{(1)}$.

The logarithmic slope profiles shown in Fig.'s 3.13 and 3.14 also lack any sign of approaching power-law behavior near the halo center. The radial behavior of $d\ln\rho/d\ln r$ appears to be accurately described by a power-law, such as that provided by the Einasto profile. Recent claims suggesting the existence of cusps as steep as $r^{-1.2}$ (Diemand et al 2004; 2005; 2008) are thus strongly disfavored by our data.

Asymptotic Inner Slope

The results presented above indicate that convergence to a well-defined central power-law is inconsistent with the numerical data over the resolved radial range. However, this does not preclude the existence of a shallow power-law cusp in the central regions of dark matter halos. The maximum allowed value for such a central cusp can be constrained directly from the data and, in fact, depends only on the enclosed mass and local density at a given radius. It is straightforward to show that

the maximum allowable power-law slope is given by

$$\gamma_{\rm max} = 3\left(1 - \frac{\rho(r)}{\bar{\rho}(r)}\right), \tag{3.7}$$

where $\rho(r)$ and $\bar{\rho}(r)$ are the local and mean density at radius r respectively. Evaluating eq. 3.7 at the innermost resolved point provides an important constraint on the mass profile interior to the convergence radius.

In Fig. 3.15 we show the radial dependence of this quantity for our Aq-A series. As before, thick lines correspond to $r > r^{(7)}_{\rm conv}$ and thin lines to $r > r^{(1)}_{\rm conv}$. Down to $\approx r^{(7)}_{\rm conv}$ the maximum asymptotic slope profiles converge remarkably well. For our highest resolution run (Aq-A-1) we robustly rule out an asymptotic slope steeper than $\sim r^{0.9\pm0.1}$. Fig. 3.16 shows the corresponding results for all level 2 runs, which clearly indicate that $\gamma_{\rm max} \approx 1$, or less. This is a strong indication that cusps as steep as $r^{-1.2}$ do not exist in CDM halos (as recently claimed by Diemand et al). We do note, however, the results of Taylor & Navarro (2001), who predict a power-law central cusp of $r^{-3/4}$, which is still *shallower* than the maximum allowed slope for any of our runs and hence is not ruled out by our data.

3.4.2 Velocity Structure

Fig. 3.17 shows the velocity dispersion and anisotropy profiles for halo Aq-A at different resolutions. Lines of different thickness and color have the same meaning as in all previous plots. The results shown in Fig. 3.17 again demonstrate the remarkable convergence achieved in the Aquarius simulation series, as well as a couple of other important points. The first of these regards the *shape* of the velocity dispersion profile: $\sigma(r)$ increases gradually from the halo center out to a well defined maximum before decreasing again to the virial radius. This results in a profile that looks remarkably similar to the $\rho\ r^2$ profiles shown in Fig. 3.10. This coincidence indicates an intimate connection between the radial dependence of mass and of

velocity dispersion. The second point concerns the anisotropy profile, which clearly exhibits a non-monotonic radial dependence: a roughly isotropic central velocity distribution becomes gradually more radial towards the outer regions, but isotropic again near the edge of the system.

In Fig. 3.18 we plot the velocity dispersion and anisotropy profiles for all 6 level 2 runs, which clearly show that the above behavior is not unique to halo Aq-A. All six halos exhibit velocity dispersion profiles with a characteristic maximum, as well as a non-monotonic dependence of velocity anisotropy on radius. Perhaps more important is the clear lack of self-similarity in the velocity structure of the halos. This is explicitly shown by our choice of normalization: $\sigma(r)$ profiles are chosen to match at $\sigma_{\rm max}$, the maximum velocity dispersion, and $r = r(\sigma_{\rm max})$, the radius at which this is achieved.

This scaling demonstrates that, like the $\rho(r)$ profiles, the $\sigma(r)$ profiles differ subtly but significantly amongst halos. The most striking case is, again, that of halo Aq-E: the velocity dispersion profile, like the density profile, is much broader than the others. This would seem to indicate that departures from self-similarity in density and velocity structure are tightly linked, and suggests that these halos may share a common property that combines the density and velocity dispersion. We explore this connection in more detail in the next section, and again in Chapter 4.

These results may help us assess the recent claims by Hansen & Moore (2006) of a dynamical relation between the local slope of the density profile and (local) velocity anisotropy. Since $d\ln\rho/d\ln r$ is clearly monotonic with radius (Fig. 3.14), whereas the $\beta(r)$ profiles are not (Fig. 3.18), the trivial linear relation proposed by Hansen & Moore appears to be at odds with the simulations presented here.

In Fig. 3.19 we show this explicitly for all level 2 Aquarius runs. Here we plot the local value of the velocity anisotropy parameter β versus the logarithmic slope of the density profile at the same radius. We use open circles for points with $r_{\rm conv}^{(1)} \leq r \leq r_\sigma$ and solid circles for the outer regions ($r_\sigma \leq r \leq r_{200}$). As in all

previous plots, different colors denote the different level 2 runs; the relation proposed by Hansen & Moore is shown as a dashed line. Fig. 3.19 illustrates that this simple relation provides a reasonable (though not perfect) description of the simulated data within r_σ, where both the anisotropy and logarithmic slope profiles are monotonic with radius. The non-monotonicity of the anisotropy profiles in the outer regions, however, leads to strong departures from the simple relation suggested by Hansen & Moore.

3.4.3 Phase-space Density Profiles

The similarity in the shapes of the $\rho\ r^2$ and $\sigma(r)$ profiles shown in the previous sections indicate that there may be a simple scaling between the densities and velocity dispersions across dark matter halos. This connection is best appreciated by considering the pseudo-phase-space density profile, quantified by ρ/σ^3. It is important to realize that this quantity is *not* the true coarse-grained phase-space density of our simulations, nor its spherical average, but rather a quantity that is inversely proportional to the local *entropy* of the dark matter at a given radius. We calculate ρ/σ^3 directly from estimates of $\rho(r)$ and $\sigma(r)$ computed, as before, in spherical shells.

In Fig. 3.20 we show the ρ/σ^3 profile for halo Aq-A, together with the expectation of Bertschinger (the latter shown as a dot-dashed line in each panel). The residuals in the lower panels of Fig. 3.20 are deviations from Bertschinger's law normalized to match within the radius r_{-2}. Note that, unlike the density profiles, the phase-space density profiles have *only one free parameter*, and still match the data to better than about 20% at *all* radii within r_{200}, even though substructure in the halo outer regions induce substantial noise in the dynamical estimates. Note that the residuals increase when one considers the "radial phase-space density" profile; Bertschinger's law appears to concern the full kinetic energy content of a given shell rather than just the contribution from radial motion. This is shown in the

right-hand panels of Fig. 3.20.

A similar plot for all level 2 runs is given in Fig. 3.21, and confirms that the power-law nature of the phase-space density profile is a general feature common to all dark matter halos. Also in Fig. 3.21 we see that the simple power-law scaling is preserved when only radial motions are considered, but the best-fitting exponent differs systematically from -1.875, and prefers slightly steeper slopes. This is seen clearly in the lower-right panels of Fig. 3.21, where the residuals are shown relative to the best-fitting $\rho/\sigma^3 \propto r^{-\chi}$. We list the value of the best-fit power-law exponents for both ρ/σ^3 and ρ/σ_r^3 (χ and χ_r respectively) in Table 3.3.

Perhaps the most important result in Fig. 3.21 is that there appears to be very little halo-to-halo scatter when considering the phase-space density profiles. This point is illustrated clearly by considering, again, halo Aq-E, which was a clear outlier in the density, velocity dispersion, and anisotropy profiles. When considering ρ/σ^3 this halo is virtually indistinguishable from the others, and follows Bertschinger's law very accurately.

Though the origin of the phase-space density stratification is unknown, it is possible to exploit it in order to place constraints on the asymptotic structure of the central cusp, under the plausible (though unproven) assumption that the power-law behavior extends all the way to the halo center. This was the approach of Taylor & Navarro (2001), who used this assumption to show that, for isotropic systems, a power-law phase-space density implies a density cusp which approaches $r^{-0.75}$ at the center. This is consistent with the results presented in Fig. 3.14, which only rule out cusps steeper than $\sim r^{0.9\pm0.1}$. Simulations of even larger dynamic range are required to explore whether the asymptotic slope of Taylor & Navarro holds in the innermost unresolved regions of a halo.

3.4.4 Summary

We have presented results from a series of ultra-highly resolved simulations of Milky Way-like dark matter halos: the *Aquarius project*. Our simulations have been run at a variety of numerical resolutions and in the proper ΛCDM cosmological context. The set includes the largest simulation of its kind reported to date; a ~ 4.4 billion particle simulation in which the final object has ~ 1.1 billion particles within the virialized region of the halo, r_{200}. This particular halo has been simulated five times, with mass resolution increasing by a factor of about 2000 from the lowest to the highest resolution run, allowing for a comprehensive numerical convergence study on the structure and substructure of this halo. The other five simulations in our sample resolve halos with between 100 and 200 million particles within the virial radius at $z = 0$.

In § 3.3 we analyzed the basic statistics, spatial distribution, and dynamics of substructure halos in each of the Aquarius runs. Our main conclusions regarding the *substructure* content of these halos are as follows.

- The abundance of dark matter subhalos in the Aquarius simulations is significantly higher than reported by other groups, in particular the *Via Lactea* simulations of Diemand et al (2008). The subhalo mass and peak circular velocity distributions show very little scatter from halo-to-halo suggesting that cosmic variance is *not* the origin of the discrepancy.

- The total mass in substructure is bounded to a small fraction of the total host halo mass, suggesting that a substantial smooth halo component exists in the Milky Way. The smooth component becomes increasingly dominant towards the halo center, with a total substructure mass fraction less than $\sim 10^{-3}$ within the solar circle. This implies that the dark matter through which the earth orbits is very smooth, and near-earth encounters with substructures should be rare.

- The spatial distribution of subhalos in Milky Way-like dark matter halos is substantially biased relative to the dark matter, with subhalos avoiding, in general, the innermost regions. This spatial bias extends over *five orders of magnitude* in subhalo mass, and the distribution of low-mass and massive subhalos are essentially indistinguishable.

- The kinematics of the subhalo population is also roughly independent of subhalo mass and is biased with respect to the kinematics of the dark matter halo. At any given radius, the subhalo velocity distribution is more isotropic than the dark matter; subhalos follow nearly isotropic orbits near the halo center, these orbits become slightly radially biased at intermediate radii, before becoming isotropic again near the edge of the system.

In § 3.4 we presented our analysis of the structure of the main halo in each Aquarius simulation. Our main conclusions regarding the *structure* of Milky Way-like dark matter halos are as follows.

- Density profiles deviate slightly but systematically from the from proposed by NFW, and are better described by a profile with a power-law logarithmic slope, such as the Einasto profile. Deviations from the NFW formula are the largest in the halo inner regions, where the NFW profile systematically *underestimates* the spherically averaged density. The steeply cusped Moore profile provides an inaccurate description of the structure of our six halos.

- We find convincing evidence that the density profiles of dark matter halos are *not* strictly universal and that the Einasto "shape" parameter, α, varies from halo to halo. This complements previous work by Gao et al (2008) and Hayashi & White (2008) who find that α varies systematically with halo mass. The non-universality observed in the density profiles of our simulated halos extends to their kinematic structure; velocity dispersion and anisotropy profiles differ significantly from halo-to-halo.

- Departures from self-similarity are less evident, or perhaps absent, when considering the phase-space structure of dark matter halos, quantified by the pseudo-phase-space density profile, ρ/σ^3. The phase-space density profiles are very accurately described by a power-law with $\rho/\sigma^3 \propto r^{-1.875}$; the *same* power-law derived analytically by Bertschinger for spherical infall onto a point mass perturber in an otherwise unperturbed Einstein-de Sitter universe. This suggests a limited sense in which dark matter halos can be considered to be "universal".

- Density profiles show no sign of converging to an asymptotic power-law in the inner regions, but rather shallow continuously down to the innermost resolved point. In our highest resolution run the *maximum* asymptotic slope is $\sim r^{-0.9}$, significantly shallower than the asymptotic slope predicted by Navarro, Frenk, & White, but steeper than that of Taylor & Navarro.

- Unlike the density profiles, the velocity anisotropy profiles of our six galaxy-sized halos have a non-monotonic dependence on radius. Halos have roughly isotropic central velocity distributions that gradually become more radially dominated at intermediate radii, but more isotropic again near the virial radius. Given the power-law dependence of the logarithmic density slope on radius, this implies that no simple linear relation between anisotropy and slope can hold across the entire halo. The simple linear relation proposed recently by Hansen & Moore (2006) provides a reasonable description in the halo inner regions, where both anisotropy and slope are monotonic functions of radius, but fails at large radii.

We have presented the basic properties of the structure and substructure of ΛCDM halos using the highest resolution simulations of Milky Way-like dark matter halos ever performed: the Aquarius Simulations. In our approach, we include a dedicated effort to validate numerical convergence by resimulating one of the our

halos five times, with mass resolution increasing by a factor of roughly 2000 from the lowest to highest resolution run. To quantify halo-to-halo scatter we have also resimulated six halos with between 100 and 200 million particles within the virial radius at $z = 0$.

The Aquarius simulations provide robust predictions for the structure of dark matter halos down to scales of order 100 pc, and allows for a direct comparison with a number of observations with minimal extrapolation. We recognize, however, that our simulations probe the regime where baryons have a substantial dynamical impact. Our simulations thus provide reliable theoretical predictions for the limiting case of *pure dark matter halos*; which will undoubtedly be modified in non-trivial ways by the presence of baryons.

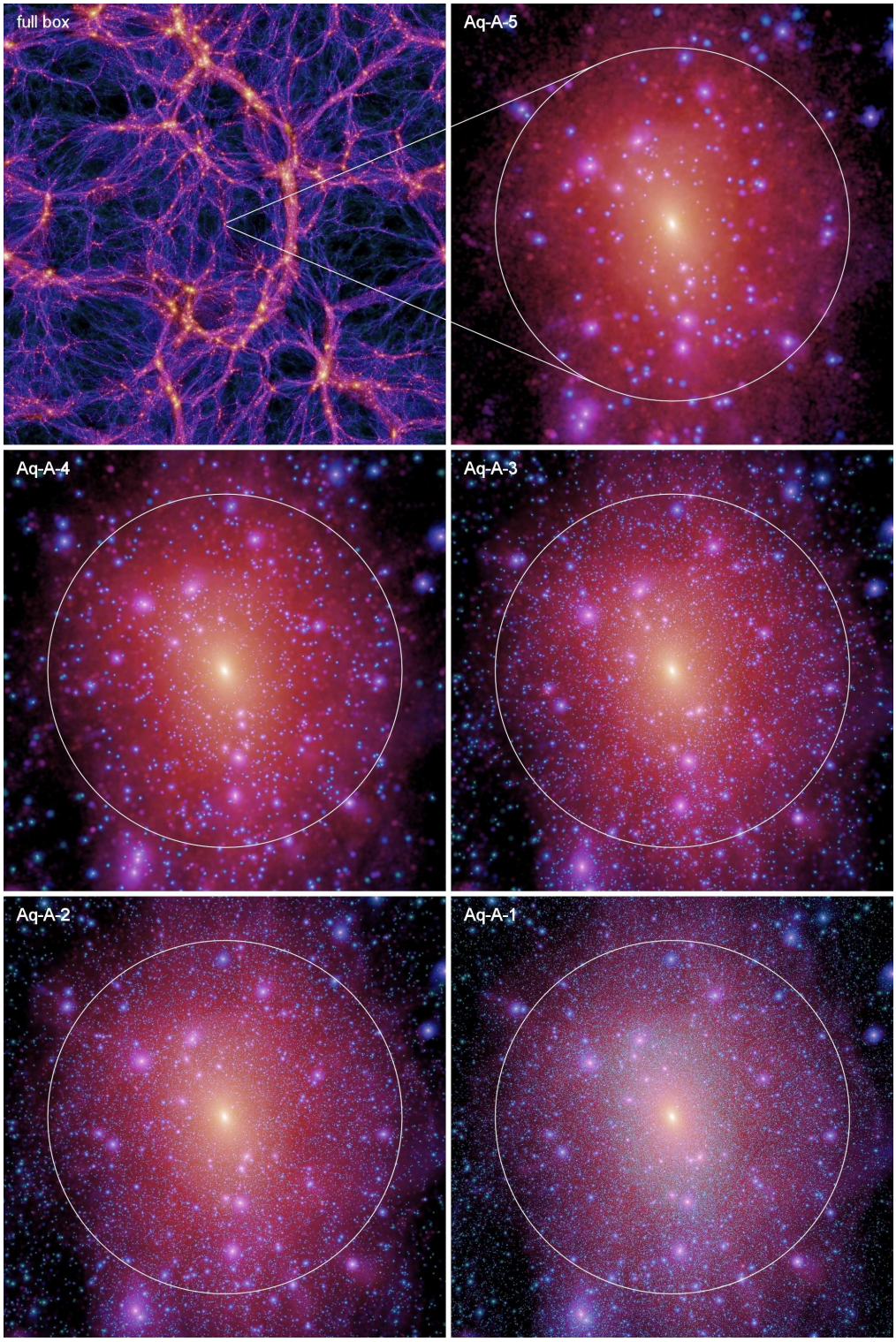

Figure 3.1: Projections of Aquarius halo Aq-A at different resolutions. Credit for Fig.'s 3.1 and 3.2 given to Volker Springel.

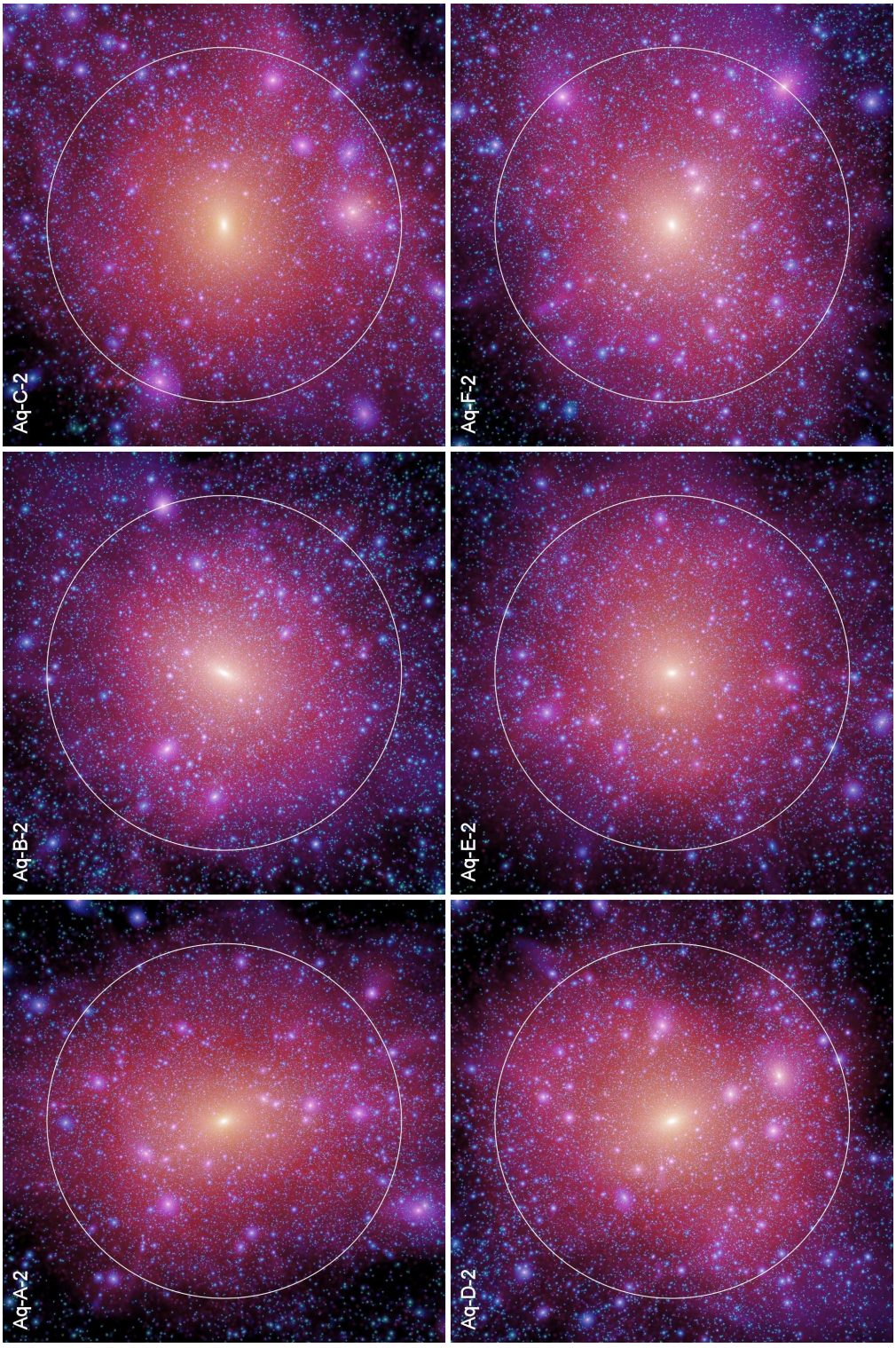

Figure 3.2: Projections of all level 2 Aquarius halos. Credit for Fig.'s 3.1 and 3.2 given to Volker Springel.

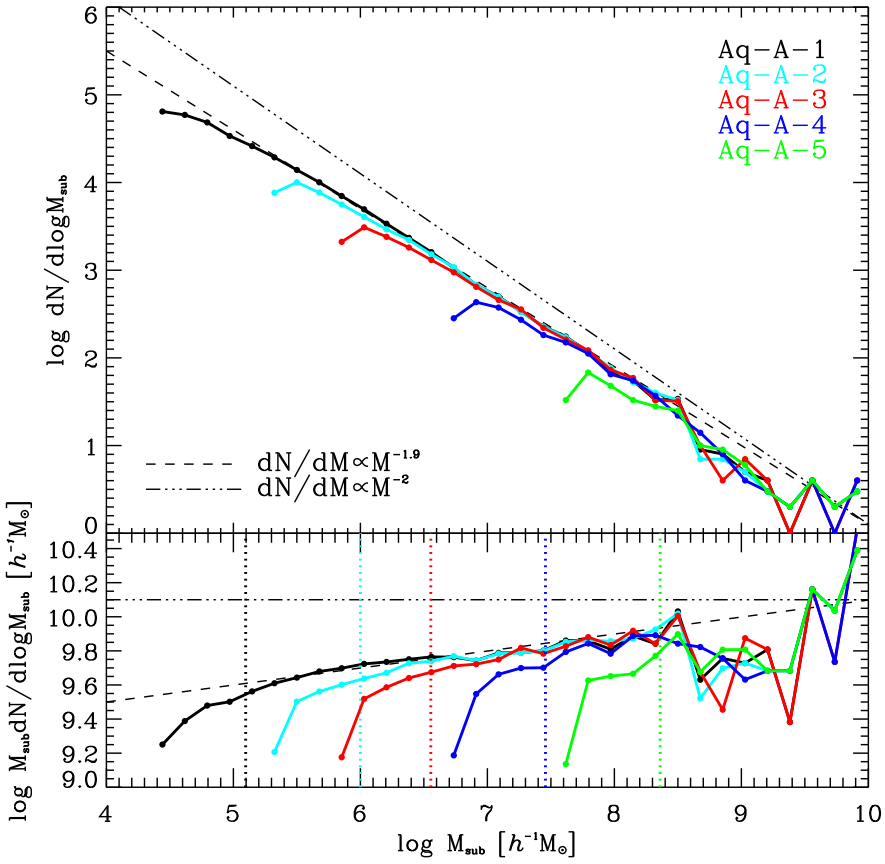

Figure 3.3: Differential substructure mass functions for halo "Aq-A" at different resolutions. Top panel shows the number of subhalos per logarithmic mass interval; bottom panel shows the total mass in subhalos per logarithmic mass interval. Each mass function is limited to subhalos identified within r_{50} having at least 20 particles. The dashed and triple-dot-dashed line show, respectively, the power-law $dN/dM \propto M^{-1.9}$ and the logarithmically divergent case, $dN/dM \propto M^{-2}$. Vertical lines in the lower panel are used to mark the 100 particle limit.

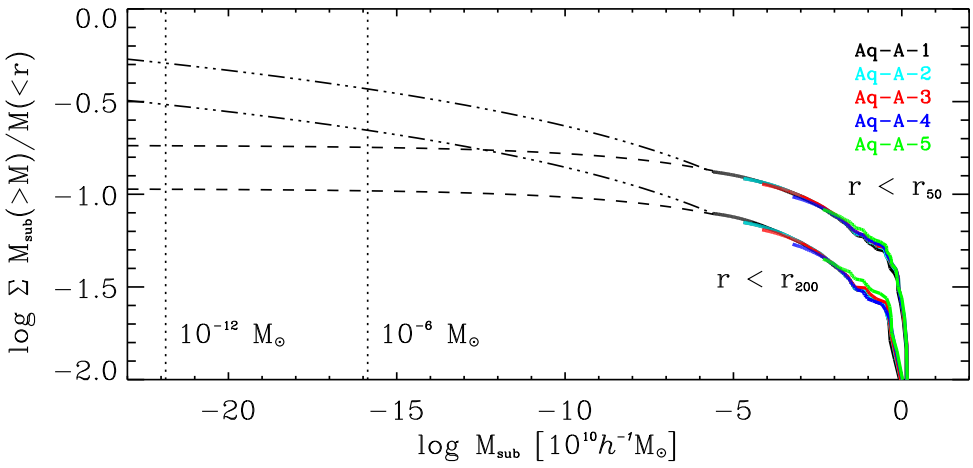

Figure 3.4: Total mass in subhalos above a given limiting mass, M_{sub}, for subhalos identified within r_{200} and within r_{50} (halo Aq-A). We extrapolate the data to the thermal free streaming limit (shown as vertical lines) assuming that the mass function follows $dN/dM \propto M^{-1.9}$ (dashed) and $dN/dM \propto M^{-2}$ (triple-dot-dashed). In both cases there is a substantial smooth halo component. The substructure mass fraction decreases significantly between r_{50} and r_{200}.

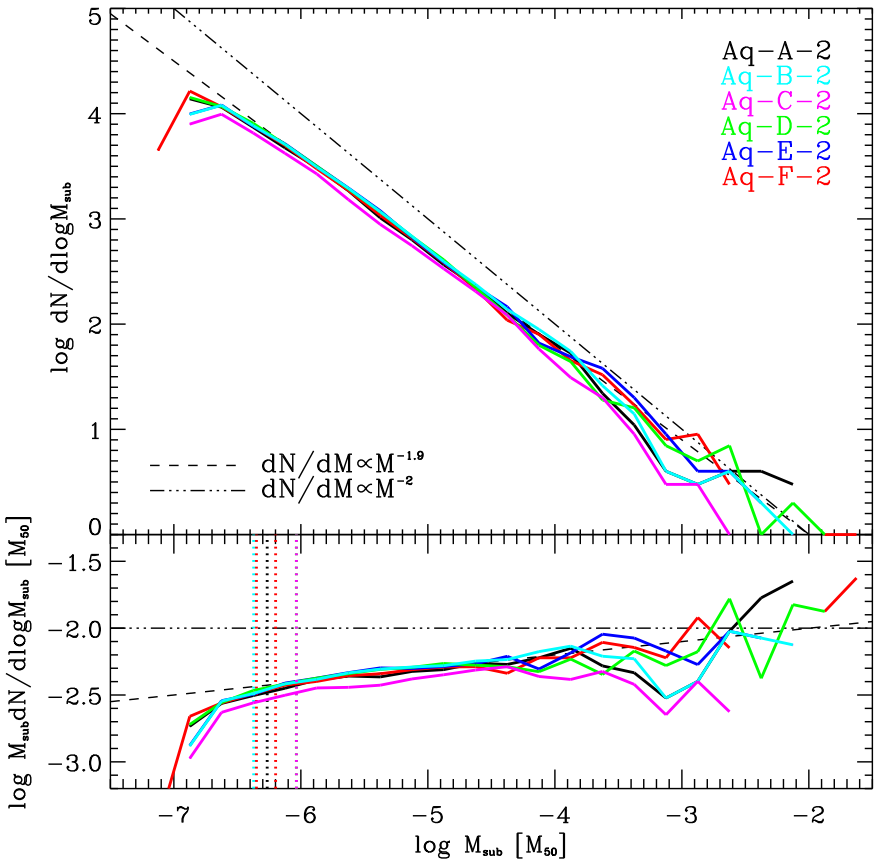

Figure 3.5: Differential substructure mass functions for all level 2 Aquarius simulations. Mass functions are limited to subhalos containing at least 20 particles that are, at $z = 0$, within r_{50}. Top panel shows the number of subhalos per logarithmic mass interval; bottom panels show the total mass in subhalos per logarithmic mass interval. Subhalo masses are normalized by M_{50}, the mass of the main halo contained within r_{50}. Power-law profiles corresponding to $d\mathrm{N}/d\mathrm{M} \propto \mathrm{M}^{-1.9}$ (dashed), and $d\mathrm{N}/d\mathrm{M} \propto \mathrm{M}^{-2}$ (triple-dot-dashed) are shown for reference. Vertical lines in the lower panel marks the 100 particle limit for each simulation.

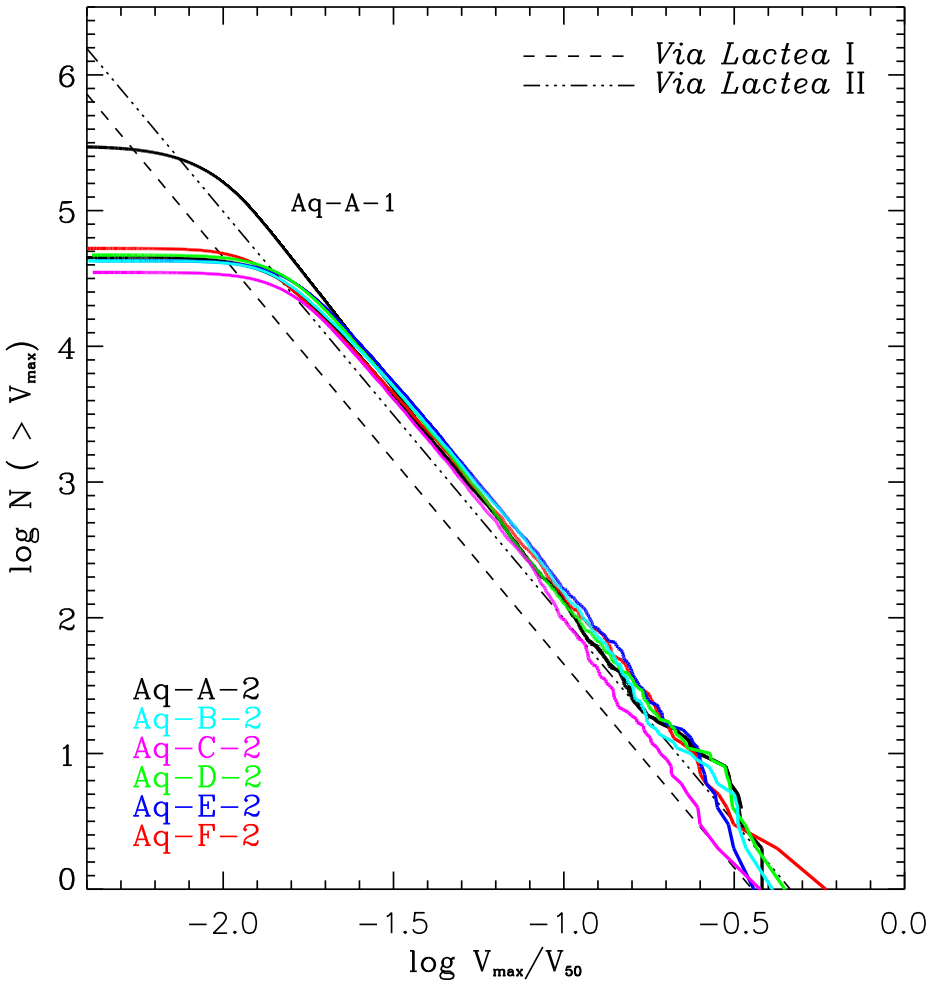

Figure 3.6: Cumulative distribution of subhalo peak circular speeds for subhalos identified within r_{50} in halo Aq-A-1 and all level 2 simulations. Subhalo peak circular velocities are normalized by V_{50}, the characteristic circular speed at r_{50}. For comparison we include the cumulative distributions shown to fit the *Via Lactea* I and II simulations, appropriately rescaled to the units used here.

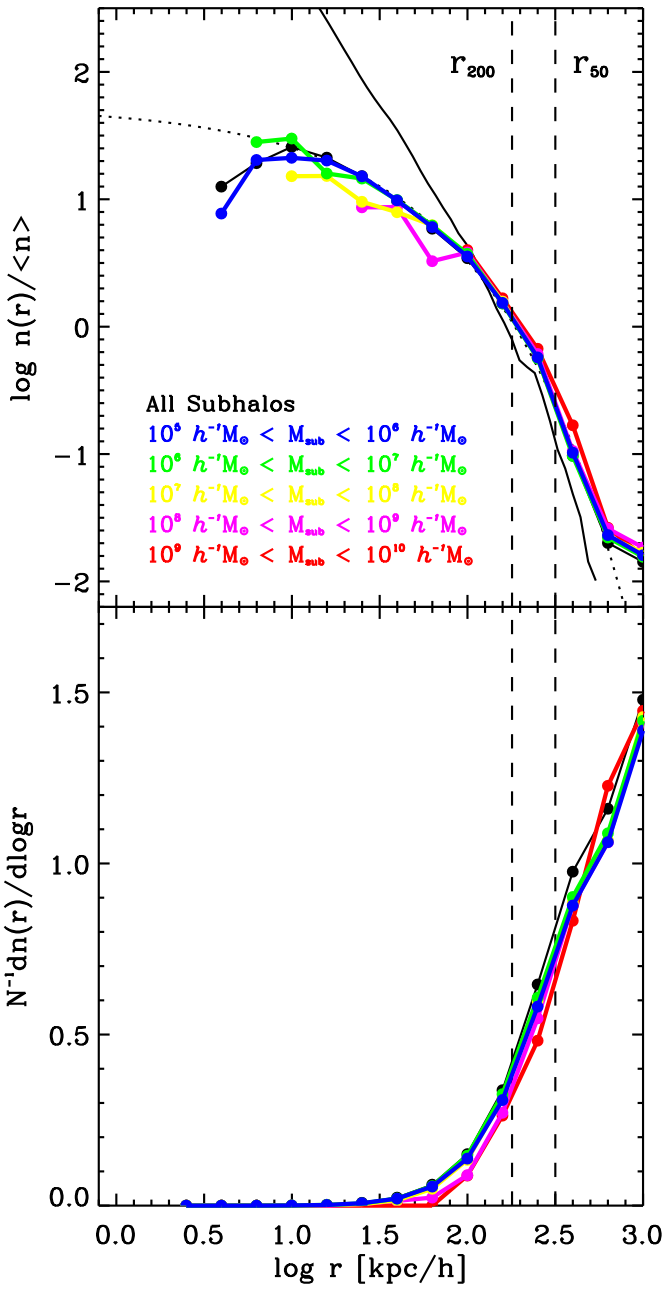

Figure 3.7: (Top panel) The number density profiles for subhalos in various mass bins in our highest resolution run (Aq-A-1). Each profile is normalized by the sample mean number density within r_{50}. The density profile of the dark matter (in arbitrary unit) is shown as a thin black line. (Bottom panel) The fraction of subhalos in a given mass bin as a function of radius for halo Aq-A-1.

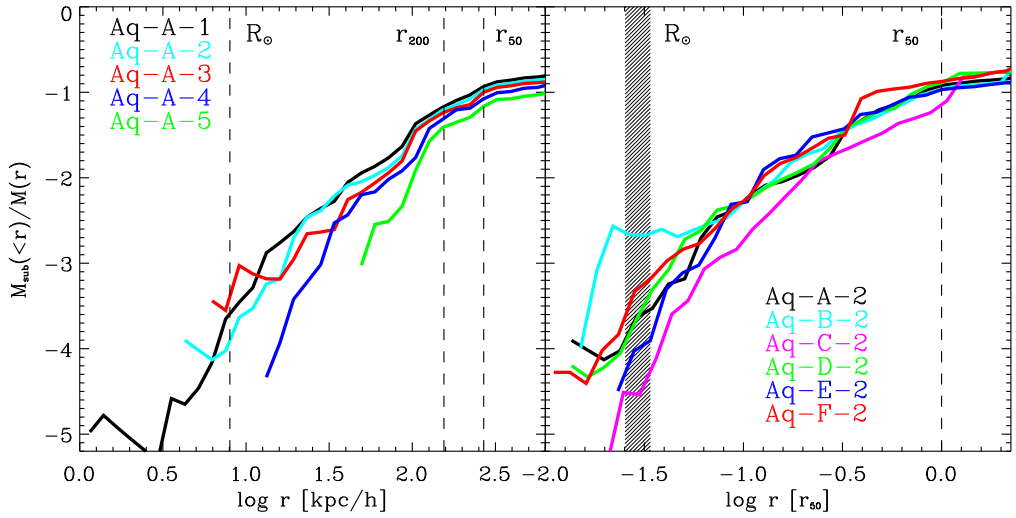

Figure 3.8: Cumulative substructure mass fractions as a function of radius for halo Aq-A at different resolutions (left), and for all level 2 simulations (right). In the left panel vertical lines mark the characteristic radii r_{50} and r_{200}, as well as the location of the solar circle, $R_\odot = 8$kpc. In the right panel we mark r_{50} with a vertical line and a shaded band highlights $R_\odot$. The central regions of the halo are dominated by a smooth distribution of mass, with significant substructure in the outer regions of the halo only. The substructure mass fraction within the solar circle is small, typically less than about 0.1%.

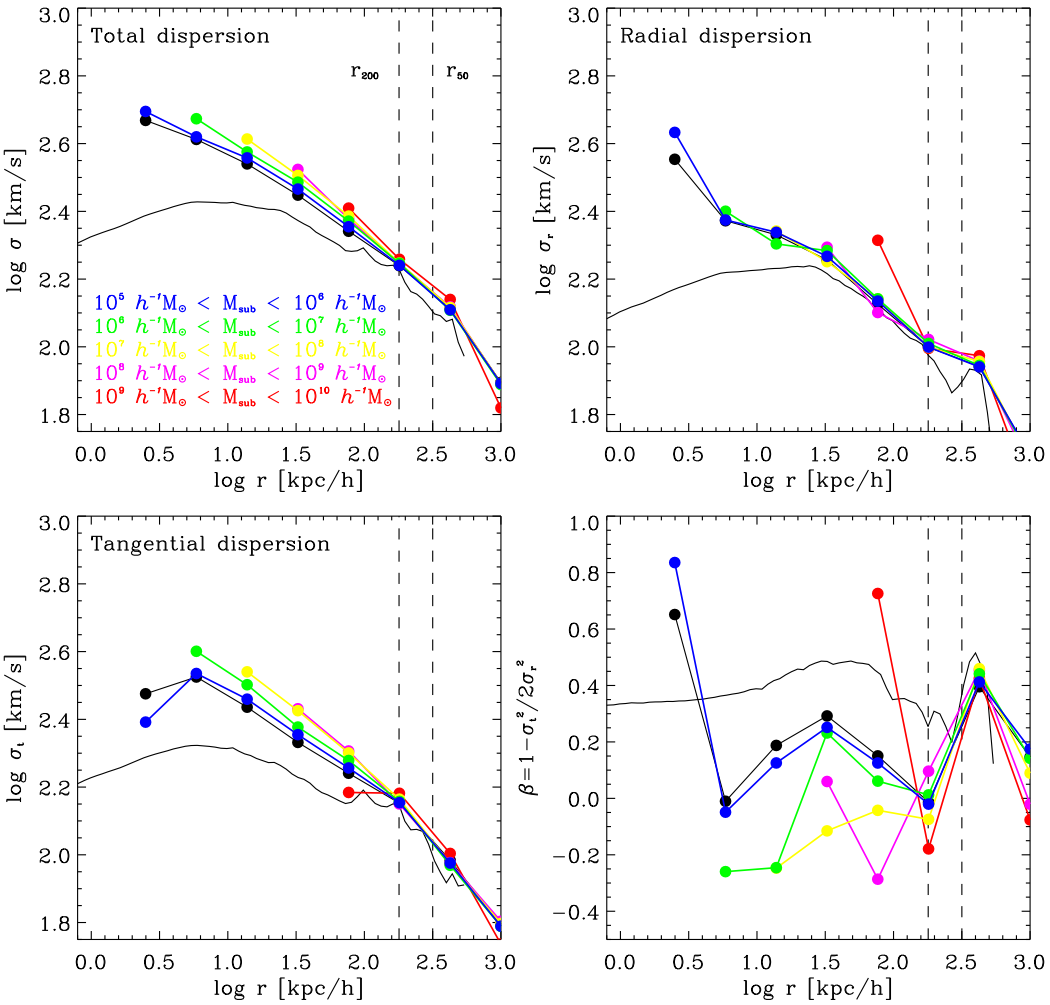

Figure 3.9: Velocity dispersion and anisotropy profiles for subhalos in Aq-A-1, selected by mass. Top-left panel shows the total 1-dimensional velocity dispersion; top-right the radial component only. The lower-left and right panels show, respectively, the tangential velocity dispersion and the velocity anisotropy profiles. Like the spatial distribution, the dynamics of the subhalo population is also biased with respect to the dark matter: subhalos near the halo center are dynamically hotter than the dark matter, and appear to follow orbits with a larger tangential bias than the dark matter halo. The kinematics of the subhalo population is largely independent of mass, particulalrly in radial velocity dispersion. There appears to be a slight mass-dependence to tangential velocity disperions such that more massive systems follow slightly more tangential orbits at any radius.

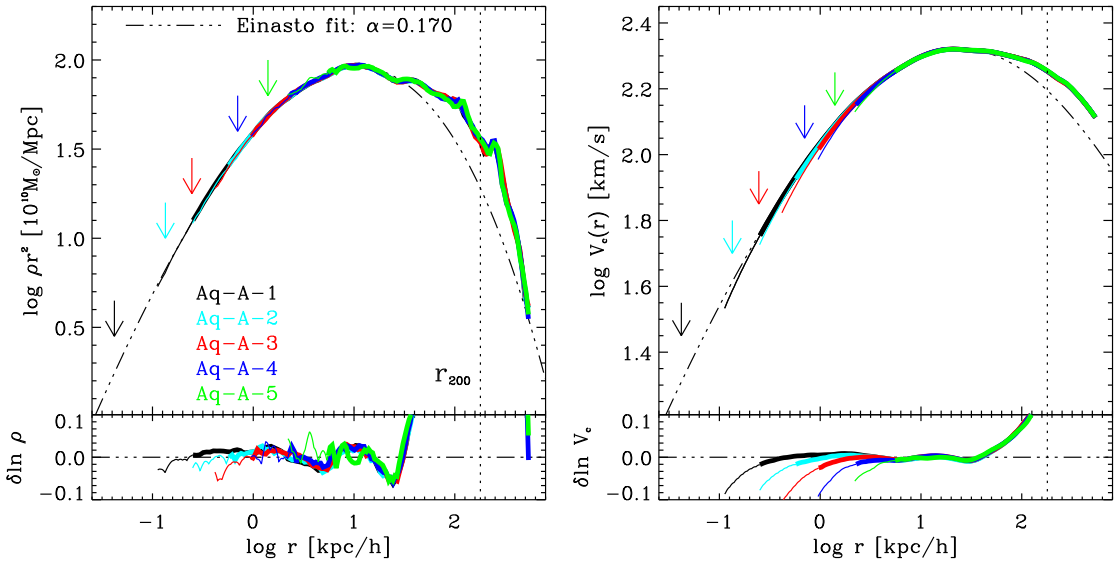

Figure 3.10: Density (left) and circular velocity (right) profiles for the Aq-A halo simulation series. Different colors correspond to different resolution runs, as labeled in the figure. The density profile is multiplied by r^2 in order to emphasize small deviations. Profiles are shown from $\sim 3\ r_{200}$ down to the "convergence radius", $r^{(1)}_{\rm conv}$, corresponding to the radius where the relaxation time is of the order of the age of the Universe. The thick portion of each profile indicates the region ($r > r^{(7)}_{\rm conv}$) where stricter convergence is demanded. At $r^{(7)}_{\rm conv}$ circular velocity estimates converge to better than 2.5% (see Fig. 3.11). The dot-dashed line shows an Einasto profile with $\alpha = 0.170$ matched at (r_{-2},ρ_{-2}), the peak in the $r^2\rho$ profile. This provides an excellent fit to the structure of the inner regions of the halo, as shown by the residuals from the fit shown in the bottom panels.

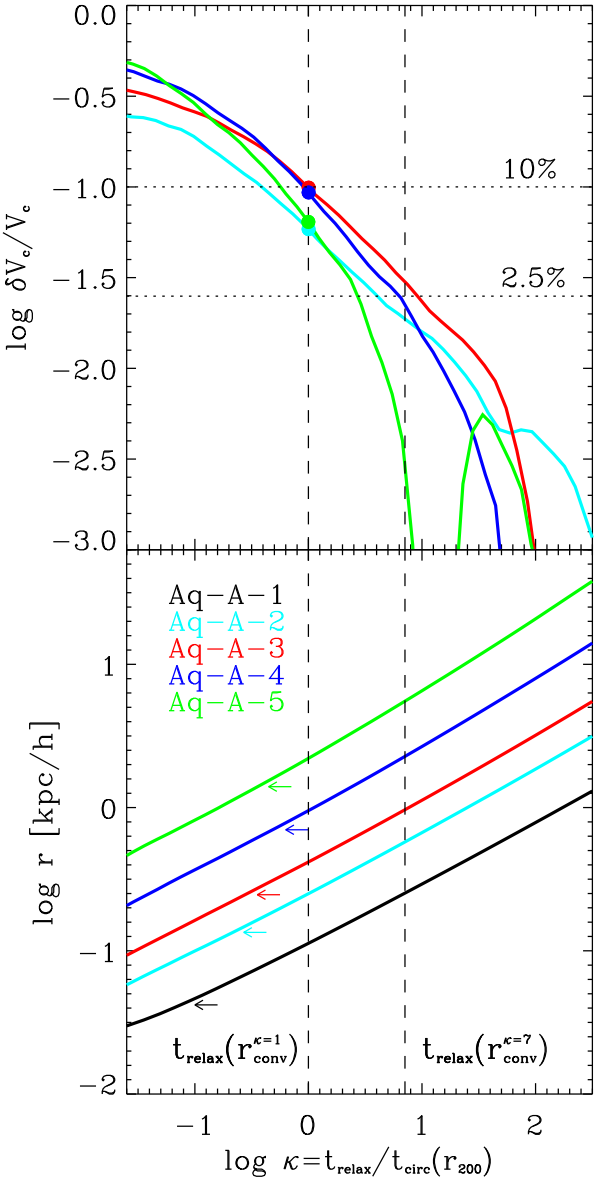

Figure 3.11: *Top panel:* Fractional deviations in the circular velocity profile of the Aq-A convergence series versus the (enclosed) relaxation time, $t_{\rm relax}$, expressed in units of the circular orbit timescale at the virial radius, $t_{\rm circ}(r_{200})$. Deviations are measured relative to the highest resolution halo, Aq-A-1. Note that departures from convergence for all simulations roughly overlap when expressed this way, indicating that $t_{\rm relax}$ is the main parameter determining convergence. Solid circles mark the location of the convergence criterion proposed by P03. Note that V_c estimates converge there to about 10%. A stricter convergence criterion, e.g., 2.5% convergence in V_c, is achieved at larger radii, where $t_{\rm relax} \sim 7\, t_{\rm circ}(r_{200})$ (right vertical line). *Bottom panel:* Relaxation time versus radius for all 5 Aq-A simulations. Arrows indicate $h_s = 1.4\,\epsilon_G$, the lengthscale where softened pairwise interactions are become Newtonian.

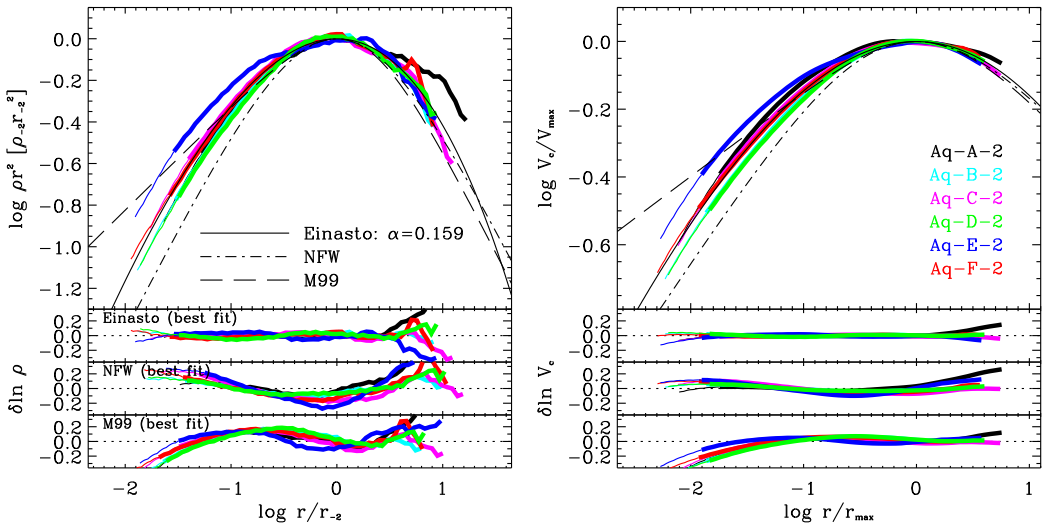

Figure 3.12: *Top panel:* Spherically averaged density profiles of all level-2 Aquarius halos. Density estimates have been multiplied by r^2 in order to emphasize details in the comparison. Radii have been scaled to r_{-2}, the radius where the logarithmic slope has the "isothermal" value of -2. Thick lines show the profiles outside $r_{\rm conv}^{(7)}$; thin lines extend inward to $r_{\rm conv}^{(1)}$. For comparison, we also show the NFW and Moore et al (1999) profiles, which are fixed in these scaled units. This scaling makes clear that the inner profiles curve inward more gradually than NFW but are substantially shallower than predicted by the Moore et al formula. The bottom panels show residuals from the *best fits* to the $r < r_{-2}$ portion of the profiles, where the fits are not compromised by the bumps and wiggles caused by substructures, using various fitting formulae. Note that the Einasto formula provides excellent fits to the inner region. The NFW profile is also able to reproduce the inner profiles fairly well, although systematic deviations are apparent at the innermost resolved point. The steeply-cusped Moore et al profile clearly gives the poorest fits.

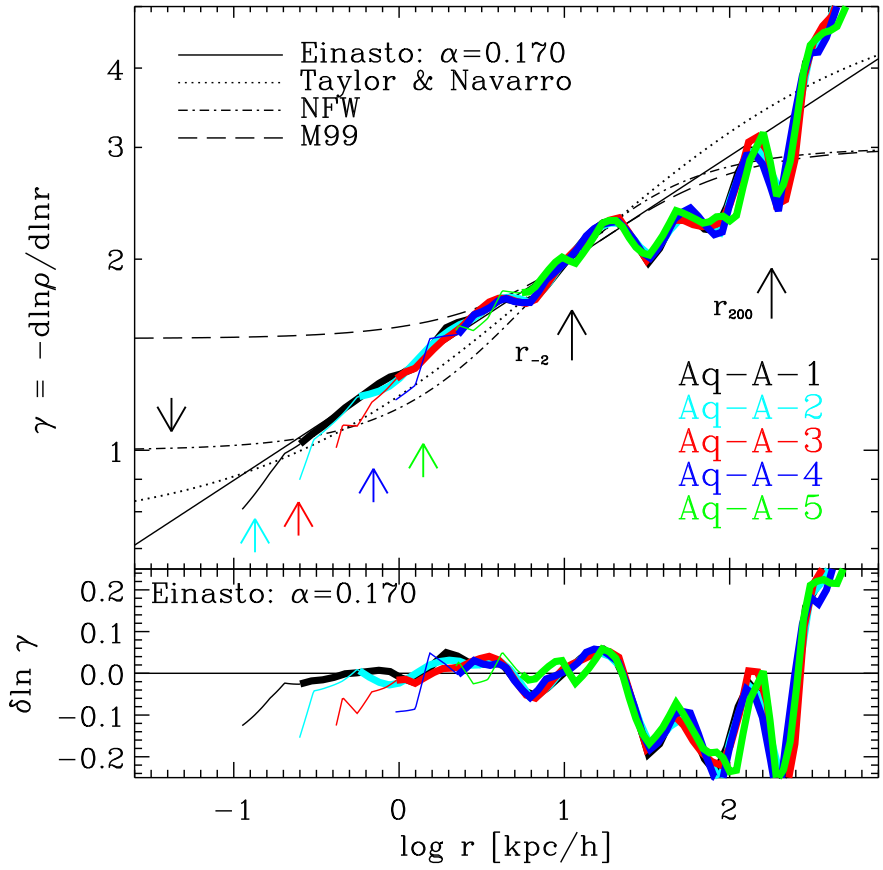

Figure 3.13: Logarithmic slope of the density profile as a function of radius for our Aq-A halo convergence series. As in other plots, thick lines show results for $r > r^{(7)}_{\rm conv}$, thin lines extend the profiles down to the less strict convergence radius $r^{(1)}_{\rm conv}$. The comparison between different simulations shows that excellent numerical convergence for the slope is achieved down to a radius intermediate between these two convergence radii. Applied to the highest-resolution Aq-A-1 simulation, this implies that the slope is shallower than the asymptotic value of the NFW profile (r^{-1}) in the inner regions. We see no sign of convergence to a steep, $r^{-1.2}$, asymptotic inner power-law, as argued in recent work (Diemand et al 2004; Diemand et al 2005). Instead, the profiles get shallower toward the center as predicted by the Einasto formula. The "critical solution" of Taylor & Navarro (2001) (which has a $r^{-0.75}$ asymptotic inner cusp) does better than NFW but not as well as Einasto in reproducing the inner regions of the halo.

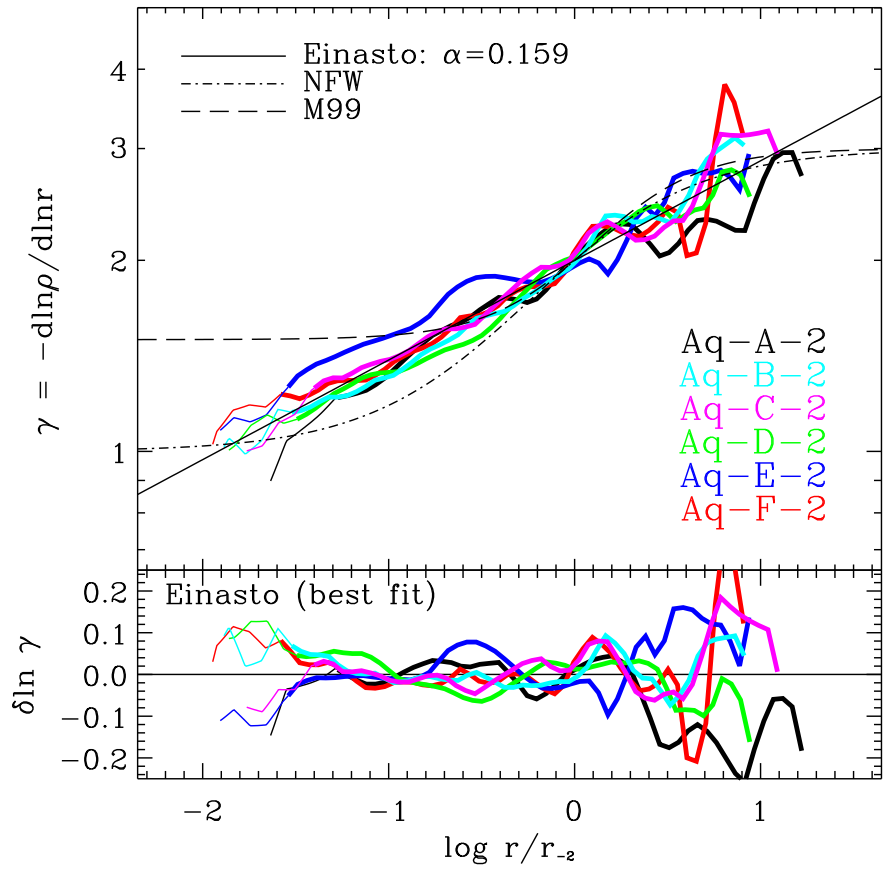

Figure 3.14: As Fig. 3.13, but for all our level-2 resolution Aquarius halos, after scaling radii to r_{-2}.

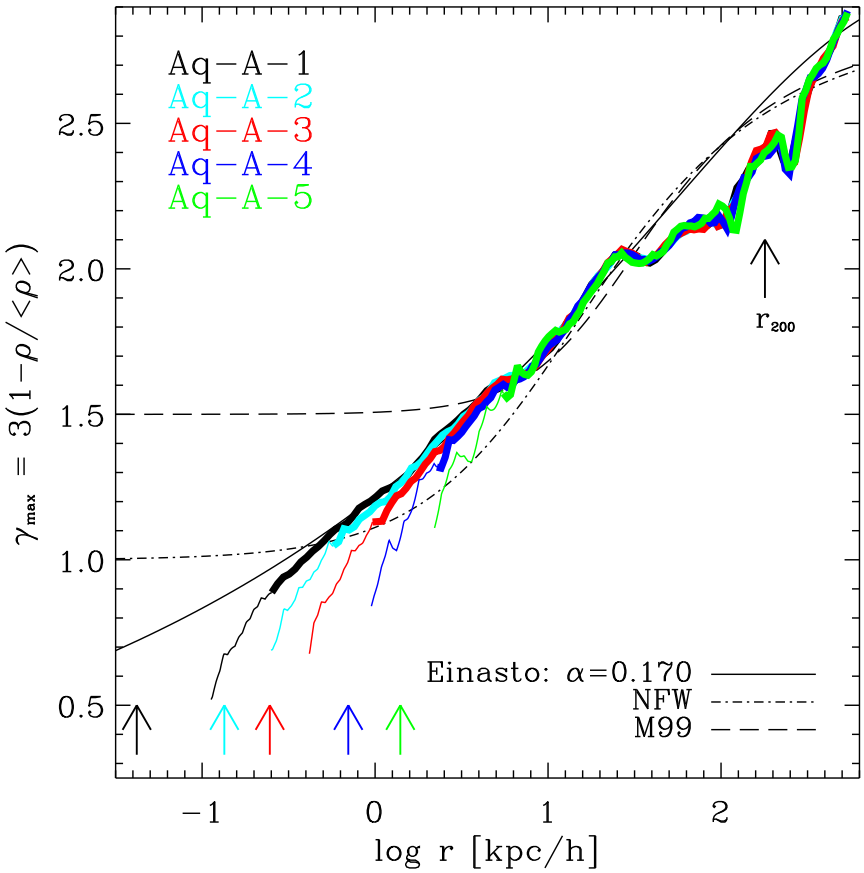

Figure 3.15: Maximum value of the asymptotic inner slope of the density profile cusp, shown as a function of radius for our Aq-A halo convergence series. Excellent numerical convergence is achieved at radii comparable or larger than $r_{\rm conv}^{(7)}$ (the inner limit of the thick lines; thin lines extend down to $r_{\rm conv}^{(1)}$). Applied to our highest resolution halo, Aq-A-1, this shows convincingly that there is not enough mass near the center to sustain a cusp steeper than $\rho \propto r^{-0.9\pm0.1}$.

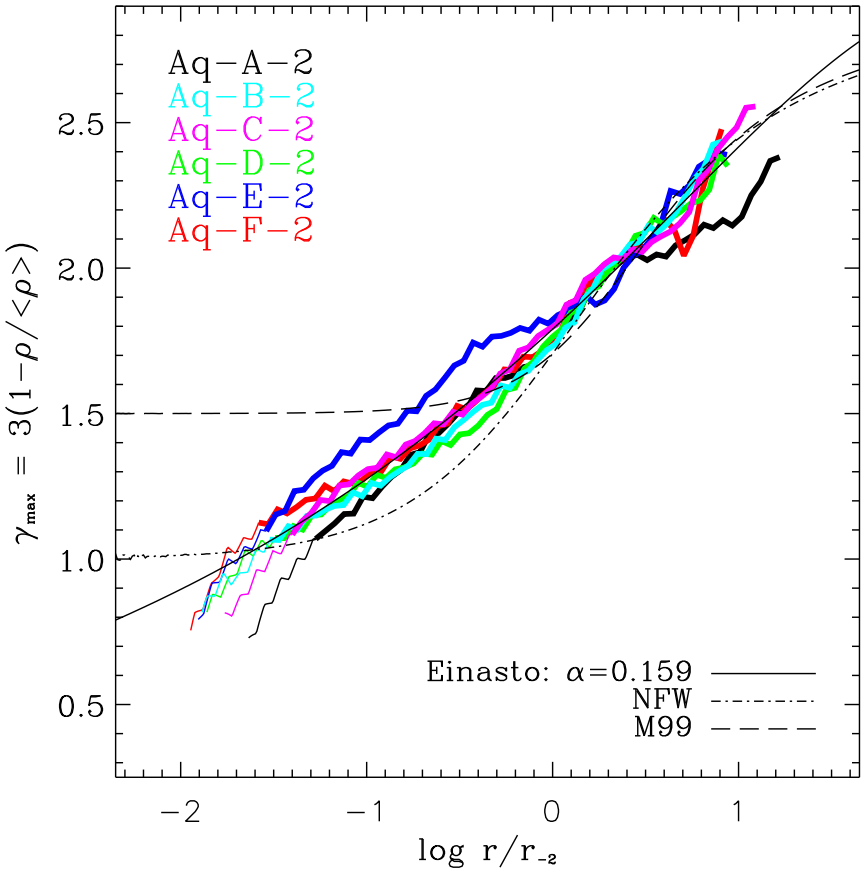

Figure 3.16: As Fig. 3.15, but for our six level-2 Aquarius halos. This confirms the results for the Aq-A halo and rules out cusps steeper than r^{-1} or so.

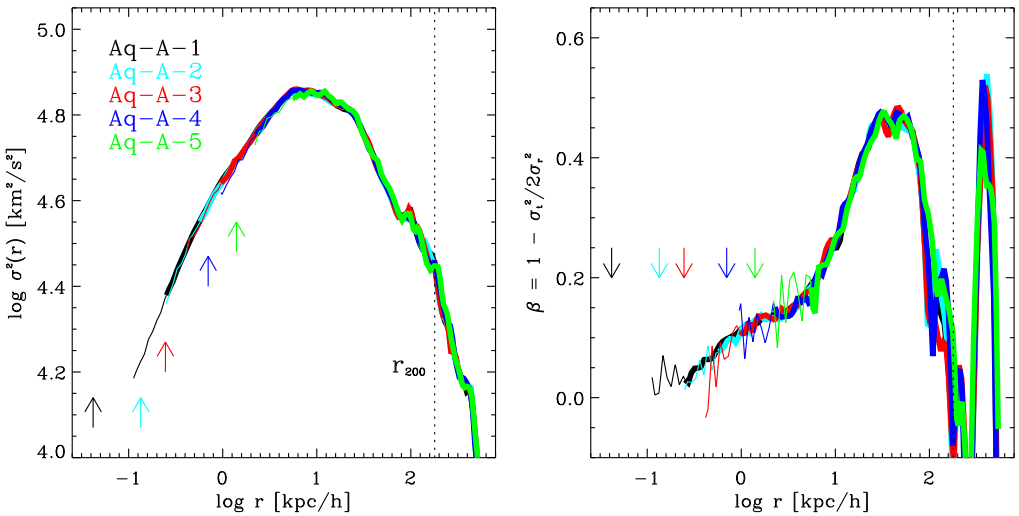

Figure 3.17: *Left panel:* Velocity dispersion profile of our Aq-A halo convergence series. Arrows, line types, and colors are as in Fig. 3.10. Note the excellent numerical convergence achieved outside the convergence radius of each simulation. The shape of the velocity dispersion profile is remarkably similar to that of the $r^2\rho$ profile shown in Fig. 3.10, highlighting the intimate structural similarity between density and velocity responsible for the power-law behavior of the phase-space density profile discussed in § 3.4.3. *Right panel:* Anisotropy profile for the Aq-A halo convergence series. Note the excellent numerical convergence and the non-monotonic radial behavior: the halo is nearly isotropic near the center, dominated by radial motions in the outskirts, before becoming again less anisotropic near the virial radius.

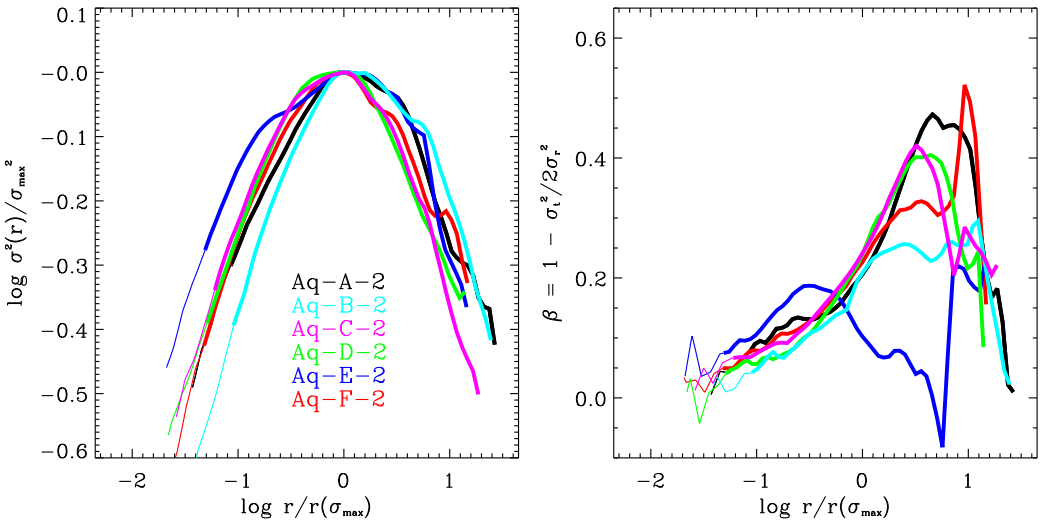

Figure 3.18: As Fig. 3.17, but for all six level-2 resolution Aquarius halos. Radii have been scaled to $r(\sigma_{\rm max}) = r_\sigma$ and velocity dispersions to the maximum value. Note the similarity in the shape of the velocity dispersion profiles between halos and also with the form of the $r^2\rho$ profiles shown in Fig. 3.10. Note as well that the non-monotonic behavior of the anisotropy highlighted in Fig. 3.17 is a general feature in our simulations. In particular, the decline in the predominance of radial motions near the virial radius seems to be a general feature of our simulations.

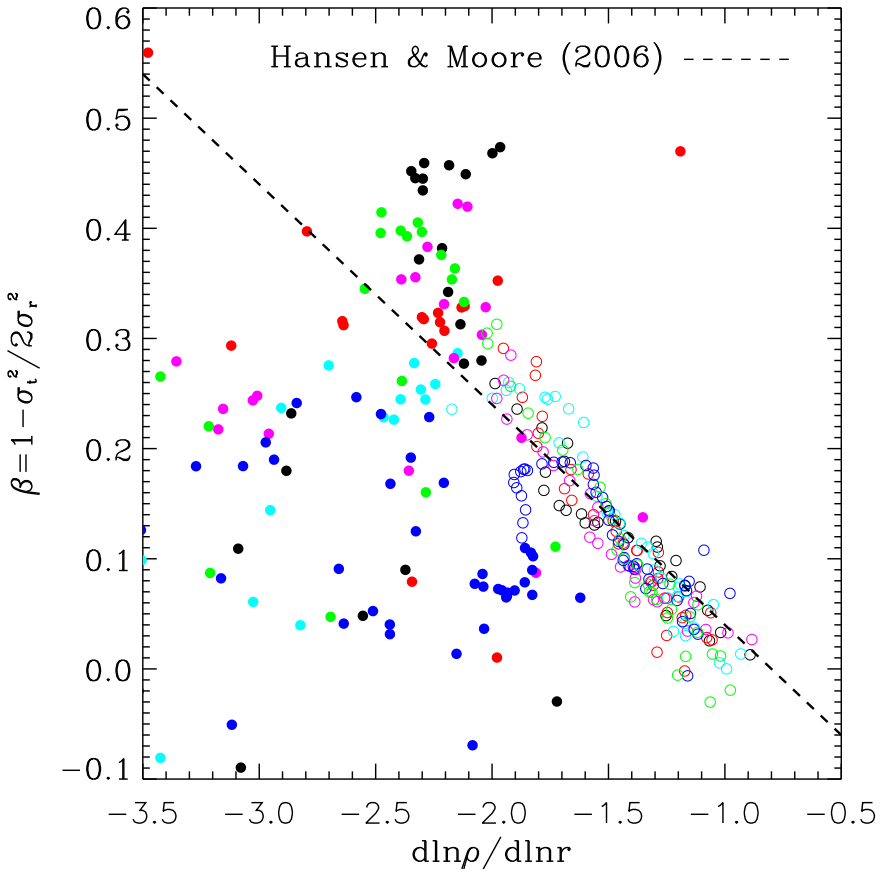

Figure 3.19: Local values of the logarithmic slope of the density profile plotted versus the velocity anisotropy, as measured in spherical shells. The relation proposed by Hansen et al (2006) is shown by the dashed line. Because the density profile steepens gradually from the center outwards whereas the velocity anisotropy is non-monotonic, there is no simple relation between these two quantities valid throughout the halo. The Hansen et al formula approximates our results reasonably well in the inner regions, but large deviations may be seen in the outer regions, where halos are approximately isotropic, and the density profile is steepest. Open circles correspond to the inner regions ($r^{(1)}_{\rm conv} < r < r_\sigma$); filled circles to the outer regions ($r_\sigma < r < r_{200}$).

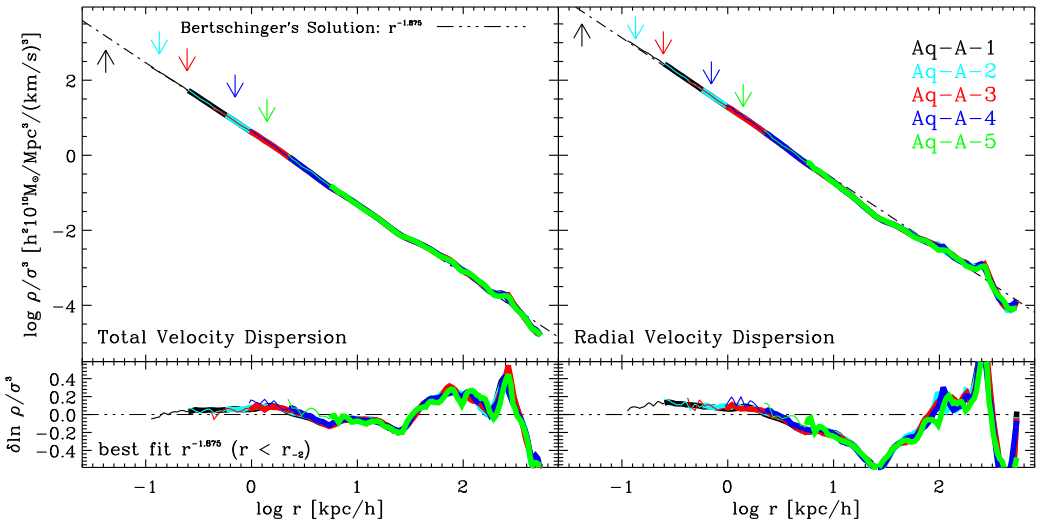

Figure 3.20: "Phase-space density" profiles for our Aq-A halo convergence series. This is estimated as ρ/σ^3, computed in concentric spherical shells. Arrows, line types, and colors are as in Fig. 3.10. Note the remarkable power-law behavior of the phase-space density, a result already anticipated by Taylor and Navarro (2001). The dot-dashed line is not a fit to the data, but rather the radial dependence of the self-similar secondary infall solution derived by Bertschinger (1985), where $\rho/\sigma^3 \propto r^{-1.875}$, matched to the inner ($r < r_{-2}$) region of the profile. Residuals from the Bertschinger solution are shown in the bottom panels. Note that the power-law behavior is best appreciated when the full 3D velocity dispersion is used (left panels). When only the velocity dispersion in radial motions is used (right panels) the deviations from the Bertschinger solution are considerably larger.

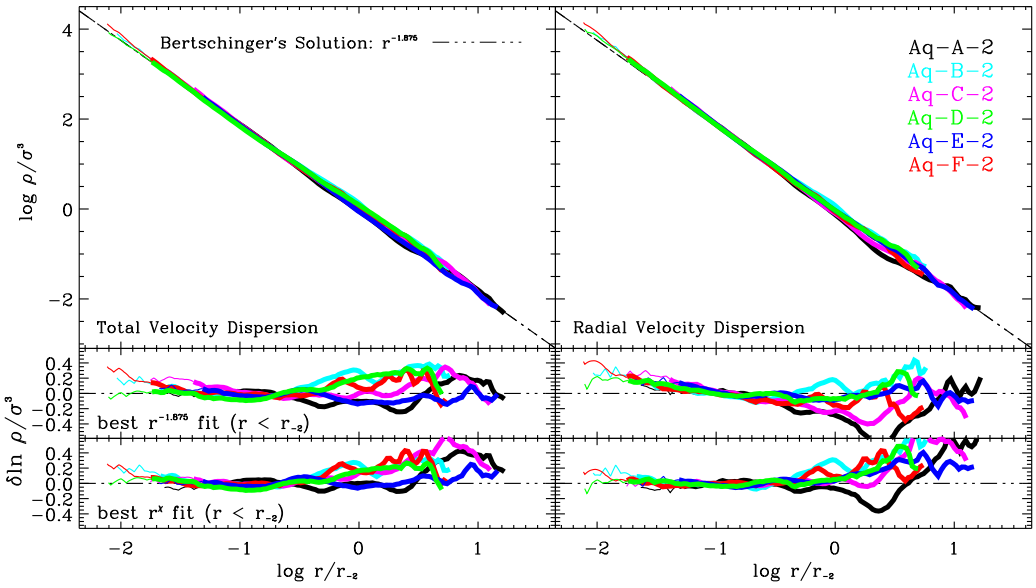

Figure 3.21: As Fig. 3.20, but for all six level-2 resolution Aquarius halos. Radii have been scaled to r_{-2}, and phase space densities to the value at $r = r_{-2}$. Note that all six halos are very well approximated by a power law with radius, and that the exponent of the power law is very close to the Bertschinger solution. In general, deviations from the Bertschinger slope are more pronounced when the radial velocity dispersion is used rather than the full 3D velocity. Residuals from best fit power-laws, $\rho/\sigma^3 \propto r^{\chi}$ are shown in the bottom panels. The values of χ are listed for each halo in Table 3.3.

Halo	$m_{\rm p}$ $[M_\odot/h]$	ϵ [pc/h]	r_{200} [kpc/h]	M_{200} $[M_\odot/h]$	N_{200} [10^6]	$V_{\rm max}$ [km/s]	$r_{\rm max}$ [kpc/h]	$\sigma_{\rm host}$ [km/s]	$\sigma_{\rm max}$ [km/s]
Aq-A-1	1.250×10^3	14	179.41	1.343×10^{12}	1074.06	208.75	20.69	117.47	261.70
Aq-A-2	1.000×10^4	48	179.49	1.345×10^{12}	134.47	208.49	20.54	117.13	261.88
Aq-A-3	3.585×10^4	88	179.31	1.341×10^{12}	37.39	209.22	20.35	117.31	262.80
Aq-A-4	2.868×10^5	250	179.36	1.342×10^{12}	4.68	209.24	20.58	117.23	262.29
Aq-A-5	2.294×10^6	500	180.05	1.357×10^{12}	0.59	209.15	22.15	116.61	260.59
Aq-B-1	4.706×10^3	48	137.02	5.982×10^{11}	127.09	157.68	29.31	89.59	190.74
Aq-C-1	1.021×10^4	48	177.26	1.295×10^{12}	126.77	222.40	23.70	124.08	270.50
Aq-D-1	1.020×10^4	48	177.28	1.295×10^{12}	126.98	203.20	39.48	113.15	254.28
Aq-E-1	7.002×10^3	48	154.96	8.652×10^{11}	123.56	179.00	40.52	101.73	215.14
Aq-F-1	4.946×10^3	48	152.72	8.282×10^{11}	167.45	169.08	31.15	96.78	204.53

Table 3.1: Basic parameters of the Aquarius simulations. We have simulated 6 different halos, each at several different numerical resolutions. The leftmost column gives the simulation name, encoding the halo (A to F), and the resolution level (1 to 5—1 is our highest resolution, 5 the lowest). $m_{\rm p}$ is the particle mass in the high-resolution region, ϵ_G is the Plummer-equivalent gravitational softening length, r_{200} is the virial radius, defined as the radius enclosing a mean overdensity 200 times the critical value for closure, M_{200} is the mass within the virial radius, N_{200} is the total number of particles within r_{200}. Other characteristic properties of the halos listed are the position ($r_{\rm max}$) of the peak ($V_{\rm max}$) of the circular velocity profile, as well as the 1D velocity dispersion of the main halo ($\sigma_{\rm host}$), as well as the peak ($\sigma_{\rm max}$) of the velocity dispersion profile.

Halo	$N_{\rm sub}$ $(< r_{200})$	$N_{\rm sub}$ $(< r_{50})$	$M_{\rm sub}$ $(< r_{200})$ $[10^{10} M_\odot/h]$	$M_{\rm sub}$ $(< r_{50})$ $[10^{10} M_\odot/h]$	$M_{\rm unres}$ $(< r_{50})$ $[10^{10} M_\odot/h]$	$M_{\rm sub}^{\rm max}$ $(< r_{50})$ $[10^{10} M_\odot/h]$
Aq-A-1	144634	297791	10.57 (7.9%)	24.31 (13.2%)	7.81 (4.2%)	32.12 (17.4%)
Aq-A-2	21052	45024	9.48 (7.0%)	22.40 (12.3%)	9.62 (5.2%)	32.02 (17.4%)
Aq-A-3	6279	13854	8.63 (6.4%)	20.88 (11.3%)	10.92 (5.9%)	31.81 (17.3%)
Aq-A-4	899	1959	7.21 (5.4%)	17.84 (9.7%)	13.45 (7.3%)	31.29 (17.0%)
Aq-A-5	120	278	6.00 (4.4%)	15.26 (8.2%)	16.56 (8.9%)	31.82 (17.2%)
Aq-B-1	24902	42537	4.15 (6.9%)	8.04 (10.5%)	8.92 (11.7%)	16.96 (22.2%)
Aq-C-1	17489	35022	5.27 (4.1%)	11.76 (7.2%)	9.64 (5.9%)	21.40 (13.0%)
Aq-D-1	22065	47014	8.43 (6.5%)	24.00 (13.1%)	9.63 (5.2%)	33.64 (18.3%)
Aq-E-1	23254	42724	6.25 (7.2%)	12.14 (10.7%)	9.28 (8.2%)	21.42 (19.0%)
Aq-F-1	26739	52640	9.04 (10.9%)	14.83 (13.4%)	8.96 (8.1%)	23.79 (21.5%)

Table 3.2: Summary of the substructure content of the Aquarius halos. $N_{\rm sub}(< r)$ refers to the total number of subhalos resolved with > 20 particles within radius r; $M_{\rm sub}$ is the corresponding total mass in bound subhalos; $M_{\rm unres}$ is the total mass in *unresolved* subhalos; and $M_{\rm sub}^{\rm max}$ is the theoretical maximum substructure mass within r_{50} which includes the contribution from unresolved subhalos (see text for details).

Halo	$r_{\rm conv}^{(1)}$ [kpc/h]	$r_{\rm conv}^{(7)}$ [kpc/h]	ρ_{-2} [$10^{10}h^2M_\odot$]	r_{-2} [kpc/h]	$\sigma_{\rm max}$ [km/s]	r_σ [kpc/h]	α	χ	χ_r	$\gamma_{\rm max}^{(1)}$	$\gamma_{\rm max}^{(7)}$
Aq-A-1	0.113	0.253	1.254×10^5	10.17	261.54	7.62	0.177	-1.898	-1.948	0.598	0.927
Aq-A-2	0.250	0.575	7.893×10^5	10.64	261.88	7.94	0.174	-1.917	-1.976	0.730	1.081
Aq-A-3	0.417	0.966	8.104×10^5	10.61	262.80	8.14	0.179	-1.926	-1.995	0.748	1.141
Aq-A-4	0.952	2.277	5.414×10^5	13.18	262.29	8.64	0.149	-1.991	-2.061	0.917	1.340
Aq-A-5	2.244	5.579	4.373×10^5	17.31	260.31	9.08	0.120	-2.015	-2.111	1.054	1.527
Aq-B-1	0.219	0.507	1.771×10^5	17.03	190.80	8.53	0.175	-1.863	-1.932	0.837	1.079
Aq-C-1	0.248	0.573	5.174×10^5	14.13	276.04	7.64	0.154	-1.946	-2.012	0.818	1.099
Aq-D-1	0.281	0.652	1.996×10^5	20.66	255.82	10.26	0.177	-1.855	-1.940	0.841	1.088
Aq-E-1	0.223	0.516	2.461×10^5	16.31	210.58	10.79	0.122	-1.912	-1.946	0.803	1.122
Aq-F-1	0.209	0.486	1.599×10^5	19.23	206.27	9.71	0.153	-1.911	-1.980	0.768	1.133

Table 3.3: Fit parameters of Aquarius halos. The first column labels each halo, as in Table **??**, the second and third list the convergence radii obtained for $\kappa = 1$ and $\kappa = 7$. These radii, $r_{\rm conv}^{(1)}$ and $r_{\rm conv}^{(7)}$, respectively, correspond to where departures from convergence in the circular velocity are expected to be of order 10% and 2.5%. The characteristic scale radius r_{-2} corresponds to where the logarithmic slope equals the isothermal value; $\rho_{-2} = \rho(r_{-2})$, and α is the best-fit Einasto parameter. χ refers to the exponent of the best fitting power-law describing the ρ/σ^3 profile. χ_r is analogous to χ, but for ρ/σ_r^3, where σ_r is the rms velocity in radial motions. All fits are computed by minimizing residuals in the region $r_{\rm conv}^{(1)} < r < r_{-2}$. Finally, $\gamma_{\rm max}$ lists the value of the maximum asymptotic slope of the density profile cusp, measured at $r = r_{\rm conv}^{(7)}$.

Chapter 4

The Universal Structure of ΛCDM halos

Abstract

We use cosmological N-body simulations to study the structure of ΛCDM halos. We focus our analysis on the spherically averaged density (ρ), velocity dispersion (σ), and phase-space density profiles (ρ/σ^3) of a sample of 15 *dynamically relaxed* systems. We add to the extensive literature on the subject by placing specific emphasis on the "universality" of these profiles, and by attempting to quantify and interpret some noticeable deviations from self-similarity. The main results of this work can be summarized as follows. The spherically averaged density profiles of dark matter halos are not strictly universal; both the global shape of the density profile and its characteristic scales depend on the details of the mass accretion history of a given system. The global shape of the density profile is reflected in the kinetic energy profiles, $\sigma^2(r)$, such that systems with more gradually changing logarithmic slopes, $\mathrm{d}\ln\rho/\mathrm{d}\ln r$, also exhibit more gradual variations in velocity dispersion. We find that the logarithmic slope of the density profile correlates strongly with the concentration of the system, suggesting that the formation history of a given halo sets not only the characteristic scales (ρ_{-2}, r_{-2}), but also its shape. This is shown by a strong correlation between the concentration parameter, $c = r_{200}/r_{-2}$, and the Einasto parameter, α, describing a given halo. The coupling between $\rho(r)$ and $\sigma(r)$ is such that the phase-space density profiles stratify radially to a well defined and universal power-law: $\rho/\sigma^3 \sim r^{-1.875}$. This is the same power-law derived analytically by Bertschinger (1985) for the spherical infall of gas onto a point mass in an expanding background.

4.1 Introduction

In the currently favored cosmogony the dominant matter component in the universe takes the form of a cold and collisionless particle, known as cold dark matter (CDM). The theoretical predictions of this model (e.g the distribution of large scale structure, the properties of the cosmic microwave background, and the structure of dark matter halos) have been studied in great detail and shown to be concordant with

an impressive array of observational data (for example, Spergel et al 2003, 2006). Remarkable advances is computational hardware and the continued improvement of numerical algorithms designed specifically for simulating the evolution of structure in the universe (e.g. Springel et al 2005, 2008) are largely responsible for its success.

Such simulation work has led to a general consensus that the virialized objects resulting from the gravitational collapse of an initial CDM overdensity share a number of "universal" structural properties: 1) the spherically averaged density profile (e.g. Navarro, Frenk & White 1996, 1997, hereafter NFW; Moore et al 1998, 1999), 2) the distribution of angular momentum with mass (Bullock et al 2001a), 3) the density slope versus velocity anisotropy (Hansen & Moore 2006; Hansen & Stadel 2006), and 4) the phase-space density profile, ρ/σ^3 (e.g. Taylor & Navarro 2001, hereafter T&N). In spite of many attempts at explaining the origin of these relations the physics regulating them remains largely unknown, but collectively they suggest that the structural and dynamical properties of dark matter halos are closely related.

The universal nature of the CDM density profile was first pointed out by Navarro, Frenk & White (1997, 1998) who proposed a simple empirical relation where the spherically averaged density takes the form

$$\frac{\rho(r)}{\rho_{\rm crit}} = \frac{\delta_c}{r/r_s(1+r/r_s)^2}. \tag{4.1}$$

Here $\rho_{\rm crit} = 3H^2/8\pi G^*$ is the critical density for a closed universe, δ_c is a characteristic density contrast, and r_s defines a radial scale. As discussed by NFW, and more recently by Neto et al (2007) and Gao et al (2007), the variables δ_c and r_s are not independent but rather correlate in a way that reflects the formation time of the halo.

It is important to note that eq. 4.1 is "universal", in the sense that it contains

*Hubble's "constant" is given by $H(z)$ and parameterized at $z = 0$ by $H(z = 0) = H_0 = 100\,h$ km s^{-1} Mpc^{-1}

two scale parameters but no adjustable shape parameter. The NFW profile is characterized by a logarithmic slope that asymptotically approaches -1 at small radii and gradually steepens to -3 in the outer regions. This gradual change in slope is a well established structural feature of dark matter halos although the true asymptotic behavior of the inner mass profile is still a matter of debate. This has led to a generalization of the NFW profile which asymptotes to $\rho \sim r^{-3}$ at large radii, but to an arbitrary power-law in the inner regions (Zhao 1996). Profiles of this sort are referred to as *generalized* NFW profiles.

The class of broken power-laws conventionally used to fit CDM density profiles have recently been questioned by several authors (Power et al 2003; Navarro et al 2004, hereafter N04; Merritt et al 2005; Prada et al 2006; Gao et al 2007). For example, N04 advanced a fitting formula where the logarithmic slope is a continuously varying function of radius:

$$\mathrm{d}\ln\rho/\mathrm{d}\ln r = -2(r/r_{-2})^{\alpha}, \tag{4.2}$$

where r_{-2} defines the radius at which $\mathrm{d}\ln\rho/\mathrm{d}\ln r = -2$, and α is a shape parameter that can be tailored to fit individual halos. The density profile corresponding to eq. 4.2 is given by

$$\ln(\rho(r)/\rho_{-2}) = -2\alpha[(r/r_{-2})^{\alpha} - 1], \tag{4.3}$$

and was first introduced by Einasto (1965) to describe the radial density profile of old stars in the halo of the Galaxy. This equation has been shown to fit the spherically averaged density profiles of CDM halos better than eq. 4.1, but at the expense of an additional shape parameter, α. For convenience we refer to eq. 4.3 as the Einasto profile.

In a recent study by Gao et al (2007) α has been shown to correlate with halo mass, varying from $\alpha \approx 0.15$ for galaxy sized halos to ≈ 0.3 for massive clusters. The analysis in the previous Chapter indicates that there is also considerable variation

in α at the galaxy mass scale, suggesting a non-trivial relation to halo mass. The origin of this correlation is still an open question, and is the motivation for the analysis in presented in this Chapter.

The structure of dark matter halos can also be described in terms of the so-called phase-space density profile, quantified by ρ/σ^3. This was the approach of Taylor & Navarro (2001, hereafter T&N), who studied a set of three simulated halos and found $\rho/\sigma^3 \propto r^{-\gamma}$ (with $\gamma \approx 1.875$) over nearly three decades in radius. Coincidentally, this is the same result derived by Bertschinger (1985) for the spherical infall of gas onto a point mass perturber in an Einstein-de Sitter universe. T&N exploit the power-law ρ/σ^3 behavior and use it to solve the isotropic Jeans equation in order to determine the radial density profile. They find that for $\gamma = 1.875$ there exists a critical monotonic solution for which the density profile follows closely the empirical NFW relation over the radial range probed by simulations.

Since the original work of T&N the power-law dependence of the phase-space density profile has been studied by a number of Authors. One example is the work of Austin et al (2005), who use Extended Secondary Infall Models, and an analysis of the Jeans equation, to study the structure dark matter halos in virial equilibrium. These Authors show that a power-law phase-space density profile is a robust feature of relaxed CDM halos. Furthermore, since these halos are studied using an extension of simple spherical infall models they do not contain substructure explicitly. Thus, as argued by Austin et al, it appears unlikely that hierarchical merging is responsible for the scale-free ρ/σ^3 distributions, but rather that something akin to violent relaxation may actually be the culprit. They go on to show that, for systems obeying $\rho/\sigma^3 \propto r^{-\gamma}$, there exists a critical case, $\gamma_{\rm crit} = 1.9\overline{4}$, for which the density profile is not truncated, or otherwise unrealistic.

This analysis was extended by Dehnen & Mclaughlin (2005) to spherical systems with $\rho/\sigma_r^3 \propto r^{-\gamma}$ and anisotropic velocity dispersion tensors[†]. There it was shown

[†]The assumption of a power-law radial phase-space density profile, ρ/σ_r^3, appears at least as

that the problem remains analytically tractable, and that the solutions are entirely analagous to the isotropic case, if and only if one makes the assumption that the logarithmic density slope $d\ln\rho/d\ln r$ and velocity anisotropy profile $\beta(r)$ are linearly related. Their analysis indicates that the critical slope of the phase-space density profile is modified from that derived by Austin et al (2005) by the *central* value of the velocity anisotropy: $\gamma_{\rm crit} = 1.9\overline{4} - 2\beta_0/9$. This result is somewhat gratifying because a roughly linear $d\ln\rho/d\ln r - \beta$ relation was already suggested by Hansen & Moore (2006) on entirely different grounds. It is worth mentioning, however, that the linearity of the $d\ln\rho/d\ln r - \beta$ relation appears robust in the halo inner regions only, and that there is a significant scatter from this relation at large radii (see Fig. 3.19). Dehnen & McLaughlin argue that this is not entirely unexpected; different amount of velocity anisotropy are required to stabilize different halo shapes, which results in some scatter in the $d\ln\rho/d\ln r - \beta$ for different halos.

Barnes et al (2006) examine the rich analytic content of the isotropic Jeans equation to investigate the origin of the power-law phase-space density profile. They show that mechanical equilibrium alone is an insufficient condition for producing power-law ρ/σ^3 distributions; systems with, for example, Hernquist or King-like density profiles *do not* exhibit power-law phase-space density profiles. Their analysis of the Jeans equation was extended in Barnes et al (2007) to include the effects of anisotropy in the velocity distribution. There it was shown that reproducing both the density and velocity anisotropy profiles of simulated halos *requires* a roughly linear relationship between the density slope $\gamma(r)$ and the velocity anisotropy $\beta(r)$, as observed by Hansen & Moore (2006) and suggested by Dehnen & McLaughlin (2005), but that such a relation is not a *requirement* for systems with power-law phase-space density profiles. In other words, the roughly linear $\beta-\gamma$ and power-law ρ/σ^3 relations appear to have distinct physical origins.

In Chapter 3 we studied the density, velocity dispersion, anisotropy, and pseudo-

empirically well motivated as the power-law behavious of the one dimensional phase-space density profile (see, e.g., Fig. 3.21).

phase-space density profiles of a set of six ultra-highly resolved CDM halos. Our analysis convincingly demonstrated that the density and velocity dispersion profiles of ΛCDM halos are *not* strictly self-similar: different halos cannot be simply rescaled to look alike. Intriguingly, the major differences in these profiles from halo-to-halo are minimized when analyzing the phase-space density profile suggesting, in a limited sense, a way in which dark matter halos can be considered "universal". More intriguing still is the fact that, even in these ultra high resolution simulations, the phase-space density profiles follow the $r^{-1.875}$ Bertschinger law over the entire resolved radial range.

State of the art numerical simulations of structure formation are now beginning to probe the distribution of dark matter robustly on scales of hundreds of parsecs, where observational constraints tend to be the strongest. Although baryonic processes inevitably alter the distribution of dark matter on sub-galactic scales, an understanding of the equilibrium structure of dark matter halos remains a theoretically appealing problem as it is intimately linked to the nature of dark matter, and is often required to aid in the interpretation of observational data sets.

In this Chapter we use a suite of cosmological N-body simulations of dark matter halo formation to study the connection between the resulting density and velocity dispersion profiles, and how these relate to the power-law phase-space density profile. We place particular emphasis on the *universality* of the profiles and speculate on possible mechanisms for generating the observed scatter in the global shapes of spherically averaged CDM density profiles.

The remainder of this Chapter is organized as follows. We briefly introduce our numerical experiments, halo sample, and analysis techniques in §2. In §4 we present our main findings: we begin by presenting the density and velocity dispersion profiles of our halo sample, followed by a discussion of how they relate to a universal phase-space density profile. We use the Jeans equation to interpret the small but significant deviations from a universal $\rho(r)$ profile and show that the ρ/σ^3 profile is

apparently more universal that $\rho(r)$. We end with a brief summary of our findings in § 4.4.

4.2 Numerical Experiments

The numerical techniques used in the present Chapter, including the production of initial conditions and numerical parameter optimization, have been described thoroughly in previous Chapters as well as elsewhere in the literature (see e.g. Power et al. 2003, P03; N04; Ludlow et al 2008). For the sake of completeness we here review the main numerical issues, but refer the reader to that work for a more complete discussion.

4.2.1 The Cosmological Model

Our simulations adopt a flat concordance ΛCDM cosmological model with $\Omega_0 = 1 - \Omega_\Lambda = 0.3$, and a present day Hubble constant of 73 km s^{-1} Mpc^{-1}. The power spectrum of matter fluctuations is normalized such that $\sigma_8 = 0.9$ is the current rms mass fluctuation within spheres of $8h^{-1}$Mpc radius. The linear power spectrum of density fluctuations is generated assuming a Harrison-Zel'dovich primordial power spectrum, $P(k) \propto k$, appropriately modified by the CDM transfer function (Bardeen et al 1986). These choices of parameters are consistent with those determined from the WMAP1 data (Spergel et al 2003) and the 2dF galaxy redshift survey (Colless et al 2001).

4.2.2 Numerical Methods

The simulations presented here follow the evolutionary histories of individual dark matter halos in their full cosmological context. Each halo was identified as a gravitationally bound friends-of-friends halo (FOF, Davis et al 1985) in a large-volume simulation and was subsequently resimulated at higher resolution using the methods

described in this thesis. The technique consists of resimulating the entire parent volume after replacing the particles that end up in the halo of interest (at z=0) with higher-resolution ones, and re-sampling the remainder of the simulation volume at lower resolution. Additional power is added to the region containing the high resolution particles up to the Nyquist frequency imposed by the particle spacing. Care is taken to ensure that the volume outside the high-resolution region retains sufficient structure to apply realistic tidal torques to the high-resolution particles.

Each simulation was run with the publicly available tree-SPH code `Gadget2` (Springel 2005), a massively parallel N-body code optimized for cosmological simulations. `Gadget2` computes the long-range gravitational forces between particles using a hierarchical tree algorithm, has adaptive timestepping for individual particles, and optionally supplements the force calculation using a particle mesh for intermediate-range forces. For the purpose of identifying FOF halos and their associated substructures we use SUBFIND (Springel et al 2001). The softening lengths for the high resolution particles are chosen according to the "optimal" prescription of Power et al. (2003), namely a spline lengthscale $h_s = 1.4\ \epsilon_{gdt} \approx 4\ r_{200}/\sqrt{N_{200}}$. Numerical details of the runs are given in Table 4.4.

4.2.3 Halo Sample and Analysis

We focus our analysis on the spherically-averaged density, velocity dispersion, and anisotropy profiles of each halo. We identify the halo center with the location of the particle having the minimum potential energy and compute each radial profile between $r_{\rm conv}$ and r_{200} in equally-spaced intervals in $\log r$. We define $r_{\rm conv}$ as the radius at which the relaxation time is equal to the age of the universe, where the enclosed mass profiles have been shown to converge (see §3.4.1 of Chapter 3).

We estimate the phase-space density profile using the proxy ρ/σ^3 which, by analogue, has the same units as the distribution function $f(\mathbf{x}, \mathbf{v}, t)$ of kinetic theory. Here $\rho(r)$ is the spherically averaged density profile; $\sigma^2/2 = \bar{v}^2/2$ is the specific

kinetic energy in a given radial shell. Velocity anisotropy is quantified by

$$\beta(r) = 1 - \frac{\sigma_\theta^2 + \sigma_\phi^2}{2\sigma_r^2}, \tag{4.4}$$

where $\sigma_{\rm tan}^2 = \sigma_\theta^2 + \sigma_\phi^2$ is the tangential velocity dispersion. With this parametrization $\beta = 0$ for isotropic systems, $0 < \beta \leq 1$ for radially biased systems, and $\beta < 0$ for tangentially anisotropic velocities.

One of the goals of this study is to quantify and explain the origin of the scatter in the shapes of the spherically averaged density profiles. As pointed out by Neto et al (2007) and Gao et al (2007), halo parameters derived by fitting empirical formulae (like eq. 4.1 and eq. 4.3) to the density profiles of simulated halos depends on the level to which the halo can be considered relaxed. Given the striking similarity in the density profiles over a wide range of masses it is important to draw conclusions from a sample of sufficiently relaxed systems, so as to minimize the possibility of introducing a subtle bias into the results. We follow Neto et al (2007) and measure for each halo, and at all times, three parameters which allow us to identify a sample of "relaxed" halos. These include the substructure mass fraction $M_{\rm sub}/M_{200}$, the offset between the center of mass of the systems and its minimum potential energy $d_{\rm off} = r_{\rm CM}/r_{200}$, and the virial ratio $U/2K$. Unless otherwise stated, each profile presented in the following sections correspond to the most recent output for which all three conditions $M_{\rm sub}/M_{200} \leq 0.07$, $d_{\rm off} \leq 0.05$, and $U/2K \leq 1.$ are satisfied.

The redshift zero properties of each halo in our sample are listed in Table 4.4. Here the virial mass (M_{200}) and particle number (N_{200}) refer to the quantities measured within the virial radius, r_{200}, defined as the distance from the halo center at which the mean interior density is equal to 200 times the critical density. $V_{\rm max}$ and $r_{\rm max}$ measure the magnitude and location of the peak circular velocity of the halo. Table 4.4 lists, in addition, some of the basic structural parameters of the halos at the most recent relaxed redshift, $z_{\rm rel}$. This includes the substructure mass fraction

($M_{\rm sub}$), the offset between the center of mass and the location of the minimum potential ($d_{\rm off}$), and the virial ratio. Note that the value of these parameters at $z = z_{\rm rel}$ typically exceed the standard for "relaxed" halos set in Neto et al (2007).

4.3 Results

4.3.1 The Structure of ΛCDM Halos

$\rho(r)$ and $\sigma(r)$ profiles

In Fig. 4.1 we plot the spherically averaged density (left) and velocity dispersion (right) profiles for all 15 relaxed halos in our sample. The radial coordinates have been normalized to r_{-2} and $r_\sigma = r(\sigma_{\rm max})$ respectively; densities to ρ_{-2} and velocity dispersions to $\sigma_{\rm max}$. The density profiles are plotted from the virial radius r_{200} down to the innermost converged radius $r^{(1)}_{\rm conv}$ (see § 3.4.1 of Chapter 3), a convention adopted in all subsequent plots, and have been weighted by a factor of r^2 in order to highlight the differences in profile shapes. The $\rho(r)$ and $\sigma(r)$ profiles are grouped according to their best-fit "α", determined by fitting the $\rho(r)$ profiles to eq. 4.3 over the radial range $r_{\rm conv} \leq r \leq r_{200}$. Halos with the most gradual turnover in density ($\alpha \leq 0.161$) are shown in blue (dashed), intermediate halos in green (solid), and those with the most rapid changing profiles ($\alpha \geq 0.187$) are shown in red (triple-dot-dashed). The thick black (solid) line in the left panel shows the NFW profile (eq. 4.1), which is fixed in these scaled units. Also plotted are the "average" Einasto profiles for each of the three colored samples,corresponding to $\alpha = 0.142$ (blue), 0.168 (green), and 0.196 (red).

Fig. 4.1 illustrates a number of interesting aspects of CDM halo structure. First, and in agreement with the results of Chapter 3, the overall shape of the density profiles appear to be well approximated by the 2-parameter profile proposed by NFW (solid black curve in left panel). These profiles deviate strongly from the simple

power-laws predicted by early analytic studies and steepen systematically from the inner to outer regions, having logarithmic slopes shallower than isothermal in the center, but steeper than isothermal near the virial radius. Like the density profiles, the velocity dispersion profiles of these halos have a distinctive shape: the velocity dispersion increases with radius to a well defined maximum before decreasing to the virial radius. More importantly, we find that the velocity dispersion profiles also tend to segregate with respect to the best-fit Einasto parameter, albeit with some scatter. This is reflected by a more gradual change in the radial behavior of $\sigma(r)$ in halos that have more gradually changing logarithmic density slopes. This confirms the conclusions drawn in Chapter 3, but here, with a larger sample size.

Also note that the density profiles exhibit small but significant deviations from the NFW profile and are more accurately modeled by the 3-parameter Einasto function. Given the differences in profile shape from halo to halo a 3-parameter function that allows for varying logarithmic slope is likely the simplest parametrization that one can hope for. We note that deviations from a universal $\rho(r)$ have been discussed previously by several groups (N04; Merritt et al 2005; Gao et al 2007), yet the *origin* of the deviations have not yet been discussed in any detail in the literature.

It is important to note that our present discussion of universality is not the same as that previously suggested by Jing & Suto (2000) (see also Ricotti 2003; Ricotti et al 2007). These authors find that the local density at the innermost converged radius increases systematically with halo mass and use this fact to argue against a universal density profile. However, as noted by Klypin (2001) and N04, this just reflects the well-established trend between halo mass and concentration, and does not signify departure from self-similarity. True deviations from self-similarity are seen as systematic differences in slope measured at fixed fractions of some *mass-independent* radius, such as r_{-2}, as seen in Fig. 4.1.

ρ/σ^3 profiles

In Fig. 4.2 we compile the phase-space density profiles for our sample of 15 halos (upper panels). The left and right panels show, respectively, the total PSD profile, $\rho/\sigma^3_{\rm tot}$, and its radial analogue, $\rho/\sigma^3_{\rm r}$. As before, each profile is grouped and colored according to its best-fit α. Also plotted is the theoretical result anticipated by Bertschinger (1985) for secondary infall onto a point mass perturber in an expanding background. This confirms the results of previous studies and demonstrates that the phase-space density profiles of dark matter halos are very well described by a universal power-law of slope -1.875. This is a remarkable feature of ΛCDM halos given that the radial density and velocity dispersion profiles are known to exhibit preferred scale lengths.

Another interesting feature, as discussed in Chapter 3, is how accurately the phase-space density profiles of the simulated halos can be described by Bertschinger's secondary infall solution, plotted as a thick dot-dashed line in Fig. 4.2. This solution corresponds to the stratification of entropy obtained by smooth and spherical accretion onto a point mass perturber in an Einstein-de Sitter universe. In these secondary infall models the radially collapsing mass shells settle into hydrostatic equilibrium with progressively larger entropies (lower densities in phase-space) ultimately leading to phase-space density profiles that diverge near the center.

This is an unexpected result since the halo formation process envisioned by Bertschinger is markedly different from that occurring in a fully cosmological scenario. In the latter, dark matter halos obtain most of their mass through the accretion of clumpy material which primarily occurs along filaments and in a highly aspherical manner. This is in stark contrast with the smooth, spherical accretion envisioned by secondary infall models. Indeed, the differences in analytical and simulated halos are seen clearly in their density and velocity dispersion profiles; spherical infall models produce power-law density and velocity dispersion profiles, whereas simulated halos have corresponding profiles with smoothly changing slopes.

The radial phase-space density profiles (shown in the right-hand panel of Fig. 4.2) appear to prefer a slightly steeper power-law than $r^{-1.875}$, as indicated by the small but systematic deviations from Bertschinger's solution within the halo scale radius, r_{-2}. We do note, however, that these deviations are small, less than ∼25% for all $r < r_{-2}$. This is in agreement with the work of Knollmann et al (2008) (among others), who find that the radial phase-space density profiles of a large sample of cosmologically simulated halos are described by power-laws with slopes > 1.875, and is expected for systems whose velocity distributions become increasingly biased to radial motions with increasing radius.

This is certainly in agreement with the analytic results of Dehnen & McLaughlin (2005) and Barnes et al (2007), who use the anisotropic Jeans equation to place constraints on the slope of the radial phase-space density profile. These Authors independently derive a critical value, $\gamma_{\rm crit} = 1.9\overline{4} - 2\beta_0/9$, for the slope of ρ/σ_r^3 that produces density profiles which asymptote to realistic power-laws at large and small radii. Under the plausible (though untested) assumption that $\beta \rightarrow 0$ as $r \rightarrow 0$, the critical slope of the radial phase-space density profile would thus be $\gamma_{\rm crit} = 1.9\overline{4} = 35/18$, which is roughly consistent with the mean slope and its associated $1-\sigma$ scatter (1.96 ± 0.1) derived for the halos presented here.

Another intriguing result is that the ρ/σ^3 profiles are "universal", in the sense that they are independent of the Einasto parameter, α, which dictates the radial behavior of $\rho(r)$ and $\sigma(r)$. This suggests that the $\rho - \sigma$ coupling alluded to in Fig. 4.1 occurs so that the phase-space density profiles stratify radially to a well-defined power-law, $r^{-1.875}$, independent of the physics governing the variations in α. But what determines α?

4.3.2 Dark Matter Halos and the Jeans Equation

The equilibrium structure of self-gravitating collisionless objects is described by the Jeans equation:

$$V_c^2 = -\sigma_r^2 \left[\frac{d\ln\rho}{d\ln r} + \frac{d\ln\sigma_r^2}{d\ln r} + 2\beta \right]. \tag{4.5}$$

Here $V_c^2 = GM/r$ is the circular speed at radius r, $\rho(r)$ is the density, $\sigma_r(r)$ the radial velocity dispersion, and $\beta(r)$ the anisotropy profile. In order to solve this equation one must make strong assumptions regarding the relationship between the density profile and the components of the velocity dispersion tensor. One common assumption is that the phase-space density profile follows a power-law, $\rho/\sigma^3 \sim r^{-\gamma}$. Knowledge of either $\rho(r)$ or $\beta(r)$ is then sufficient to close the Jeans equation and determine the other.

Assuming that $\rho/\sigma^3 \propto r^{-\gamma}$ the shape of the $\sigma(r)$ profile can be determined for a given radial density profile. For the Einasto profile we have

$$\frac{\mathrm{d}\ln\sigma^2}{\mathrm{d}\ln r} = \frac{2\gamma}{3}\left(1 - \left(\frac{r}{r_\sigma}\right)^\alpha\right), \tag{4.6}$$

where $r_\sigma = r(\sigma_{\rm max})$ is the radius where the velocity dispersion profile peaks: $r_\sigma = r_{-2}(\gamma/2)^{1/\alpha}$. The shape of the velocity dispersion profiles are accurately described by eq. 4.6, as can be seen by the small residuals in the lower-right panel of Fig. 4.1. It is worth mentioning that the quality of the fits of eq. 4.6 to the simulated $\sigma(r)$ profiles is comparable to the quality of fits of eq. 4.3 to the density profiles (provided α is allowed to vary at fixed γ, see Fig. 4.1), neither of which show any systematic trend in the residuals.

To further illustrate the visual trends in Fig. 4.1 we have fit each velocity dispersion profile to eq. 4.6, allowing $\alpha = \alpha_\sigma$ and r_σ to vary at fixed γ. This allows us to compare directly two independent estimates of the Einasto parameter α (which, in Fig. 4.3, we call α_σ and α_ρ, depending on the profile fitted) as well as the relationship between r_σ and r_{-2}, and to compare these directly with the anticipated

trends for Bertschinger's law. The results of this exercise are presented in Fig. 4.3. The clustering of α_ρ and α_σ around the 1:1 line shows the connection between the global shape of the density and velocity dispersion profiles.

Given that the radial phase-space density profiles appear to follow a universal power-law we can use eq.'s 4.3 and 4.6 to write the spherically symmetric Jeans equation (eq. 4.5) as

$$\frac{V_c^2}{\sigma_r^2} + 2\beta(r) = \frac{\gamma}{3}\left(5\left(\frac{r}{r_\sigma}\right)^\alpha - 2\right). \tag{4.7}$$

This implies that the Einasto parameter α is related to the behavior of the quantity $\psi(r) = V_c^2/\sigma_r^2 + 2\beta$. Here $\kappa_r(r) = V_c^2/\sigma_r^2$ measures the ratio between the specific kinetic energy in radial motion to the circular speed at a given radius, and $\beta(r)$ is the anisotropy parameter (eq. 4.4). Thus, the slight deviations from universality evident in Fig. 4.1 appear to be modulated by differences in the radial behavior of $\psi(r)$, either through $\kappa_{\rm r}(r)$ or $\beta(r)$. Furthermore, if the ratio ρ/σ_r^3 is a universal power-law for all CDM halos then $\psi(r_\sigma) = \gamma$ is a universal characteristic of CDM halo structure.

For a spherically symmetric and isolated system we can use eq. 4.7 to obtain the anisotropy profile for a given $\rho(r)$. The Einasto profile yields

$$\begin{aligned}\beta(x) = \frac{5}{3}x^\alpha - \frac{\gamma_r}{3} - \eta_{-2}2^{-(3+\alpha)/\alpha}e^{2/\alpha}\alpha^{3/\alpha-1}\Gamma\left(\frac{3}{\alpha}\right) \\ \times\, e^{-4(x^\alpha-1)/(3\alpha)}x^{-(2\gamma_r/3+1)}\Gamma\left(\frac{3}{\alpha};\frac{2x^\alpha}{\alpha}\right),\end{aligned} \tag{4.8}$$

where $x = r/r_{-2}$, $\eta_{-2} = 4\pi G r_{-2}^2\rho_{-2}/\sigma_{-2}^2$, and $\Gamma(a;x)$ is the incomplete Gamma function. As discussed by Zait et al (2007), eq. 4.8 may aid in more detailed mass modeling of galaxy clusters from kinematic data, which has typically been limited to the assumption of constant velocity anisotropy (Lokas et al 2006; Wojtak & Lokas 2007).

Clues to what sets the Einasto parameter may be gleaned from Fig. 4.4, where

we plot the $\kappa_r(r)$ (top) and $\beta(r)$ (bottom) profiles for our halo ensemble. As in previous plots the profiles have been grouped and colored according the best-fit value of α. The $\kappa_r(r)$ profiles appear distinct when grouped by α. In contrast, the $\beta(r)$ profiles appear to be independent of the value of α, implying that the global shape of the density profile of a given halo is determined by the radial dependence of $\kappa_r = V_c^2/\sigma_r^2$, and is less affected by anisotropies in the velocity distribution.

This is reminiscent of the work of T&N who derived density profiles for spherically symmetric and isotropic systems constrained to follow power-law ρ/σ^3 distributions. These authors show that the shape of the resulting density profile is characterized by two parameters: the slope γ of the phase-space density profile, and the value of the parameter $\kappa = V_{\rm max}^2/\sigma^2(r_{\rm max})$. Assuming that γ is a universal constant for all halos this leaves one free parameter, κ_r, which governs the over-all shape of the density profile.

In Fig. 4.5 we plot the $\psi(r)$ profiles (thin lines) together with the predictions of the Jeans equation (heavy lines). Radii have been normalized to r_{200}. As anticipated by eq. 4.7 the profiles intersect at $\psi(r_\sigma) = \gamma \approx 1.875$, which reinforces the utility of the power-law description of the dark matter halo phase-space density profile. Moreover, the shape of $\psi(r)$ agrees with the Jeans equation for power-law phase-space density profiles, as seen by the segregation with respect to α.

4.3.3 Understanding Non-universality

Clues to the origin of the systematic deviations in the shapes of dark matter halo density profiles can be gleaned from Fig 4.6 a), where we show the relationship between halo concentration (defined as r_{200}/r_{-2}) and the Einasto parameter α. As mentioned, the concentration parameter measures (the inverse of) the halo scale radius, r_{-2}, in units of r_{200}, and depends strongly on the formation time of the halo. Halos that collapse earlier are, on average, more concentrated than their later forming counterparts (Neto et al 2007, Gao et al 2007, Bullock et al 2001). Since in

a hierarchical universe small objects typically collapse first this introduces a (well studied) mass−concentration relationship in which low-mass, early collapsing halos are systematically more concentrated than massive objects, reflecting the higher cosmic density at their earlier formation epoch.

We find evidence for a weak correlation between concentration and α, indicating that halos with higher concentrations have systematically steeper density profiles (i.e. lower value of α) than less concentrated halos. It appears that the halo formation epoch imprints itself, not only on the characteristic scales of the density profile (r_{-2}, ρ_{-2}), but also on its shape parameter α. This is in qualitative agreement with the recent results of Gao et al (2007), who analyze halos in the millennium simulation and find that α is an increasing function of halo mass.

Given the $c - \alpha$ relationship above we can begin to speculate about the origin of the non-universal shapes of relaxed density profiles. Qualitatively speaking, the empirical relationship between halo concentration and formation time indicates that early collapsing objects accrete larger fractions of their $z = 0$ mass at higher redshifts than those which form later. This implies that the initial accretion rate onto primordial perturbations is accelerated for objects with earlier formation times. In order to achieve a more rapid accretion rate, the host must originate from an initial linear overdensity which exceeds that of an object collapsing later. The enhanced overdensity of these primordial perturbations provides the excess gravitational pull that is required to halt the expansion of nearby mass shells, causing them to turn around and to accrete at earlier times, and from more localized volumes.

This is shown explicitly in Fig. 4.7, where we plot the mass accretion histories (MAH) for each halo, $M_{200}(z)/M_{200}(0)$. Line colors segregate profiles according to α, as before. The strong segregation of the MAHs by Einasto parameter at early times (between $z \approx 9$ and $z \approx 3$) indicate that the mass accretion rates differ markedly in the early stages of halo growth. For example, the median redshift at which the $< \alpha >= 0.142$ sample reaches 1% of its final virial mass is ~ 9, compared to ~ 5 for

the $< \alpha >= 0.196$ sample. The corresponding redshifts at which $M(z)/M_{200} \approx 0.05$ are $z \approx 5$ and $z \approx 3$ respectively. We note that the segregation of the median MAH for the high (red) and low (blue) α samples persists to $z \approx 1$, but there is a large amount of scatter (induced by the increased merger activity) at all times subsequent to $z \approx 3$.

The differences in the accretion rates at early times are also evident in the evolution of Lagrangian radii containing fixed fractions of the $z = 0$ virial mass. In Fig. 4.7 b) we plot the evolution of the (Lagrangian) radius encompassing the inner 5% of the $z = 0$ halo mass profile. As expected, the more concentrated systems, with steeper density profiles, accrete a given fraction of their $z = 0$ mass at earlier times, and from more localized volumes.

The overall trends described above are perhaps best understood by considering the distribution of kinetic and potential energy across the linear perturbation leading to the collapse and formation of each halo. Here we define the kinetic energy, $T_r(M) = v_{\rm rad}^2/2$, as that contained in the outward expansion of a given mass shell; the potential energy, $\Phi(M) = GM(< r)/r$, is that of all mass interior to a given shell. We plot the ratio, $T_r(M)/\Phi(M)$ versus enclosed mass in Fig. 4.8. In each case, the total enclosed mass has been normalized by the present day virial mass of each halo.

The results shown in Fig. 4.4 indicate that α appears to modulate the radial dependence of the quantity $\kappa_r = V_c^2/\sigma_r^2$, suggesting that α reflects, *at the present day*, how the kinetic support varies as a function of enclosed mass *across the system*. In Fig. 4.8 we see that the same it true when referring to the initial overdensity field. Halos collapsing early have, in general, less kinetic support for a given enclosed mass than those collapsing later. Thus, early collapsing halos form virialized objects with κ profiles that are distinct from those collapsing later. Hence, subtle differences in the $z = 0$ structure of dark matter halos appears to be dependent on processes occurring in the very early universe.

Consider, for example, two spherical linear overdensities, both having the same total mass, but different initial distributions of kinetic support across the fluctuation (i.e. different initial virial ratios). For the purposes of this illustration, we can assume (as in van Albada 1982) that the initial conditions are obtained by disturbing particles from an initially homogeneous sphere along the gradient of a Gaussian random field, $\psi(\mathbf{x})$. Initial velocities of the particles are given by $\nabla\psi/t_{ff}$, where t_{ff} is the free-fall time of the original sphere. The idea being that these particles have decoupled from the Hubble flow and are just now turning around and begining to accrete.

Allowed to evolve in isolation, these overdensities will collapse under their self-gravity to a compact configuration in a timescale $\sim t_{ff}$, and then partially re-expand. After several free-fall times, the inner regions of the objects approach a steady state, and the oscillations in the mass profiles are pushed to progressively larger radii. The smaller the initial virial ratio of the system (i.e. the less initial kinetic support for a given enclosed mass) the more pronounced the initial collapse and the higher the central density of the final relaxed object. Similarly, halos with more pronounced the initial collapse tend to perturb more mass onto large apocenter orbits, thereby increasing the density in the outer regions of the halo as well. The final density profiles of relaxed halos forming from the spherical collapse of an initially cold overdensity thus reflect the initial virial ratio of the system in a way that is qualitatively consistent with the results presented here. We caution, however, that the comparison with fully cosmological simulations is not direct, and should be taken with a grain of salt.

4.4 Discussion and Summary

The results presented in this Chapter have interesting implications for models attempting to describe the formation and structural evolution of dark matter halos

from the cosmological parameters and power spectrum alone. We have established that the global shape of the density profile of relaxed objects formed by hierarchical clustering (characterized by their logarithmic density slopes $\mathrm{d}\ln\rho/\mathrm{d}\ln r$) do not follow a universal form, as originally suggested by NFW. Rather, the density profiles of individual halos seem to reflect the details of their mass accretion histories. The picture supported by these results is one in which early collapsing, low-mass objects are systematically more concentrated, have less kinetic support (for a given enclosed mass), and consequently steeper density profiles than their later collapsing counterparts. This heralds the need for improved semi-analytic models aimed at developing a deeper grasp of the internal structure of dark matter halos and the factors that govern their evolution. Extensions of simple analytical models, such as those proposed by NFW, Eke et al (1996) and Bullock et al (2001b) are clearly required in order to explain these new details of CDM halo structure.

Our findings also indicate that the structure of ΛCDM halos may be considered "universal" when cast in terms of the phase-space density profile. The systematic differences in the spherically averaged density profiles induced by the various formation histories of dark matter halos are reflected in their velocity dispersion profiles (see Fig. 4.1) in a way that preserves a unique power-law ρ/σ_r^3. This provides a novel way of viewing the structure of CDM halos that form in ΛCDM cosmogonies which may help improve upon current Jeans inspired methods of modeling the structure and dynamics of relaxed systems.

We emphasize that deviations from universality in $\rho(r)$ are small and that the density profiles for relaxed halos can generally be fit by an NFW profile to better than $\sim$20% at all radii. The need for an improved fitting formula, such as the Einasto profile, comes from the fact that the comparison between typical simulated profiles and NFW fits show clear radially-dependent residuals. Thus, extrapolating these fits to radii where they have not been tested numerically, or show strong systematic deviations (as is often done in simplistic modeling techniques) is likely to

incur substantial error. Use of a 3-parameter function, such as eq. 4.3, substantially reduces the errors between the simulations and model fits and offers a method of quantifying the variation in the shape of the density profiles. For modeling purposes, it is important to employ fitting formulae that most accurately describe the anticipated structure of the systems being modeled.

Our results are consistent with the recent work of Gao et al (2007). These authors exploit the unprecedented number of halos in the very large millennium simulation (Springel et al, 2005) and show that both the concentration and Einasto parameter, α, of a halo ensemble correlates weakly with mass. In this paper we have shown that the Einasto parameter is actually set by the Jeans equation (eq. 4.7) for systems that obey power-law phase-space density profiles. Strictly speaking, it the the combination of V_c^2/σ_r^2 and anisotropy β that fixes α (see, also, Barnes et al 2005, 2007), but given the large scatter in anisotropy profile shapes, and the lack of evidence for a correlation between β and α, we have suggested that it is former quantity that most strongly affects α. This led us to speculate that the logarithmic slope of the density profile may actually hold clues about the formation histories of individual halos, which is exemplified by the relationship between concentration and α (Fig. 4.6). We base this speculation on the strong correlation between halo formation time and concentration (Neto et al (2007)), but plan to address the details of this issue in future work.

Finally, it is worth mentioning a recent study by Bellovary et al (2008), who use idealized spherical collapse simulations to investigate the role of the radial orbit instability (ROI) in molding the structure relaxed dark matter halos. These authors find that the quantity V_c^2/σ^2 acts to modulate the effects of the ROI; regions of a halo where $V_c^2/\sigma^2 \gtrsim 1$ are unstable and rapidly become triaxial due the instability. This is an intriguing result in light of the recent work of Barnes et al (2005), who have suggested that the density structure of dark matter halos may be regulated by the onset of the ROI. In this thesis we have shown that the global shape of the

density profile (parametrized by the Einasto parameter, α) appears to modulate the radial dependence of the quantity V_c^2/σ^2. It is thus possible, as suggested by Barnes et al (2005), that some aspect of the radial orbit instability occuring during the initial collapse phase is responsible for the scatter observed in the radial density profiles of relaxed dark matter halos. We plan to address this conection in future work.

We emphasize that the physics governing the correlations between concentration and formation time, as well as the correlations presented in Fig.4.6, is not yet understood; these correlations are, to a large, extent, only empirical. We plan to address the origin of these correlations in future work.

A brief summary of our results are as follows.

- The density profiles of CDM halos are *not* strictly universal, but rather show halo-to-halo variation in their logarithmic slopes measured at various *mass independent* radii. We find that the radial trend in density is more accurately described by the Einasto profile (eq. 4.3), first applied to CDM halos by N04.

- The velocity dispersion profiles of dark matter halos have a characteristic shape: $\sigma(r)$ rises from the center outward before dropping again near r_{200}. Assuming that the phase-space density profile follows a power-law the shape of the $\sigma(r)$ profiles and the radius of the maximum ($r_\sigma = (\gamma/2)^{1/\alpha} r_{-2}$) can be calculated, and is shown to be in agreement with the results of our simulations (see Fig. 4.1 and 4.3).

- The phase-space density profiles, ρ/σ^3 and ρ/σ_r^3, appear to be "universal" insofar as they are independent of concentration and the Einasto parameter, α, describing a given halo. This suggests that the most fundamental aspect of dark matter halo structure is its radial stratification of entropy. This represents a strong new constraint on the structure of dark matter halos and could provide improved methods of modeling observational data.

- The phase-space density profiles closely follow a power-law with slope -1.875, in agreement with the spherical infall models of Bertschinger (1985).

- Systematic differences in the curvature of the density profiles of relaxed CDM halos appear to be related to the distribution of kinetic support across the system; halos with larger $\kappa_r = V_c^2/\sigma_r^2$ have systematically broader (less curved) density profiles than those with lower κ_r. We speculate that the origin of these deviations is related to the details by which individual halos accrete mass, and this is supported by the fact that more concentrated halos typically have steeper density profiles.

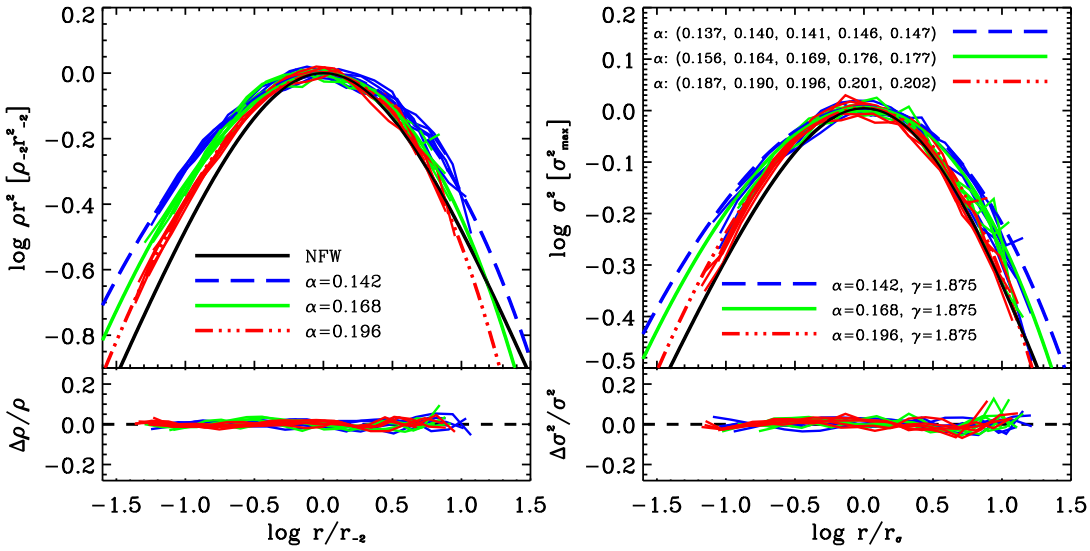

Figure 4.1: Spherically averaged density (left) and velocity dispersion profiles (right) for all halos in our sample. In order to highlight deviations from "universality" we have grouped the profiles according to their best-fit α's (eq. 4.3) and have weighted them by a factor of r^2. Radial coordinates are normalized to r_{-2} and densities to ρ_{-2}. The solid black curve shows the NFW profile (eq. 4.1), and the remaining curves correspond to the "average" Einasto profiles for each of the colored groups. The velocity dispersion profiles are also grouped and colored according to the Einasto parameter α. The curves in the upper-right panel show the averaged velocity dispersion profiles corresponding to a power-law phase-space density profile and the $\rho-$profiles shown on the right. The lower panels show the residuals to the best-fit Einasto profiles (left) and eq. 4.6 (right).

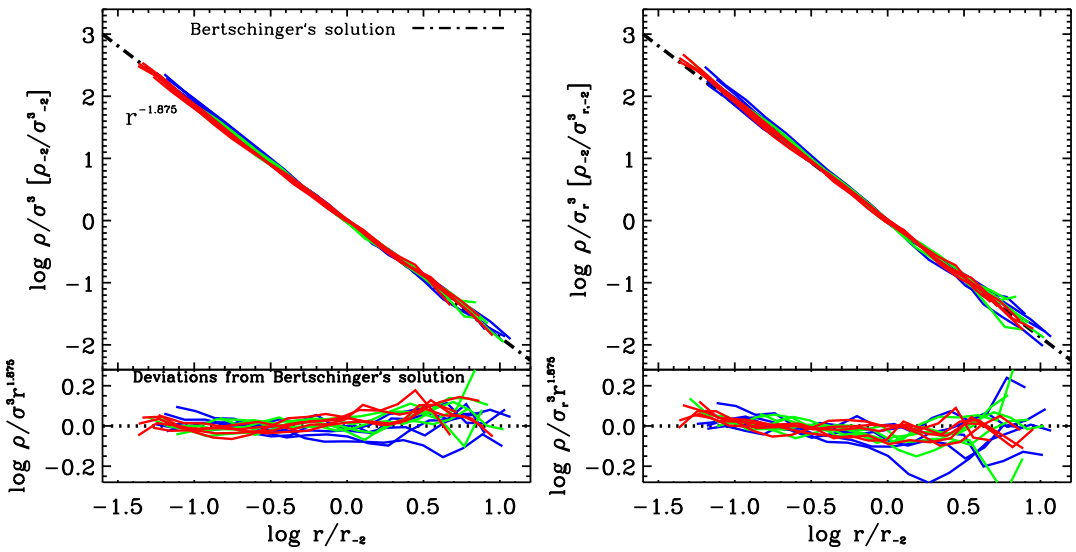

Figure 4.2: The total (left) and radial (right) phase-space density profiles for all dynamically relaxed halos. The radii coordinates have been scaled to r_{-2}, the radius where the logarithmic slope of the density profile is equal to -2, and both ratios $\rho/\sigma^3_{\rm tot}$ and $\rho/\sigma^3_{\rm r}$ have been normalized by their respective values at r_{-2}. The single power-laws (dot-dashed line) in each panel are not fits to the data but rather show the theoretically anticipated result of Bertschinger and have a slope of -1.875. The bottom panels show the rms deviations from Bertschinger's solution which are vertically normalized to be minimized within the halo scale radius, r_{-2}. Although the radial phase-space density profiles appear to be slightly but systematically steeper than Bertschinger's solution at this resolution, the absolute deviations are still quite small ($\lesssim 10\%$).

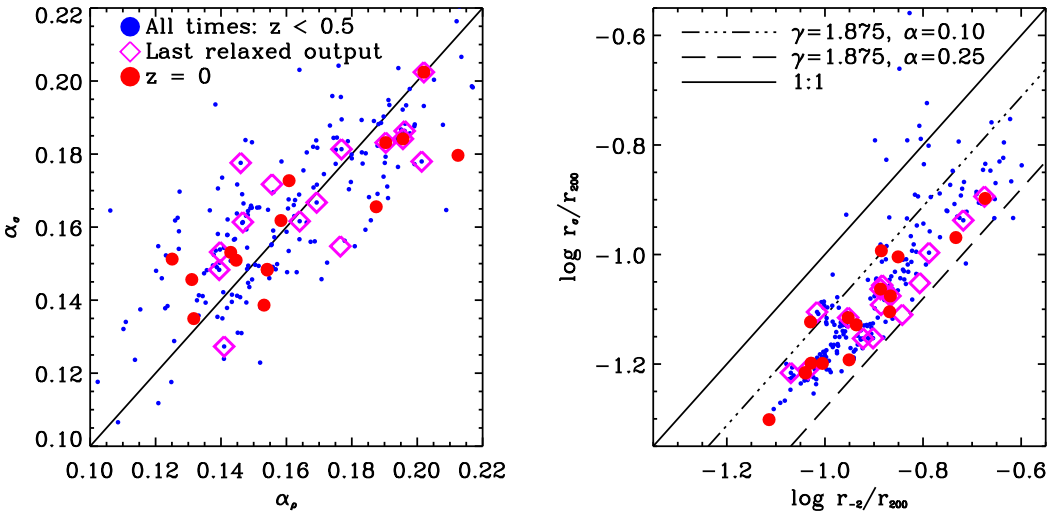

Figure 4.3: (Left panel) The best-fit "shape" parameters, α_ρ and α_σ, derived from eq. 4.3 and eq. 4.6 (the latter for $\gamma = 1.875$ kept fixed). The heavy squares correspond to the last relaxed output, and the small points to all outputs since $z = 0.5$. Note the scatter of the data points about the $1:1$ line, which shows the anticipated relationship between the shape parameters for Bertschinger's law. (Right panel) The relationship between the scale radii r_σ and r_{-2}. The dashed and triple-dot-dashed lines show the expected relationship for halos with fixed $\gamma = 1.875$ but with α ranging from 0.1 to 0.25; the typical values for the simulated halos studies here.

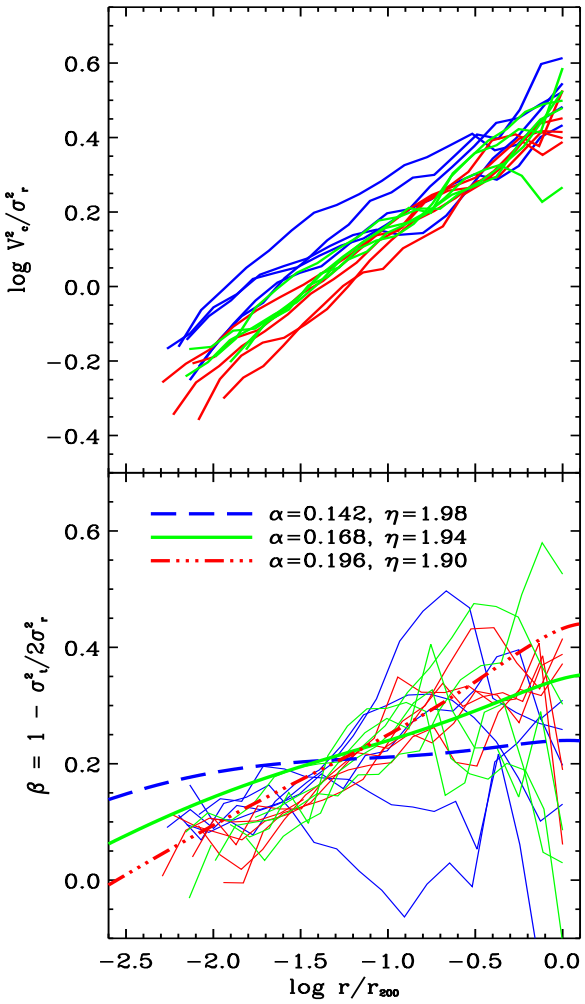

Figure 4.4: Ratio $\kappa_r = V_c^2/\sigma_r^2$ (top) and $\beta(r)$ (bottom) as a function of radius for our halo ensemble. As before, each profile is colored according to its best fit "α" from the Einasto profile. κ_r measures the ratio of gravitating mass within radius r, $GM(r)/r$, and σ^2 the local kinetic energy; β is the (local) anisotropy in velocities defined by eq. 4.4. The global shape of the density profile, characterized by its Einasto parameter, α, appears to be modulated by the gradient of κ_r, and is less effected by anisotropies in the velocity distribution.

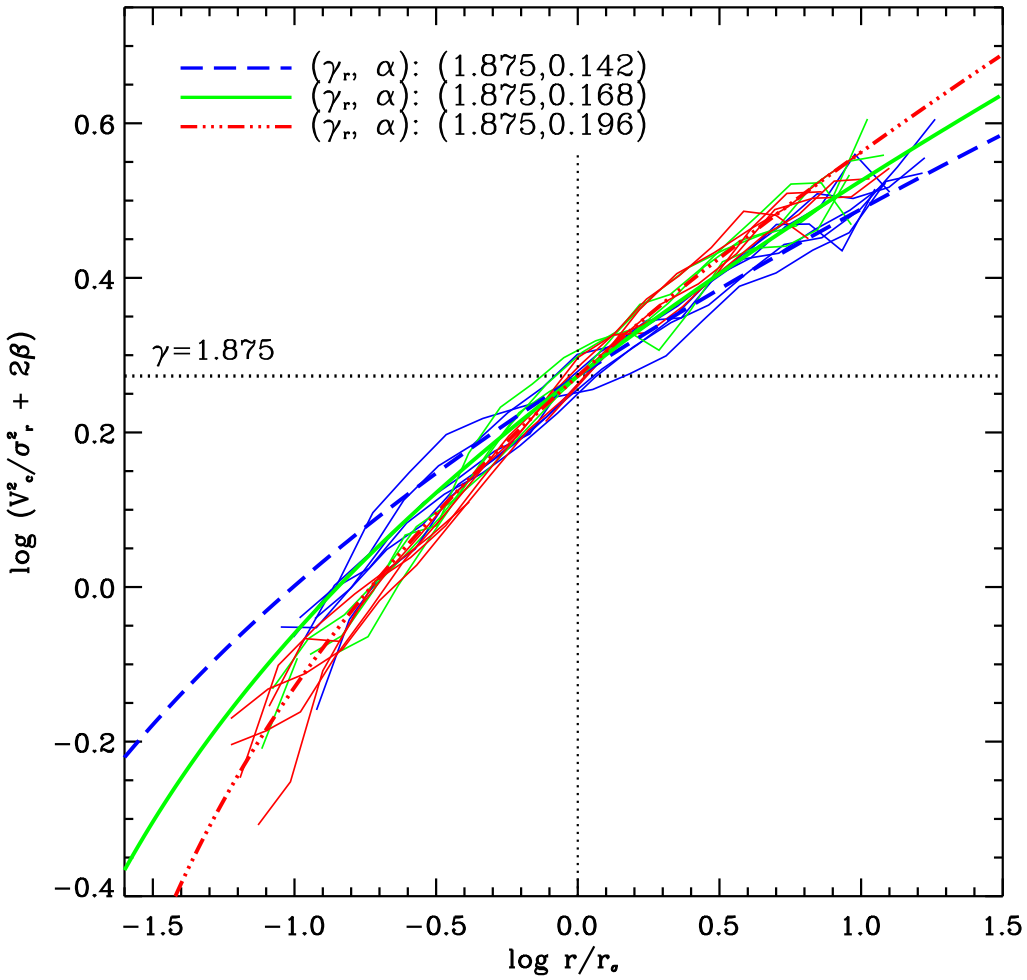

Figure 4.5: Radial dependence of the Jeans equation $\psi(r) = V_c^2/\sigma_r^2 + 2\beta$ for our halo sample. As before, each profile is grouped by the Einasto parameter α determined from fits to eq. 4.3, and the averaged analytic results are shown as heavy lines of the same style. Each profile has been normalized to the radius, r_σ, where the velocity dispersion profile peaks. For a universal phase-space density profile all profiles are expected to cross at $\psi(r_\sigma) = \gamma$.

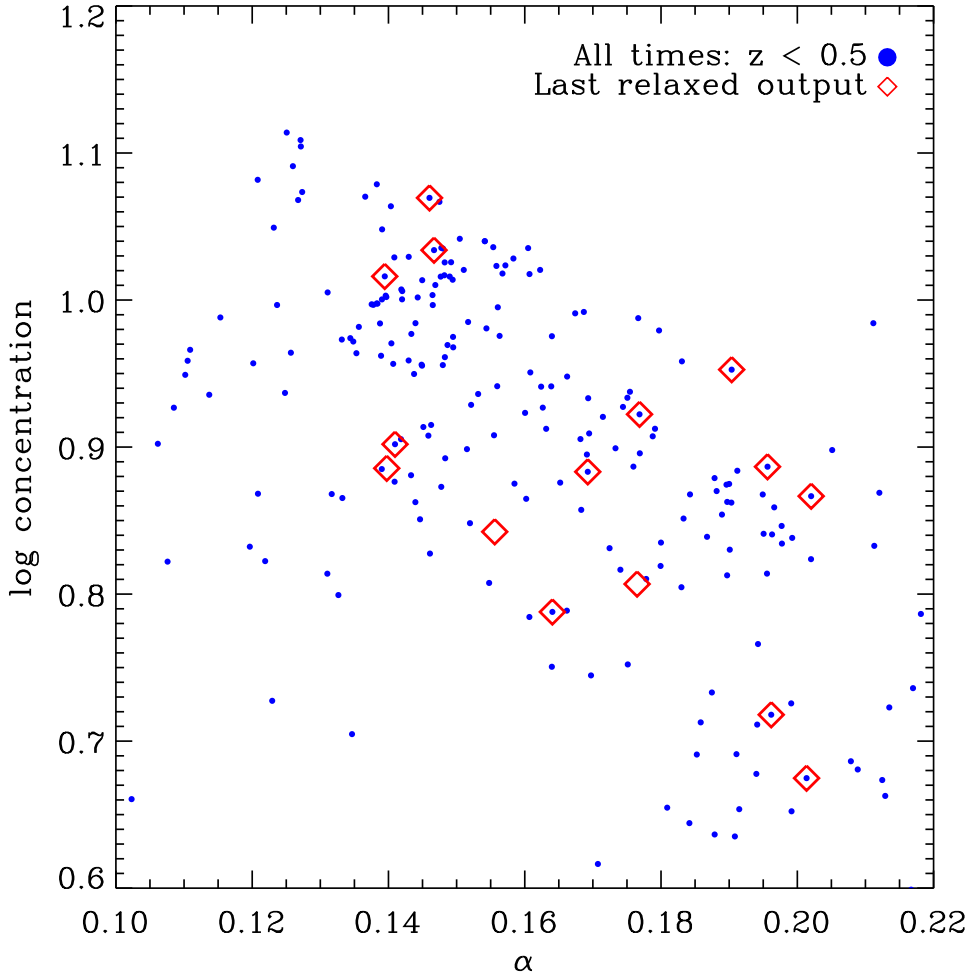

Figure 4.6: Relationship between the concentration, $c = r_{200}/r_{-2}$, and the Einasto parameter α describing halos in our sample. In each panel we use heavy squares (red) to denote the last relaxed output and smaller points (blue) for all outputs since z=0.5. Both parameters are derived from fits to the eq. 4.3 over the radial range $r_{\rm conv} \leq r \leq r_{200}$. The correlation between these structural parameters indicate that the formation time of a given halo affects not only the characteristic scales of the density profile, ρ_{-2} and r_{-2}, but also its shape.

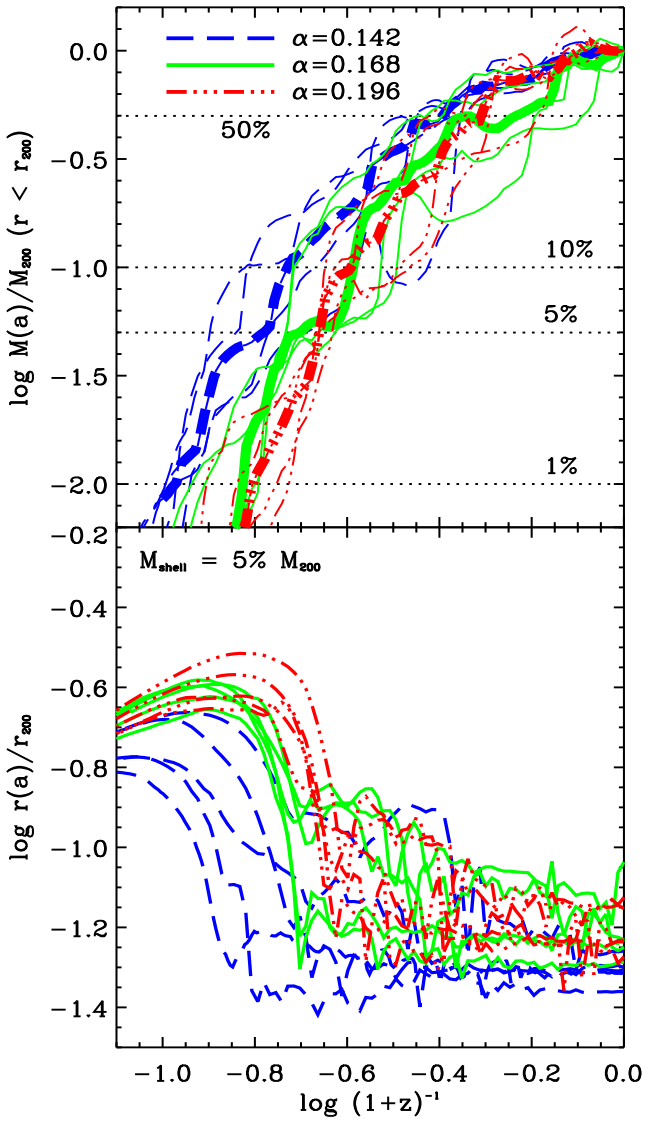

Figure 4.7: (Top panel) Mass accretion histories, defined as the virial mass, $M_{200}(z)/M_{200}(0)$, of the most massive progenitor halo in units of the present-day virial mass. (Bottom panel) Evolution of the Lagrangian radius containing the inner 5% of $M_{200}(0)$ as a function of cosmic expansion factor, a. Line styles and colors delineate curves according to the Einasto parameter describing the spherically averaged density profiles at the most recent relaxed output.

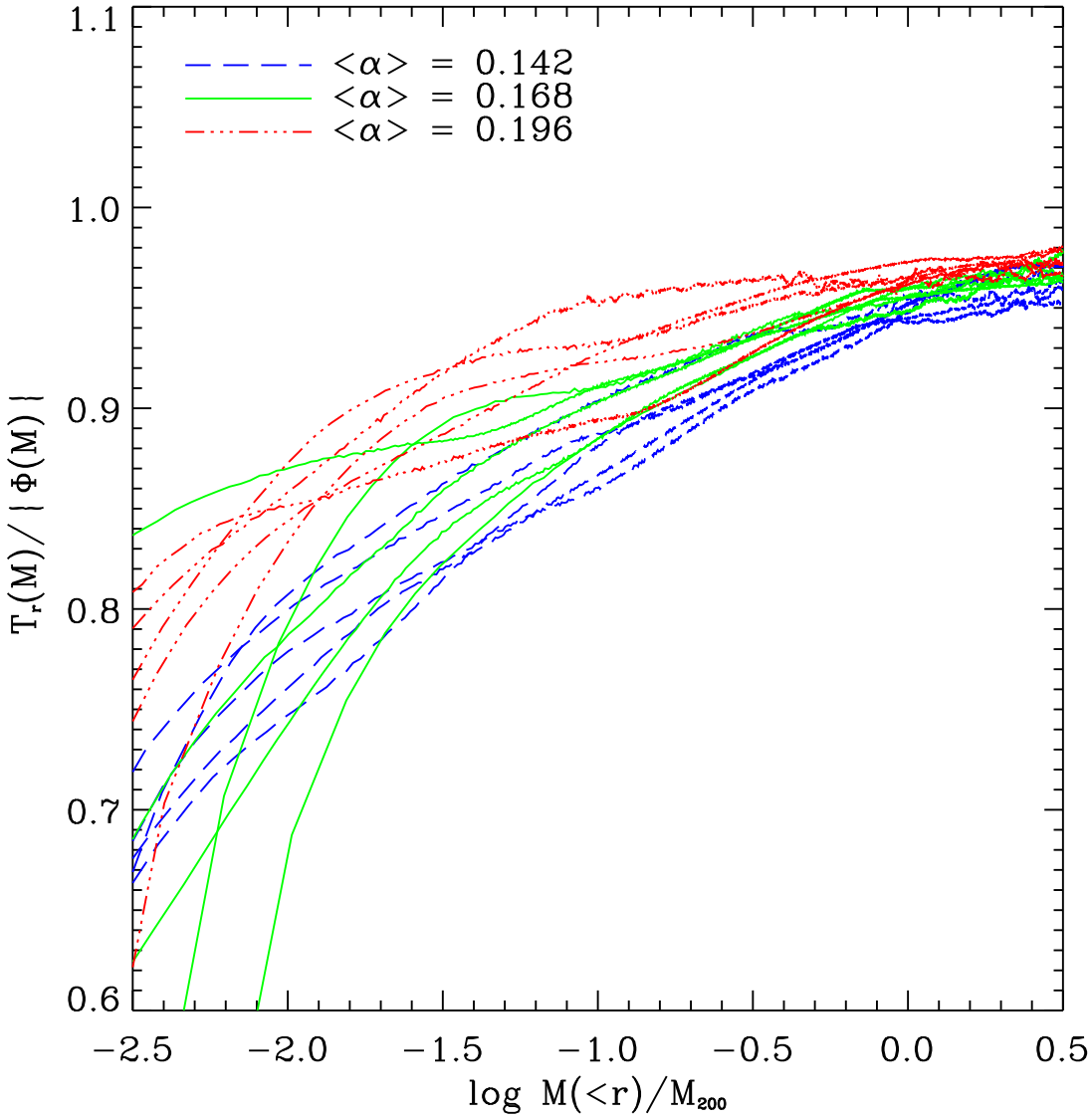

Figure 4.8: Ratio of kinetic energy in radial motion ($v_{\rm rad}^2/2$) to gravitational potential energy ($GM(<r)/r$) in linear overdensity field centered on primary overdensity plotted as a function of enclosed mass. Line colors and styles have the same meaning as in all previous plots. This shows that fluctuations with less kinetic support for a given enclosed mass collapse and virialize to form halos with less curved density profiles and higher V_c^2/σ_r^2 ratios.

Halo	ϵ_p [kpc/h]	M_{200} [$M_\odot/h$]	r_{200} [kpc/h]	$V_{\max}$ [km/s]	$r_{\max}$ [kpc/h]	$r_{\rm conv}$ [kpc/h]	N_{200} [10^6]
9-13-74	0.31	86.1	154.7	174.4	30.3	0.006	4.11
9-1-53	0.35	92.2	158.3	183.6	37.4	0.006	3.26
9-23-84	0.39	56.4	134.4	150.4	44.0	0.008	1.99
C02-400	0.33	144.1	183.7	209.3	21.3	0.005	5.02
9-14-56	0.38	85.0	154.1	179.2	33.7	0.007	2.59
9-14-49	0.26	91.7	158.0	171.6	47.3	0.005	5.91
9-22-4	1.61	1445.2	396.1	421.3	86.9	0.011	0.97
9-26-1	1.39	1389.5	391.0	424.6	114.2	0.010	1.26
9-2-20	1.06	486.4	275.5	272.0	188.2	0.012	1.09
9-14-39	0.39	125.9	175.6	202.9	39.1	0.007	3.30
9-62-1	2.08	14581.8	856.0	882.8	263.6	0.008	2.70
9-4-70	0.24	88.5	156.1	173.9	32.0	0.005	6.63
9-2-48	0.45	130.8	177.8	198.5	45.1	0.008	2.54
9-15-1	3.65	21993.1	981.6	1 043.0	444.8	0.012	1.16
9-12-46	0.25	70.3	144.6	159.4	35.1	0.006	5.26

Table 4.1: Here we provide, for each halo in our sample, a name, the Plummer-equivalent gravitational softening, virial mass and radii (M_{200} and r_{200} respectively). The structural parameters $V_{\max}$ and $r_{\max}$ measure the magnutide and location of the peaks of the circular velocity curve for each halo, $r_{\rm conv}$ is the Power et al (2003) convergence radius, and finally, N_{200} is the total number of particles within the halo virial radius, r_{200}.

Halo	z_{rel}	α_ρ	α_σ	κ_r $r < r_\sigma$	c	r_{-2} [kpc/h]	r_σ [kpc/h]	M_{sub} M_{200}	r_{CM} r_{200}	Virial
9-13-74	0.876	0.137	0.151	1.578	7.68	12.94	8.05	0.063	0.050	0.906
9-1-53	0.062	0.140	0.148	1.947	10.38	15.10	12.30	0.058	0.019	0.931
9-23-84	0.198	0.141	0.127	1.663	7.98	15.71	8.82	0.049	0.035	0.967
C02-400	0.350	0.146	0.178	1.547	11.74	13.71	9.79	0.063	0.027	0.914
9-14-56	0.049	0.147	0.161	1.518	10.81	13.87	9.27	0.036	0.024	0.925
9-14-49	0.821	0.156	0.172	1.497	6.96	13.34	7.21	0.060	0.026	1.000
9-22-4	0.140	0.164	0.162	1.543	6.14	58.50	36.12	0.043	0.031	0.893
9-26-1	0.140	0.169	0.167	1.577	7.64	47.59	31.95	0.040	0.031	0.874
9-2-20	0.309	0.176	0.155	1.532	6.41	30.01	17.06	0.047	0.023	0.944
9-14-39	0.350	0.177	0.181	1.426	8.36	18.29	10.75	0.047	0.014	0.957
9-62-1	0.030	0.187	0.166	1.502	5.22	161.50	97.40	0.058	0.011	0.883
9-4-70	0.000	0.190	0.183	1.483	8.97	17.41	11.97	0.048	0.020	0.916
9-2-48	0.000	0.196	0.184	1.510	7.70	23.09	15.38	0.050	0.004	0.891
9-15-1	0.094	0.201	0.178	1.446	4.73	207.77	125.40	0.055	0.023	0.886
9-12-46	0.000	0.202	0.202	1.444	7.36	19.66	12.15	0.039	0.005	0.936

Table 4.2: Various structural and dynamical properties of each halo in our sample at the most recent relaxed redshift, z_{rel}.

Chapter 5 | *Conclusions*

In this thesis we examine several aspects of the structure and substructure of cold dark matter halos using fully cosmological simulations of their formation. In doing so, we have neglected the effects of baryons, and assumed that the initial conditions are provided by the CDM cosmological model and that the equations of motion are Newtonian. Such an approach captures the non-linear evolution of primordial overdensities and allows one to extract the essential information required in order to develop an understanding of the structure of CDM halos in the universe, and the processes by which their structures are attained.

The main results of this thesis were presented in three separate chapters. Here we provide a summarizing account of the main new results, discuss the implications for our understanding of the structure and substructure of ΛCDM halos, and comment on the prospects of future work that may be motivated by our results.

5.1 The Structure and Substructure of Cold Dark Matter Halos

We present our main results pertaining to the structure of dark matter halos in chapters 3 and 4. The most important result of this study is the discovery that the only "universal" feature of dark matter halo structure in the ΛCDM cosmology is the radial stratification of phase-space density, ρ/σ^3. Although this quantity (and its universality) has been focus of much attention in the literature already (e.g. Dehnen & McLaughlin 2005; Stadel et al 2008; Knollmann et al 2008; Ascasibar &

Gottleober 2008; Ziat et al 2008; Van Hese et al 2008; Navarro et al 2008; Lapi & Cavaleir 2008) we here show that it is more fundamental than several other "universal" structural and dynamical features of virialized halos. In particular, by focusing our attention on the structure of *dynamically relaxed* dark matter halos we show explicitly that the global shape of the spherically averaged density profile (quantified by the rate of change of its logarithm) of a sample of halos depend strongly on their concentrations. The systematic dependence of the shape of the spherically averaged $\rho(r)$ profile on the halo formation history of a given halo indicates that this quantity is *not* a universal feature of CDM halos, as is often claimed (and assumed) in the literature. Furthermore, we go on to show that there exists a simple scaling between the densities and velocity dispersions across a halo such that their ratio, ρ/σ^3, remains independent of whatever physics governs the minute differences in the $\rho(r)$ (and $\sigma(r)$) profiles.

Interestingly, we find that the phase-space density profile follows very closely a single power-law for all halos in our sample, consistent with $\rho/\sigma^3_{\rm tot} \propto r^{-1.875}$. Perhaps more intriguing is the fact that this is the same form for the phase-space density profile derived from spherical collapse models by Bertschinger (1985). In the latter, spherical shells of dark matter turn around and collapse smoothly onto spherical overdensities, relaxing into structures with power-law density, velocity dispersion, and phase-space density profiles. To contrast the simplicity of this model with the fully cosmological one, we note that in the real universe primordial overdensities span many overlapping scales, are non-spherical, and that the collapse of matter first initiates along large-scale sheets and filaments. This results in a highly asymmetric accretion process in which clumps of dark matter and gas accrete along filaments and merge together forming progressively larger structures. The complexity of this process generates episodes of *violent* halo relaxation (Lynden-Bell 2005) and the possibility of instabilities that can drive the system further still from spherical symmetry (Bellovary et al, 2008). The resulting systems have density and

velocity dispersion profiles with a complex radial behavior, with densities steepening outwards from the halo center. It is thus surprising that the phase-space density profiles are so remarkably similar. Why the phase-space density profiles should follow this power-law to begin with is still a mystery.

To add to this, it has been recently shown that, outside a certain "core" radius, the entropy profile of gas in galaxy clusters follows the same radial power-law as is predicted for the dark matter (Faltenbacher et al 2007). The adiabatic accretion of collisional gas onto the potential wells of galaxy clusters is again a very different process than the violent hierarchical growth of the *collisionless* dark matter halos themselves. Understanding the origin and ubiquity of the $\sim r^{-1.875}$ power-law is thus a very interesting theoretical problem, which may have strong implications for our understanding of structure formation in the universe.

We examine the robustness of the power-law phase-space density profile to numerical resolution using the simulations of the *Aquarius project*. In the highest resolution run of the sample we robustly probe the structure of dark matter halos to scales approaching ~ 100 pc (less than 0.1% of r_{200}). We confirm that the spherically averaged phase-space density profile follows Bertschinger's law over the entire resolved radial range, with no systematic deviations down to the innermost point.

In § 4.3.3 of chapter 4 we follow the mass accretion histories of a sample of halos and show explicitly the connection between halo growth and the logarithmic slope of the density profile. We find that systems collapsing early on have *systematically steeper* density profiles than their later-forming counterparts. This manifests as a rather strong correlation between the the Einasto index α and the concentration parameter $c = r_{200}/r_{-2}$ describing a given halo (see Fig. 4.6).

Our results indicate that the Einasto parameter, α, appears to modulate the radial dependence of the quantity $\kappa = V_c^2/\sigma^2$. This suggests that α reflects how the level of kinetic support varies as a function of enclosed mass *across the system*. We find similar differences in the energy content of linear overdensities whose collapse

lead to the formation of these systems: linear overdensities which exhibit less kinetic support for a given enclosed mass collapse early, forming virialized halos which, at $z = 0$, also have less kinetic support for a given enclosed mass. Thus, subtle differences in the structure of CDM halos at $z = 0$ appear to reflect processes occurring in the very early universe, and so should not depend on the specific details of the mass accretion histories, such as the time since the most recent major merger.

In chapter 2 we use a suite of 11 N-body simulations to study the detailed orbital trajectories and accretion histories of substructure halos in and around galaxy sized dark matter halos in the ΛCDM cosmogony. In doing so we are able to show that the number of subhalos *physically associated* with a given dark matter halo (defined as the set of all subhalos that have at least once crossed within the virial radius of the systems main progenitor) outnumber by roughly a factor of two the total number of subhalos within the virial radius at $z = 0$. This is reflected by the fact that only $\sim 20\%$ of all associated subhalos have $r_{\rm apo} < r_{200}$. We go on to show that a significant fraction ($\sim 39\%$) of the associated subhalo population follow *unorthodox* orbits that carry them beyond their turnaround radius, $r_{\rm ta}$. We trace the gain in orbital energy to multiple-body interactions acting during the tidal dissociation of bound groups as they are accreted by the host halo.

One implication of this result is that seemingly isolated galaxies near more massive structures may show tell-tale signs of tidal effects normally attributed to passage through a more massive potential. Some possibilities include the appearance of ram pressure stripping, truncated surface brightness profiles, or the existence of dwarf spheroidal galaxies at distances as large as (or larger than) 3 r_{200}.

We have found that there exists a clear and robust mass dependence to the above effect, in which lower mass subhalos more readily gain energy than their high mass counterparts. This mass dependence is a natural consequence of the multiple-body interactions acting during the accretion and subsequent disruption of bound groups

as they are accreted by the host galaxy.

The preferential ejection of low-mass subhalos can be understood by considering the case of a bound pair of subhalos of widely different mass. In this case, the trajectory of the more massive subhalo follows closely the trajectory of the systems center of mass, and its motion relative to it is minimal. The low mass subhalo, on the other hand, will exhibit large excursions about the systems center of mass and is capable of capturing orbital energy when its orbit within the pair happens to to be in phase with the orbit of the pair within the body of the main halo.

This effect, combined with the enhanced survival likelihood for subhalos on large-apocenter orbits, results in a clear segregation in the spatial and dynamical distribution of associated subhalos when split in terms of their mass at *accretion time*; the lower the subhalo mass at accretion time the less concentrated and kinematically hotter their descendant population. The more pronounced effects of dynamical friction and tidal stripping on more massive subhalos eliminates this bias when quantified in terms of the *present day* subhalo mass. This indicates that efficient mixing of the subhalo population within the potential of the host is *not* responsible for the uniform distribution of subhalos with respect to mass in the body of the main halo, but rather that this is a fortuitous result caused by the mass dependence of processes like dynamical friction and tidal stripping.

The supposition of Klypin et al, that the luminous satellites of the Milky Way Galaxy are hosted by the most massive substructure halos at accretion time then suggests that the visible satellites may be significantly more concentrated and kinematically biased relative to the dark matter halo of the Galaxy, and the subhalo population as a whole. This result could have implications for studies attempting to deduce the mass of the Milky Way from the dynamics and spatial distribution of its nearby satellites.

In chapter 3 we corroborated several of our findings from chapter 2 by using the unprecedented statistics and dynamic range of subhalos found in the *Aquarius*

simulations. In particular, we show that the spatial distribution and dynamics of the subhalo population at $z = 0$ is strongly biased with respect to the dark matter distribution and largely independent of subhalos mass. Substructure halos show a strong preference to be found in the outer regions of the halo, with less that about 0.1% of the mass within the solar circle being bound into small clumps. A full treatment of the orbital properties, accretion histories, and dynamical evolution of subhalos in these simulations is still pending but is likely to provide valuable insights into the process responsible for "lighting-up" substructure halos in systems such as the Milky Way Galaxy.

In our analysis of the subhalo population of the Aquarius simulations, we pay great attention to the validating numerical convergence and explore the uncertainties associated with halo-to-halo expected for Milky Way-like halos. This is achieved by simulating a sample of six halos at varying resolution, including one which we simulate five times, with mass resolution increasing by a factor of about 2000. We have focused our analysis on the $z = 0$ properties of the subhalo population, but plan to address questions related to their *evolution* in future work.

Our analysis indicates that the abundance of dark matter subhalos as a function of their mass is remarkably similar across our halo sample when normalized to the parent halo mass. This is particularly evident when considering subhalos of sufficiently low mass, so that counting statistics contribute negligible errors. The substructure mass function of each of the six Aquarius halos is described very accurately by a single power-law: $dN/dM \propto M^{-1.9}$. This indicates that the total mass fraction in subhalos is bounded to a small fraction of the total parent mass, indicating that a *smooth* halo component dominates the halo mass distribution. We find that less than $\sim 20\%$ of the total mass found within r_{50} at $z = 0$ should be bound into small clumps, an estimate which includes the contribution of "unresolved" subhhalos.

5.2 Consistency with Other Work

The results presented in this thesis agree with those of a number of studies by other groups, but important discrepancies are also evident. Most importantly, we find that our results related to the cusp structure, and substructure abundance disagree both qualitatively and quantitatively with those of the *Via Lactea* simulations (Diemand et al 2007, 2008; Kuhlen et al 2008, Madau et al 2008). Regarding the substructure content, we find *substantially more* substructure than reported for the Via Lactea simulations independently of subhalo mass, and numerical resolution. We find that the discrepancy between subhalo abundances in the Aquarius and Via Lactea simulations is much larger than the halo-to-halo scatter observed in our six runs, suggesting that cosmic scatter is unlikely to be the origin of the discrepancy. Furthermore, since the Via Lactea group adopted a lower normalization of the matter power spectrum ($\sigma_8 = 0.72$ for Via Lactea, whereas $\sigma_8 = 0.9$ for Aquarius) we expect differences in the background cosmology to have an opposite effect: lowering σ_8 delays structure formation slightly leading to an *increase* in the abundance of substructure halos surviving at $z = 0$.

In § 3.4 of chapter 3 we investigated the internal structure of Milky Way-like dark matter halos using the Aquarius simulations. Here, we confirmed the results of many previous studies regarding the *shape* of the spherically averaged density profile (e.g. Power et al 2003; Navarro et al 2004; Gao et al 2007): dark matter halos exhibit power-law logarithmic density slopes that shallow progressively from the outermost to the innermost regions of the halo, with no sign on converging to an asymptotic power-law. This interpretation differs from that of Diemand et al (2004, 2005, 2007) who use simulations of comparable resolution and conclude that the spherically averaged density profile converges to a well defined power-law: $\rho \propto r^{-1.2}$. We do note, however, that more recently members of the same group have completed an even higher resolution simulation of a Milky Way-like dark matter halo (which they dubbed "G-Halo") than the preceding Via Lactea simulations

(Stadel et al 2008). Here, these authors argue that the density profile shallows systematically down to the inner-most resolved point, in agreement with the results presented in this thesis.

Although the Via Lactea simulation is of exceptionally high resolution, these authors fail to associate a detailed numerical convergence study with their results. This makes isolating the origin of the discrepancy between our results and theirs a difficult task. The results presented in chapter 3 demonstrate the exceptional numerical convergence achieved in the Aquarius simulation suite. Combining a detailed numerical convergence study with simulations of a number of different halos gives us confidence that our results provide an accurate representation of the structure and substructure populations of ΛCDM halos. Since the Via Lactea and Aquarius simulation programmes are the highest resolution simulations of their kind, resolving the discrepancies between them is a very important task and should be the focus of future work.

5.3 Future Prospects

In this thesis we have presented several interesting results related to the structure of dark matter halos forming through hierarchical merging. Neither the density nor the velocity dispersion profiles exhibit self-similarity yet there exists a coupling between the two that preserves a unique power-law phase-space density profile. In particular, we have shown explicitly that the *only* universal property of relaxed dark matter halos is the radial stratification of phase-space density, $\rho/\sigma^3 \propto r^{-1.875}$. This begs a question of fundamental importance: what is the origin of the $r^{-1.875}$ power-law phase-space density profile?

This question has recently been addressed by a number of authors (e.g. Austin et al 2005; Barnes et al 2005, 2006, 2007; Bellovary et al 2008) using semi-analytic models of halo formation and idealized collapse simulations. The purpose of these

studies is to compliment the fully cosmological treatment of halo formation, and to isolate common physical processes (such as violent relaxation, or the radial orbit instability) that may be responsible for similarities in the resulting structures.

For example, Austin et al (2005) use semi-analytic Extended Secondary Infall Models to show that the nearly scale-free distribution of ρ/σ^3 is a robust feature of halos in equilibrium. Since these models do not include substructure explicitly, these authors argue (as in the original work of Bertschinger) that this must be an outcome of violent relaxation, rather than hierarchical merging. Barnes et al (2006) examine the rich analytic content of the isotropic Jeans equation and show that mechanical equilibrium alone is an insufficient condition for producing power-law phase-space density profiles; systems with, for example, Hernquist or King mass profiles *do not* have power-law profiles in phase-space. The analysis of the Jeans equation was extended in Barnes et al (2007) to include the effects of velocity anisotropy. Here it was shown that reproducing both the density and velocity anisotropy profiles of simulated halos *requires* a roughly linear relationship between the density slope $\gamma(r)$ and the velocity anisotropy $\beta(r)$, as observed by Hansen & Moore (2006), but that such a relation is *not* stipulated by a power-law phase-space density profile. In other words, the roughly linear β-γ and power-law ρ/σ^3 relations appear to have a distinct physical origin.

More recently, works published by Knollmann et al (2008) and Schmidt et al (2008) have cast doubt on the validity of the universal power-law description of the pseudo-phase-space density profile. In the first of these, it was shown, using a statistically significant sample of halos simulated in scale-free cosmologies, that the best-fit power-law slope of the phase-space density profile depends systematically on halo concentration; more concentrated systems appear to prefer systematically steeper phase-space density slopes. These authors claim that this result is robust, in the sense that it applies to dynamically relaxed systems and appears independent of the radial range over which the power-law is fit.

Schmidt et al (2008) argue that the strongest power-law correlation describing the phase-space density profile of dark matter halos is not, in fact, that given by ρ/σ^3, as in the original work of Taylor & Navarro (2001). These authors instead argue that a generalized phase-space density profile of the form ρ/σ_d^ϵ always provides a better power-law than T&N's special case. Here, $\sigma_d^\epsilon = \sigma_r^\epsilon(1 + D\beta)^{\epsilon/2}$, is the "general" velocity dispersion profile, with D and ϵ left as free parameters. It is perhaps not surprising that such a description of the phase-space density profile, which includes two additional free parameters, can always always be forced to fit a power-law more accurately.

However, a key point that these (and esssentially all other) authors have failed to realize is that Bertschinger's solution *is not* a pure power-law, rather it exhibits a systematic positive curvature near the so-called "shock radius". The numerical solution asymptotically approaches $\rho/\sigma^3 \propto r^{-1.875}$, but recently accreted material in the outer regions of a halo remains unrelaxed for several orbits before gradually settling into the asymptotic form. This introduces a second parameter, r_{shock}, which must be considered in any future discussions of either the universality or the global shape of the pseudo-phase-space density profile.

If one assumes, for simplicity, that the shock radius of Bertschinger's secondary infall solution occurs roughly at the halo virial radius, r_{200}, then one expects to see a correlation between the slope of the phase-space density profile and the concentration of the halo, as noted already by Knollmann et al. The reason is for this is that systems with lower concentrations will exhibit a stronger curvature near the halo scale radius, r_{-2}. This effect is subtle, but was already apparent in Fig. 4.2, where a systematic positive curvature away from a pure $r^{-1.875}$ power-law can be seen at large radii.

The work presented in Chapters 3 and 4 clearly show that the pseudo-phase-space density profile exhibits a self-similarity that is not evident in either the spherically averaged density or velocity dispersion profiles alone. However, as mentioned

above, we are still far from understanding the origin and robustness of this apparent universality and this should be the focus of future work on the subject. In particular, we plan to investigate the the universality of the phase-space density profiles of our simulated halos by comparing them directly with the solutions of Bertschinger's Spherical Secondary Infall Models. We plan to investigate the *origin* of the pseudo-phase-space density profile by following the details of the accretion and subsequent relaxation of material composing each virialized halo. This work will be augmented by controlled simulations of spherical collapse in idealized situations, with the hope of coaxing out the physics responsible for creating the nearly scale-free ρ/σ^3 distributions. This work will provide valuable new insights into the structure of dark matter halos and the processes responsible for molding them.

Bibliography

Afshordi N., Tolley A. J., 2008, arxiv:08061046

Amara A., Metcalf R.B., Cox T.J., & Ostriker J.P., 2006, *Mon. Not. R. Astron. Soc.*, **367**, 1367

Ascasibar Y. & Gottloeber S., 2008, *Mon. Not. R. Astron. Soc.*, **386**, 2022

Austin, C.G., Williams, L.L.R., Barnes, E.L., Babul, A., Dalcanton J.J., 2005, *Astrophys. J.*, **634**, 756A

Babcock H.W., 1939, *Lick Obs. Bull.*, **19**, 41 (No. 498)

Balough M.L., Navarro J.F., Morris S.L., 2000, *Astrophys. J.*, **540**, 113

Bardeen, J.M., Bond, J.R., Kaiser, N. & Szalay, A.S., 1986, *Astrophys. J.*, **304**, 15

Barnes, E.I., Williams, L.L.R., Babul A., Dalconton, J.J., 2005, *Astrophys. J.*, **634**, 775B

Barnes, E.I., Williams, L.L.R., Dalconton, J.J., Babul, A., 2007, *Astrophys. J.*, **665**, 847

Barnes, E.I., Williams, L.L.R., Babul, A., Dalconton, J.J., 2007, *Astrophys. J.*, **643**, 797B

Bartelmann M., Meneghetti M., 2005, *Astron. & Astroph.*, **418**, 413

Bergström L., Ullio P., Buckley J.H., *Astroparticle Phys.*, 1998, **9**, 137

Bekenstein J., 2004, *Phys. Rev. Lett. D*, **71** E

Bellovary J., Dalcanton J.D., Babul A., Quinn T.R., Maas R.W., Austin C.G., Williams L.L.R., Barnes E., 2008, (astro-ph/08063434)

Benson A. J., 2005, *Mon. Not. R. Astron. Soc.*, **358**, 551

Bertschinger E., 1985, *Astrophys. J.*, **58**, 39

Binney J.J, Davies R.L., Illingworth G.D., 1990, *Nature*, **361**, 78

Blumenthal J.R, Faber S.M., Primack J.R., Rees M.J., 1984, *Nature*, **311**, 517

Bullock, J.S., Kolatt, T.S., Sigard, Y., Sommerville, R.S., Kravstov, A.V., Klypin, A.A. Primack, J.R., Dekel, A., 2001, *Mon. Not. R. Astron. Soc.*, **321**, 559

Bullock, J.S., Dekel, A., Kolaltt, T.S., Kravstov, A.V., Klypin, A.A., Porciani, C., Promack, J.R. **2001**, *Astrophys. J.*, 555, 240B

Burkert, A., 1995, *AstroPhys J.*, **447**, L25+

Byram E.T, Chubb T.A., & Friedman H, 1966, *Science*, **152**, 66

Calcáneo-Roldán C., Moore B., 2000, *Astrophys. J. L.*, **62**, 12, 123005

Carbone C., Verde L., Mataresse S., 2008, arxiv:08061950

Clowe D., Gonzales A., & Markevitch M., 2004, *Astrophys. J.*, **604**, 596

Colless M., et al. 2001, *Mon. Not. R. Astron. Soc.*, **328**, 1039C

Colombi S., Dodelson S., & Widrow L.M., 1996, *Astrophys. J.*, **485**, 1C

Crone M.M, Evrard A.E., & Richstone D.O., 1994, *Astrophys. J.*, **434**, 402

Croton D.J., Springel V., White S.D.M., et al, 2006, *Mon. Not. R. Astron. Soc.*, **365**, 11

Dalal N., Kockanek C.S., 2002, *Astrophys. J.*, **572**, 25

Davis M., Efstathiou G., Frenk C.S., White S.D.M., 1985, *Astrophys. J.*, **292**, 371

de Blok W.J.D., McGaugh S.S, Bosma A., Rubin V.C., 2001a, *Astrophys. J.*, **552**, L23

de Blok W.J.D., McGaugh S.S, Rubin V.C., 2001b, *Astrophys. J.*, **122**, 2396

Dehnen, W. & McLaughlin, D.E. 2005, *Mon. Not. R. Astron. Soc.*, **363**, 1057

Delahaye T., Lineros R., Donato F., Fornengo N., Salati P., 2008, *Phys. Rev. D*, **77**, 3527

De Lucia G., Kauffmann G., Springel V., White S.D.M., Lanzoni B., Stoehr F., Tormen G., Yoshida N., 2004, *Mon. Not. R. Astron. Soc.*, **348**, 333D

Diemand J., Moore B., Stadel J., 2004, *Mon. Not. R. Astron. Soc.*, **352**, 535D

Diemand, J., Zemp, M., Moore, B., Stadel, J., Carollo, C.M. 2005, *Mon. Not. R. Astron. Soc.*, **364**, 665D

Diemand J., Kuhlen M. Madau P., 2007, *Astrophys. J.*, **657**, 262D

Diemand J., Kuhlen M. Madau P., 2007, *Astrophys. J.*, **667**, 859D

Dubinsky J., Carlberg R.G., 1991, *Astrophys. J.*, **378**, 496

Dunkley J, et al, 2008, Submitted to *Astrophys. J. Supp.*, (astro-ph/08030586)

Eke V.R., Cole S., Frenk C.S., 1996, *Mon. Not. R. Astron. Soc.*, **282**, 263

Einasto J., *Trudy Inst. Astrofiz. Alma-Ata*, 1965, **51**, 87

FaltenBacher A. & Diemand J., 2006, *Mon. Not. R. Astron. Soc.*, **367**, 1781

FaltenBacher A., Hoffmann Y., Gottlöber S., Gustavo Y., 2007, *Mon. Not. R. Astron. Soc.*, **376**, 1327F

Fillmore J.A., & Goldreich P., 1984, *Astrophys. J.*, **281**, 1

FLores R.A., & Primack J.R., 1994, *Astrophys. J.*, **427**, L1

Frenk C.S., White S.D.M., Efstathiou G., Davis M., 1985, *Nature*, **317**, 595

Fritz G., Davidsen A., Meekings J.F., & Friedman H., 1971, *Astrophys. J.*, **161**, L81

Fukushige T., Makino K., 1997, *Astrophys. J.*, **477**, L9

Fukushige, T. & Makino, J. 2001, *Astrophys. J.*, **557**, 533

Gao L., White S.D.M., Jenkins A., Stoehr F., Springel S., 2004, *Mon. Not. R. Astron. Soc.*, **355**, 819G

Gao L., Springel S., White S.D.M., 2005, *Mon. Not. R. Astron. Soc.*, **363L**, 66G

Gao L., Navarro J.F., Cole S., Frenk C.S., White S.D.M., Springel V., Jenkins A., Neto A., 2007, arXiv:07110746

Ghigna S., Moore B., Governato F., Lake G. Quinn T., Stadel J., 1998, *Mon. Not. R. Astron. Soc.* **300**, 146

Ghigna S., Moore B., Governato F., Lake G. Quinn T., Stadel J., 1999, aspc, **176**, 140G

Ghigna S., Moore B., Governato F., Lake G., Quinn T., Stadel J., 2000, *Astrophys. J.*, **544**, 616

Gill S.P.D., Knebe A., Gibson B.K., 2005, *Mon. Not. R. Astron. Soc.*, **356**, 1327

Green A.M., Hofmann S., Schwarz D.J., 2004, *Mon. Not. R. Astron. Soc.*, **353**, L23

Gunn J.E., & Gott J.R.I., 1972, *Astrophys. J.*, **176**, 1

Guth A.H., 1981, *Phys. Rev. Lett. D*, **23**, 347

Hagan B., Ma C.P., & Kravstov A.V., 2005, *Astrophys. J.*, **633**, 537

Hahn O., Porciani C., Dekel A., Corollo C.M., 2008, (astro-ph:08034211)

Hansen, H.S. & Stadel, J. 2006, *Journal of Cosmology and Astro-Particle Physics*, **5**, 14

Hansen, S.H. & Moore, B. 2006, *New Astronomy*, **11**, 333

Hayashi E., Navarro J.F., Power C, Jenkins A., Frenk C.S., Power C., White S.D.M., Springel V., Stadel J., Quinn T., Wadsley J., 2004, arxiv:0408132

Hayashi E., & Navarro J.F., 2006, *Mon. Not. R. Astron. Soc.*, **373**, 1117H

Hayashi E., & White S.D.M., 2008, (astro-ph:07093933)

Helmi A., White S.D.M., Springel V., 2002, *Phys. Rev. Lett. D*, **66f**, 3502H

Helmi A., White S.D.M., Springel V., 2003, *Mon. Not. R. Astron. Soc.*, **339**, 834

Hennawi J.F., Dalal N., Bode P., & Ostriker J.P., 2007, *Astrophys. J.*, **654**, 714

Hoffman Y., & Shaham J., 1985, *Astrophys. J.*, **297**, 16

Hoffman, Y., Romano-Diaz, E., Shlosman, I. & Heller, C. 2007, (astro-ph/07060006)

Hofmann S., Schwarz D.J., Stö H., 2001, *Phys. Rev. Lett. D*, **64**, 8, 083507

Ishyama T., Fukushige T., Makino J., 2007, (astro-ph/07081987)

Jing, Y.P. & Suto, Y. 2000, *Astrophys. J.*, **529L**, 69J

Jing Y.P., Suto Y., Mo H.J., 2007, *Astrophys. J.*, **657**, 664J

Kallivayalil N, van der Marel R.P., Alcock C., *Astrophys. J.*, 2006, **652**, 1213K

Klypin A., Kravstov A.V., Valenzuela O., Prada F., 1999, *Astrophys. J.*, **522**, 82

Klypin, A., Kravstov, A.V., Bullock, J.S. & Primack, J.R. 2001, *Astrophys. J.*, **554**, 903

Knollmann S., Knebe A., Hoffmann Y., 2008, (astro-ph/08091439)

Komatsu E., Dnukley J., Nolta M.R., et al, 2008, (astro-ph/08030547)

Kravtsov A.V., Klypin A.A., Bullock J.S., Primack J.R., 1998, *Astrophys. J.*, **502**, 48

Kravtsov A.V., 2001, *AIPC*, **586**, 130K

Kravtsov A.V., Gnedin O.Y., Klypin A.A., 2004, *Astrophys. J.*, **609**, 482K

Kroupa P., Thies C., Boily C.M., 2005, *Astron. & Astroph.*, **431**, 517

Kuhlen M., Diemand J., & Madau P., 2007, *Astron. & Astroph.*, **671**, 1135

Kuhlen M., Diemand J., & Madau P., 2008, (astro-ph/08054416)

Kunkel W.E., Demers S., 1976, *R. Greenwhich Obser. Bull.*, **182**, 241

Lapi A. & Cavaliere A., 2008, (astro-ph/08101245)

Libeskind N.I., Cole S., Frenk C.S., Okamoto T., Jenkins A., 2007, *Mon. Not. R. Astron. Soc.*, **374**, 16

Li & Helmi, 2007, on the arXiv, accepted to *Mon. Not. R. Astron. Soc.*

Lokas, E.L., Wojtak, R., Gottlöber, S., Mamon, G.A. & Prada, F. 2006, *Mon. Not. R. Astron. Soc.*, **367**, 1463

LoVerde M., Miller A., Shandera S., Verde L., 2007, *J. Cosmo. & Part. Phys.*, **4**, 14

Ludlow, A.D., Navarro, J.F., Springel V., Jenkins, A.R., Frenk, C.S. & Helmi, A. 2008, (astro-ph/08011127)

Lynden-Bell D., 1976, *Mon. Not. R. Astron. Soc.*, **174**, 695

Lynden-Bell D., 1982, *Obs*, **102**, 202

Lynden-Bell D., 1967, *Mon. Not. R. Astron. Soc.*, **136**, 101

Madau P, Diemand J., Kuhlen M., 2008, *Astrophys. J.*, **679**, 1260

Mamon G.A., Sanchis T., Salvador-Solé E., Solanes, J.M., 2004, AA, **414**, 445

Mao S., Jing Y.P., Ostriker J.P., & Weller J., 2004, *Astrophys. J.*, **604**, L5

Markevitch M., Gonzales A.H., Clowe D., Vikhlinin A., Forman W., Jones C., Murray S., Tucker W., 2002, *Astrophys. J.*, **606**, 219

Meekins J.F., Gilbert F., Chubb T.A., Friedman H., & Henry R.C., 1971, *Nature*, **231**, 107

Merritt D., Navarro J.F., Ludlow A., Jenkins A., 2005, *Astrophys. J.*, **624**, 85

Merritt D., Graham A.W., Moore B., Diemand J., Terzić B., 2006, *Astrophys. J.*, **132**, 2685

Milgrom M., 1983, *Astrophys. J.*, **270**, 365

Milgrom M., 1983, *Astrophys. J.*, **270**, 371

Milgrom M., 1983, *Astrophys. J.*, **270**, 384

Moore B., 1994, *Nature*, **370**, 629

Moore, B., Governato, F., Quinn, T., Stadel, J., Lake, G. 1998, *Astrophys. J.*, **499**, L5

Moore, B. et al 1999, *Astrophys. J.*L, **524**, L19

Moore B., Ghigna S., Governato F., Lake G., Quinn T., Stadel J., Tozzi P., 1999, *Astrophys. J.*, **524**, L19

Nagai D., & Kravstov A.V., 2005, *Astrophys. J.*, **618**, 557

Natarajan P. & Springel V., 2004, *Astrophys. J.*, **617**, 13

Navarro J.F., White S.D.M., 1993, *Mon. Not. R. Astron. Soc.*, **265**, 271

Navarro, J.F., Frenk, C.S., & White, S.D.M. 1996, *Astrophys. J.*, **462**, 563

Navarro, J.F., Frenk, C.S., & White, S.D.M. 1997, *Astrophys. J.*, **490**, 493

Navarro J., Hayashi E., Power C., Jenkins A.R., Frenk C.S., White S.D.M., Springel V., Stadel J., Quinn T.R., 2004, *Mon. Not. R. Astron. Soc.*, **349**, 1039N

Neto A.F., et al, 2007, *Mon. Not. R. Astron. Soc.*, **381**, 1450

Ostriker J.P & Peebles P.J.E, 1973, *Astrophys. J.*, **186**, 467

Ostriker J.P, Peebles P.J.E, & Yahil A., 1974, *Astrophys. J.*, **193**, L1

Peebles P.J.E, 1982, *Astrophys. J.*, **263**, L1

Perlmutter S. et al, 1999, *Astrophys. J.*, **517**, 565

Piatek S., Pryor C., Olszewski E. W., 2007, arXiv:07121764

Porter D.H., Ph.D. Thesis California Univ., Berkeley

Power C., Navarro J.F., Jenkins A.R., Frenk C.S., White S.D.M., Springel V., Stadel J., Quinn T., 2003, *Mon. Not. R. Astron. Soc.*, **338**, 14P

Prada, F., Klypin, A.A., Simonneau, E., Betancort-Rijo, J., Patiri, S., Gottlöber, S. & Sanchez-Conde, M.A. 2006, *Astrophys. J.*, **645L**, 5G

Quinn P.J., Salmon J.K., & Zurek W.H., 1986, *Nature*, **322**, 329

Ricotti, M. 2003, *Mon. Not. R. Astron. Soc.*, **364**, 1105

Ricotti, M., Pontzen, A. & Viel, M. 2007, *Astrophys. J.*, **663L**, 53R

Riess A.G et al, 1998, *Astrophys. J.*, **116**, 38

Roberts M.S. & Whitehurst M.N., 1975, *Astrophys. J.*, **201**, 327

Rubin V. & Ford W.K., 1970, *Astrophys. J.*, **159**, 379

Rubin V., Burstein D., Ford W.K. Jr., Thonnard N., 1985, *Astrophys. J.*, **289**, 81

Sales L.V., Navarro J.F., Abadi M.G., Stienmetz M., 2007, *Mon. Not. R. Astron. Soc.*, **379**, 1464

Sales L.V., Navarro J.F., Abadi M.G., Stienmetz M., 2007, *Mon. Not. R. Astron. Soc.*, **379**, 1475S

Sand D.J., Treu T., Smith G.P., Ellis R.S., 2004, *Astrophys. J.*, **604**, 88

Schmidt K.B., Hansen S.H., Maccio, A.V., 2008, *Astrophys. J.*, **689**, 33

Seljak U., Zaldarriaga M., 1996, *Astrophys. J.*, **469**, 437

Silk J., 1968, *Astrophys. J.*, **151**, 459

Smith, S., 1936, *Astrophys. J.*, **83**, 23

Spergel D.N., et al. 2003, *Astrophys. J.*, **148**, 175S

Spergel, D.N., et al. 2007, *Astrophys. J.*s, **170**, 377S

Springel V., White S.D.M., Tormen G., Kauffmann G., 2001, *Mon. Not. R. Astron. Soc.*, **328**, 726S

Springel V. 2005, *Mon. Not. R. Astron. Soc.*, **364**, 1105S

Springel V., White S.D.M, Frenk C.S., Navarro J.F., Jenkins A., Vogelsberger M., Wang J., Ludlow A., Helmi A., 2008, (astro-ph/08090894)

Springel V., Wang J., Vogelsberger M., Ludlow A., Jenkins A., Helmi A., Navarro J.F., Frenk C.S., White S.D.M., 2008, (astro-ph/08090898)

Stadel J, Potter D., Moore B., Diemand J., Madau P., Zemp M., Kuhlen M., Quilis V., 2008, (astro-ph/08082981)

Stoehr F., White S.D.M., Springel V., Tormen G., Yoshida N., 2003, *Mon. Not. R. Astron. Soc.*, **345**, 1313

Taylor, J.E. & Navarro, J.F. 2001, *Astrophys. J.*, **563**, 483T

Taylor J. E., Babul A., 2005, *Mon. Not. R. Astron. Soc.*, **364**, 515T

Taylor J. E., Babul A., 2005, *Mon. Not. R. Astron. Soc.*, **464**, 535T

Toomre A., Toomre J., 1972, *Astrophys. J.*, **178**, 623

van Albada T.S., 1982, *Mon. Not. R. Astron. Soc.*, **201**, 939V

van den Bergh S., 1999, *PASP*, **111**, 657

van den Bergh S., 1962, *Zs. f. Astrophys.*, **55**, 21

van der Marel R.P., Binney J.J., Davies R.L., 1990, *Mon. Not. R. Astron. Soc.*, **245**, 582

Van Hese E., Baes M., Dejonghe H., 2008, (astro-ph/08090901)

Vogelsberger M., White S.D.M, Helmi A., Springel V., 2008, *Mon. Not. R. Astron. Soc.*, **385**, 236

Wagoner R.V., Fowler W.A., & Hoyle F., 1967, *Astrophys. J.*, **148**, 3

Wang H.Y., Mo H.J., Jing Y.P., 2007, *Mon. Not. R. Astron. Soc.*, **375**, 633

Wang J., White S.D.M, 2008, astro-ph:0809.1322

White S.D.M., & Reese M.J., 1978, *Mon. Not. R. Astron. Soc.*, **183**, 341

White S.D.M., Frenk C.S., Davis M., 1983, *Astrophys. J.*, **274**, L1

White S.D.M., Davis M., Frenk C.S., 1984, *Mon. Not. R. Astron. Soc.*, **209**, 27P

White S.D.M., Davis M., Frenk C.S., Efstathiou G., 1987, *Astrophys. J.*, **313**, 505

White S.D.M, & Zaritsky D., 1992, *Astrophys. J.*, **394**, 1

White S.D.M., Navarro J.F., Evrard A.E., Frenk C.S., 1993, *Nature*, **366**, 429

White S.D.M., 1996, in COsmology and Large Scale Structure, edited by R. Schaefer, J. Silk, M. Spiro, J. Zinn-Justin, Dordrecht: Elseiver, (astro-ph/9410043)

Williams, L.L.R., Austin, C.G., Barnes, E., Babul, A. & Dalcanton, J.J. 2004, in Baryons in Dark Matter Halos, ed. R. Dettmar, U. Klein, & P. Salucci (Trieste: SISSA), http://pos.sissa.it

Willman B., Governato F., Dalcanton J.J., Reed D., Quinn T., 2004, *Mon. Not. R. Astron. Soc.*, **353**, 639

Wojtak, R. & Lokas, E.L. 2007, *Mon. Not. R. Astron. Soc.*, **377**, 834

Yoshida N., Sokasian A., Hernquist L., Springel V., 2003, *Astrophys. J.*, **591**, L1

Zait A., Hoffman Y., & Shlosman I., 2007, astro-ph:0711.3791

Zel'Dovich Y.B., 1970, *Astron. & Astroph.*, **5**, 84Z

Zhu G., Zheng Z., Lin W.P., Jing Y.P., Kang X., Gao L., 2006, *Astrophys. J.*, **639L**, 5Z

Zhao, H. 1996 *Mon. Not. R. Astron. Soc.* **278**, 488

Zwicky F. 1933, *Helvetica Phys.*, **86**, 217

Zwicky F. 1937, *Astrophys. J.*, **86**, 217